Multiphysics Modelling on the Effects of Composition and Microstructure during Tribocorrosion of Aluminum-based Metals and Structures

Kaiwen Wang

Dissertation submitted to the faculty of the Virginia Polytechnic Institute and State University in partial fulfillment of the requirements for the degree of

Doctor of Philosophy
in
Materials Science and Engineering

Wenjun Cai, Chair

Xianming Bai

William T. Reynolds

Hongliang Xin

July 7, 2022

Blacksburg, VA

Keywords: Tribocorrosion, Finite element analysis, Multiphysics modelling, Aluminum, Crystallography

Multiphysics Modelling on the Effects of Composition and Microstructure during Tribocorrosion of Aluminum-based Metals and Structures

Kaiwen Wang

Abstract

Wear and corrosion are two major threats to material integrity in multiple real-life circumstances, including oil and gas pipelines, marine and offshore infrastructures and transportations and biomedical implants. Furthermore, the synergistic effects between the two, named tribocorrosion, could cause, most of the time, severer material degradation to jeopardize materials' long-term sustainability and structural integrity. A representative case is aluminum (Al) and its alloys, which exhibit good corrosion resistance in aqueous solution due to the protection provided by the passive layer. However, these naturally formed layers are thin and delicate, leaving the materials vulnerable to simultaneous mechanical and corrosion damage, which in turn, compromise their resistance to tribocorrosion.

Past research in tribocorrosion mainly relies on costly and trial-and-error experimental methods to study the materials' deformation and degradation under simultaneous wear and corrosion. In an attempt to predict tribocorrosion behavior using numerical analysis, this work developed a set of finite-element-based multiphysics models, in combination with experimental methods for parameter input and validation, focusing on different factors influencing the tribocorrosion behavior of materials.

The first study developed a model with the coupling between strain and corrosion potential and investigated the effect of bulk material properties on tribocorrosion. This model was validated by existing tribocorrosion experiments of two Al-Mn alloys, to analyze the synergistic effects of mechanical and corrosion properties on the material degradation mechanisms of tribocorrosion. During consecutive passes of the counter body, significant residual stress was found to develop near the edge of the wear track, leading to highly concentrated corrosion current than elsewhere.

Such non-uniform surface corrosion and stress-corrosion coupling led to variations of tribocorrosion rate over time, even though testing conditions were kept constant. Tribocorrosion rate maps were generated to predict material loss as a function of different mechanical and electrochemical properties, indicating a hard, complaint metal with high anodic Tafel slope and low exchange current density is most resistant to tribocorrosion.

Secondly, the influence of microstructural design on the tribocorrosion behavior of Al-based nanostructured metallic multilayers (NMMs) was investigated computationally. Specifically, this model accounts for elastic-plastic mechanical deformation during wear and galvanic corrosion between exposed inner layers after wear. The effects of individual layer thickness (from 10 to 100 nm) and layer orientation (horizontally and vertically aligned) on the tribocorrosion behavior of Al/Cu NMMs was studied. Both factors were found to affect the subsurface stress and plastic strain distribution and localized surface corrosion kinetics, hence affecting the overall tribocorrosion rate. This model and the obtained understanding could shed light on future design and optimization strategies of NMMs against tribocorrosion.

Finally, a combined experimental and computational investigation of the crystallographic effect using Al (100), (110), and (111) single crystals as model systems, to understand the effects of crystallographic orientation on the tribocorrosion kinetics by combining tribocorrosion experiments, materials characterization, and multiphysics modeling. EBSD was exploited to characterize the crystal orientation and dislocation density of the worn samples. The tribocorrosion model was built based on the results of EBSD characterization with the coupling effect of crystal orientation and corrosion. The model successfully predicted the overall tribocorrosion current of single-crystal samples, indicating the important role played by crystal orientation and dislocation density in the acceleration of corrosion.

Multiphysics Modelling on the Effects of Composition and Microstructure during Tribocorrosion of Aluminum-based Metals and Structures

Kaiwen Wang

General Audience Abstract

Multiple applications in batteries, aerospace, marine transportation, offshore infrastructure and biomedical implants request metal materials that are both mechanically reliable and corrosion resistant. In addition to pure mechanical wear and corrosion, the synergy of the two, which is called tribocorrosion, also poses major threat to materials' integrity and longevity.

Aluminum is a widely used passive metal due to its advantage of being cheap, light-weighted and corrosion resistant, but is relatively less resistant to wear comparing to other metals. Mechanical damage could strip Al of the protection from the passive layer and also cause stress corrosion. This makes Al susceptible to tribocorrosion. Despite several previous experimental attempts to understand the mechanism of Al tribocorrosion and improve the tribocorrosion resistance of Al by alloying or structural design, there has been little quantitative model on this topic.

In this dissertation, finite element (FE) multi-physics modeling was exploited to investigate the tribocorrosion phenomenon on Al systems in sea water environment. The first model was developed based on strain-electrochemistry coupling and helped study the effect of alloys' composition on the tribocorrosion resistance of the alloy. The second model studied the tribocorrosion of Al/Cu multilayers with the focus on the micro-galvanic coupling between Al and Cu layers and predicted the influence of layer thickness and orientation. The third model exploited the result of crystallographic information from EBSD characterization to study the mechanism of pure Al tribocorrosion on the crystal level. These models provide quantitative explanation to the accelerated corrosion of Al-based metals and structures, as well as guidance to future design of material with optimum wear, corrosion and tribocorrosion resistance.

Acknowledgement

I would like to thank my research advisor professor Wenjun Cai, who has been patiently guiding and assisting me on my research throughout my PhD years. She led me into the field of tribocorrosion research and has been patiently answering academic questions and offering me hand-on help with experiments. She spent a lot of time assisting me with my writing, including journal publications and this dissertation. She has also been offering me advice for my life and career. She has been the key to my development from a amateur to a grown researcher.

I would also like to thank my committee members, Prof. Xianming (David) Bai, Prof. William Reynolds and Prof. Hongliang Xin, who have been helping me with my research when I encounter problems that are not Prof. Cai's specialization, as well as the editing of the dissertation. The courses I've taken from all committee members are also very beneficial to my PhD research.

Next, I would like to thank my group mates, Jia Chen, Wenbo Wang and Zhengyu Zhang. They also helped me a lot in terms of research and life. We also have several collaborations resulting in significant results.

I am also grateful to other researchers at Virginia Tech who helped me, especially Dr. Ya-peng Yu, who has been training and helping me on the operation of FIB, and Dr. Thomas Staley, who has been training for a lot of equipment in the MSE lab.

During my intern at Jefferson Lab, I also learn a lot from staffs at JLab, especially Dr. Charles E. Reece and Dr. Hui Tian, and also want to express my gratitude to them.

The financial support from the US National Science Foundation (NSF), and Virginia Tech is greatly appreciated.

I would like to thank all my friends, especially those at VTCSC, for the helping and supporting me throughout my PhD years.

Last but not the least, I would like to express my gratitude and love to my family, especially my mom and dad. Has not been their support, I wouldn't be able to go through the dark days, the Covid situation, the days when I make no progress in research and want to give up. Thanks for teaching me to be the person I am now.

Attribution

Throughout my Ph.D. years, some colleagues and staffs assisted me with some parts of my dissertation, including carrying out uncertainty quantification and writing/editing the manuscripts. Their contributions are summarized as follow:

Chapter 2: Yinan Wang performed the uncertainty quantification with surrogate model for the FE simulation. I developed the code for wear evaluation and the FE simulation of tribocorrosion in this manuscript. I wrote the whole manuscript and served as the first author. Prof. Wenjun Cai and Prof. Xiaowei Yue served as the corresponding author and were involved in the editing of the manuscript.

Chapter 3: I built the FE model in this study, wrote the manuscript and served as the first author. Prof. Wenjun Cai served as the corresponding author and was involved in the editing of the manuscript.

Chapter 4: I performed all the experiments, characterization and simulation. I wrote the manuscript and served as the first author. Prof. Wenjun Cai served as the corresponding author and was involved in the editing of the manuscript.

Appendix: Hui Tian performed the electrochemical test of the Nb samples. I built the FE model, wrote the manuscript and served as the first author. Prof. Wenjun Cai, Dr. Hui Tian and Dr. Charles E. Reece served as the corresponding author and were involved in the editing of the manuscript.

Table of Contents

List of Figures

List of Tables

Chapter 1. Background and motivation

1.1 Background of wear and corrosion

1.1.1 Dry abrasive wear

Wear refers to the removal or deformation of solid materials, including those induced by mechanical, chemical and thermal causes [1]. Common types of mechanical wear include abrasive wear, adhesive wear, fretting wear and erosion wear, etc. Abrasive wear is a major and very frequent source of material degradation, estimated to cost 1-4% of the gross national product of industrialized nations [2].

Abrasive wear occurs when a hard rough surface slides across a softer surface. The mechanism of abrasive wear can be mainly categorized into two modes: cutting and ploughing [3]. Cutting refers to the material delamination at the front of and underneath the tip, causing direct material removal, forming chips and debris. This is the dominant mechanism when the attack angel is high and the material has a high hardness value. Ploughing refers to the plastic deformation of the sample caused by the tip pushing the material to the front and side of the groove.

A well-known and widely used law for material wear which accounts for macroscale volume loss is Archard's law [4, 5]:

$$Q = \frac{KWL}{H} \tag{1.1}$$

where Q is the volume of material removal, W is the normal load, L is the sliding distance and H is the hardness of the material experiencing wear. K is a constant depending on several factors, like surface roughness and relative hardness, which could only be obtained from experimental results. Thus, this equation is semi-empirical and requires extensive experiments to establish the validity for the input of parameter K. Hokkirigawa et al. investigated the effect of load, the hardness of the material and the shape of the counter-body on wear modes and degree of penetration using rotation disk scratch test and SEM characterization [6, 7]. Several early theoretical models were proposed based on analytical derivation with plasticity theory to account

for the wear mechanism at microscale level using a simplified geometry of asperity contact [8, 9]. These analytical models are limited by their counter-body shape which needs to be a specific ideal geometry. It also lacks the bridge between the microscale plasticity to macroscale material removal. Despite these limitations, these models pave the way for prediction of material removal caused by wear.

1.1.2 Thermodynamics and kinetics of aqueous corrosion

Corrosion refers to the electrochemical degradation of material. Metals have irreplaceable applications due to their mechanical, electrical and thermal properties. However, they are also the category of the materials that suffers most from corrosion. The electrochemical mechanism of the corrosion process of metals can mostly be summarized by the oxidation of the metal elements as the anodic half reaction:

$$M \rightarrow M^{n+} + ne^- \tag{1.2}$$

and the oxygen reduction

$$O_2 + 2H_2O + 4e^- \rightarrow 4OH^- \text{ (For neutral or alkaline solution)} \tag{1.3}$$

$$O_2 + 4H^+ + 4e^- \rightarrow 2H_2O \text{ (For acidic solution)} \tag{1.4}$$

or hydrogen evolution reaction

$$2H^+ + 2e^- \rightarrow H_2 \tag{1.5}$$

as the cathodic half reaction.

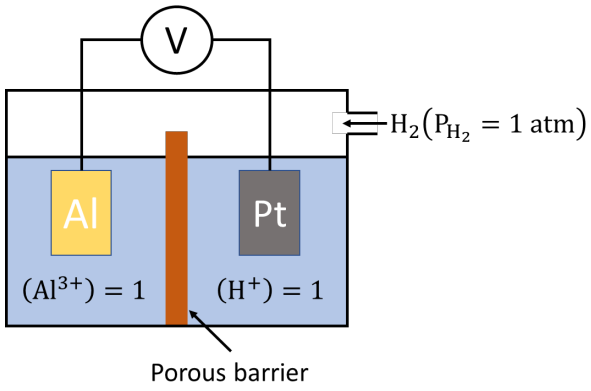

Figure 1.1 Schematic of the electrochemical cell setup measuring the standard equilibrium potential of Al.

Researchers established a convention to reflect the reaction activeness of a metal using the potential difference between the electromotive force potential of this metal and the potential of the standard hydrogen electrode (SHE). This is called the standard equilibrium potential, since it is the potential below which the reaction will happen in the direction of reduction and above which, oxidation. A schematic demonstrating the routine for measuring the equilibrium potential is plotted in **Figure *1.1***. Pt is often used as the counter electrode due to its inertness in the solution to supply the reaction site of hydrogen evolution reaction. The potential difference is thus measured between the Al oxidation and hydrogen evolution reaction and the standard equilibrium potential is obtained. The standard equilibrium potential of some commonly seen metals and cathodic counter reactions are listed in Table 1.

Table 1.1 List of equilibrium potential for reduction of commonly seen metals.

	Half reactions	Standard equilibrium potential (V vs SHE)
Noble	$Au^{3+} + 3e^- = Au$	+1.498
	$O_2 + 4H^+ + 4e^- = 2H_2O$ (pH 0)	+1.229
	$O_2 + 2H_2O + 4e^- = 4OH^-$ (pH 7)	+0.82
	$Ag^+ + e^- = Ag$	+0.799
	$Fe^{3+} + e^- = Fe^{2+}$	+0.771
	$Cu^{2+} + 2e^- = Cu$	+0.342
	$2H^+ + 2e^- = H_2$	0.000
	$Ni^{2+} + 2e^- = Ni$	-0.250
	$Fe^{2+} + 2e^- = Fe$	-0.447
	$Zn^{2+} + 2e^- = Zn$	-0.762
Active	$Al^{3+} + 3e^- = Al$	-1.662
	$Mg^{2+} + 2e^- = Mg$	-2.372

In actual corrosion environments, concentrations of participating ions will also affect the equilibrium potential. The equilibrium potential for half-cell reaction

$$a\mathrm{A} + m\mathrm{H}^+ + n\mathrm{e}^- = b\mathrm{B} + d\mathrm{H_2O} \tag{1.6}$$

considering the concentration effect could be calculated by Nernst equation

$$E = E_0 + \frac{2.3RT}{nF} log \frac{(\mathrm{A})^a(\mathrm{H}^+)^m}{(\mathrm{B})^b(\mathrm{H_2O})^d} \tag{1.7}$$

where E_0 stands for the standard equilibrium potential. (A) and (B) stands for the concentration of the species A and B respectively.

The relation between the corrosion rate and potential, namely the kinetics of the corrosion process, could be accounted for using Tafel equation, which is derived from Gibbs energy. The cathodic discharge reaction current density could be expressed as

$$i_c = -i_0 \times 10^{\eta/A_c} \tag{1.8}$$

where i_0 is the exchange current density, η is the overpotential and A_c is the cathodic Tafel slope. Similar relation calculating for anodic current density could be expressed as

$$i_a = i_0 \times 10^{\eta/A_a} \tag{1.9}$$

The total current could be obtained from the sum of the anodic and cathodic current. The total current is also written in the Butler-Volmer form:

$$i_{total} = i_c + i_a = i_0 \exp\left(\frac{\alpha_a nF\eta}{RT}\right) - i_0 \exp\left(\frac{\alpha_c nF\eta}{RT}\right) \tag{1.10}$$

and the α_a and α_c is called anodic and cathodic transfer coefficient respectively. Such relationship could be reflected by Figure 1.2. The cathodic half reaction is denoted by two blue straight lines, with the current density changing logistically with potential. The anodic half reaction is denoted by the red lines. The total current density is the absolute value of the difference between the current density of the cathodic half reaction happening in the oxygen reduction direction and the anodic half reaction happening in the metal dissolution direction. When measured experimentally, this kinetics is reflected by the polarization curve denoted as the black curve.

The corrosion rate could be calculated using the Faraday's law:

$$\mathrm{v_n} = \frac{\mathrm{i}_{loc}\mathrm{M}}{\mathrm{nF}\rho} \tag{1.11}$$

where M is the molar mass, n is the number of electrons transferred in dissolving 1 metal atom, F is the Faraday's constant (96485 C/mol), and ρ is the density of the metal.

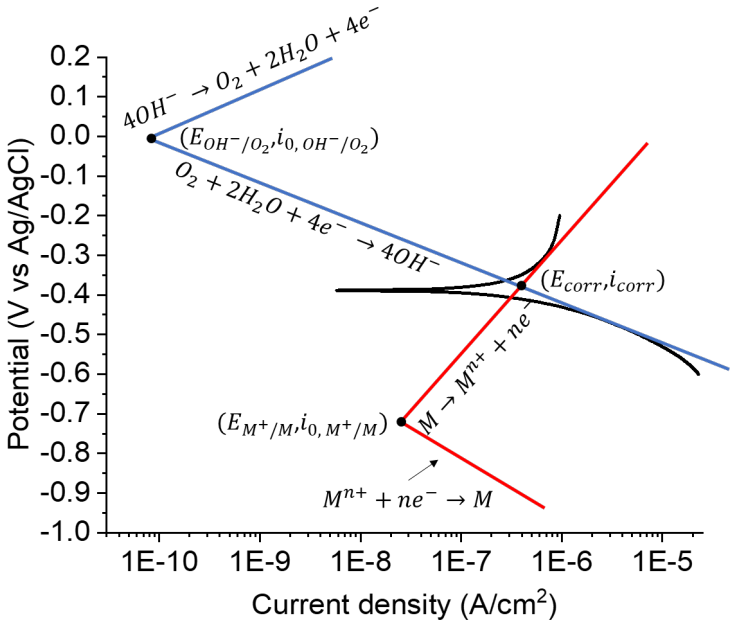

Figure 1.2 Polarization curve and corresponding anodic and cathodic half-cell reactions.

Another important aspect that affects the kinetics of metal corrosion apart from active corrosion is passivity. There is a group of metals, which are called passive metals, possessing a dense oxide layer at the surface, protecting the active metal surface from directly in contact with the corrosion environment. The existence of passive oxide layer lowers the overpotential, which acts as the driving force of the reaction, and blocks the corrosion current. Thus, such materials commonly possess good corrosion resistance. However, local defects, high concentration of specific ion species and mechanical damage can also jeopardize the integrity of the passive layer, expose the vulnerable metal surface and cause localized active corrosion [10].

1.1.3 Tribocorrosion

Tribocorrosion refers to the phenomenon of wear and corrosion synergy, which will lead to material loss different from the two of them acting alone. In most cases, accelerated material degradation is observed when there is tribocorrosion [11-16]. However, there are researches indicating that cases for negative synergistic effect also exist [17, 18].

Some researchers proposed the mechanism of accelerated material loss during tribocorrosion based on experimental observations [19-21]. A very representative research is conducted by Vieira et al. [22] investigating the tribocorrosion resistance of Al alloys in NaCl and NaNO3 solutions experimentally, followed by a theory capable of analytically predict the wear track area based on the galvanic coupling between the passive and depassivated area. In another experimental investigation on Al 7075-T6 alloys, Li et al. [23] proposed that the accelerated corrosion for samples under tribocorrosion is due to galvanic coupling between the worn region which is depassivated and the unworn region which is passive. While Martin et al. demonstrated that the crystallographic orientation has an influence on tribocorrosion using Ti-6Al-4V samples with different texture [24].

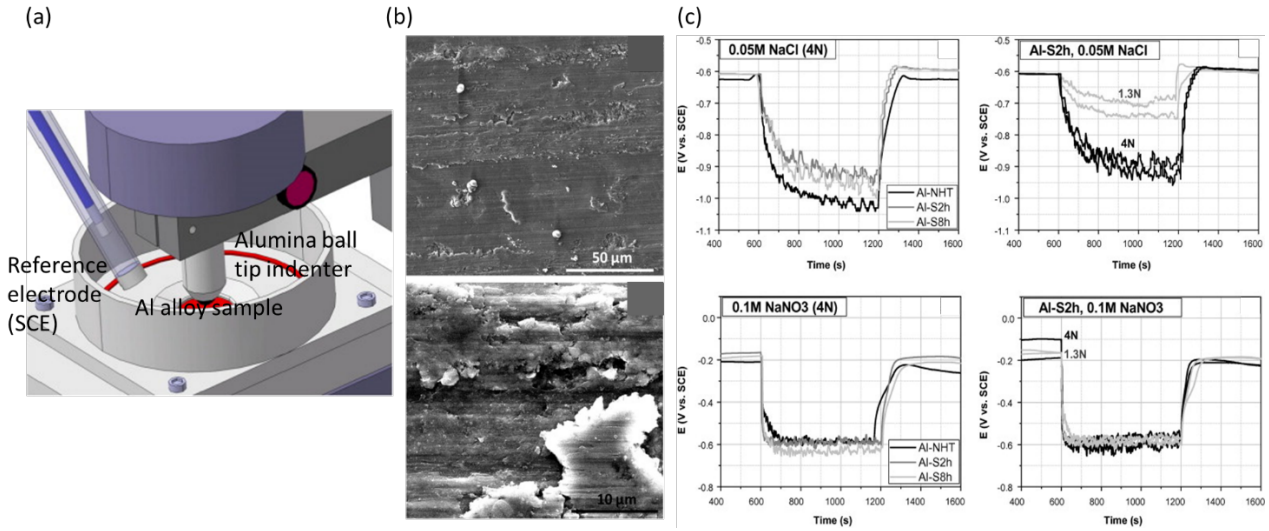

Figure 1.3 Experimental investigation of Al tribocorrosion by Vieira et al. [22]. (a) Schematic of the equipment for tribocorrosion test. (b) SEM images of the wear track of Al–10Si–4.5Cu–2Mg (wt.%) alloy sample after the tribocorrosion tests in 0.05 M NaCl solution. (c) Potential shift of samples caused by tribocorrosion.

Some theories have been proposed to explain the mechanism of accelerated corrosion during tribocorrosion of passive metals. First, wear could remove the passive layer at the surface. The exposed metal will suffer from active corrosion which leads to higher corrosion current and faster material loss. The repassivation could occur, restoring the passivity of the metal and slow down the corrosion rate again. Secondly, the scratching process may induce lattice rotation to the material, changing the local crystal orientation and inducing micro-galvanic coupling. Finally, the

plastic deformation caused by wear will increase the dislocation density, which will affect the thermal dynamic and the kinetics of the corrosion [25].

1.2 Finite element method in wear, corrosion, and tribocorrosion

Despite existing experimental research on tribocorrosion, it is time and resource consuming when the tribocorrosion behavior of a specific material needs to be evaluated, while the proposed theories and analytical models are either only qualitative or become incompetent in the case of complex geometries and structures. A numerical simulation method is needed to study the kinetics of the tribocorrosion process, provide quantitative support to the existing theories and predict tribocorrosion behavior, for example, tribocorrosion current and material loss. An ideal tool to solve this is the finite element analysis (FEA). The basic idea of FEA is meshing the geometry to small elements and using discrete form of differential equations to find solutions for physical models. has the advantage of capable of doing multiphysics couplings. FEA is proved to be very competent when simulating wear and corrosion, as well as multiphysics problems.

1.2.1 Wear simulation

Research has been done using FEA to investigate sliding wear of the materials [26-29]. Different mechanical parameters calculated in FEA are used to evaluate the wear track profile and material loss volume. Podra et al. combined the FEA with the Archard's law and used the contact pressure simulated in FEA to evaluate the wear depth [28]. Akchurin et al. used von Mises stress simulated in FEA as the criteria to evaluate wear debris size and obtain the material loss accordingly [30]. While Nelias et al. [31] and Bosman et al. [32] proposed a criteria based on plastic strain to predict wear volume, which is the method adapted and used in this project since it accommodates better with the case for severe running-in wear with hard indenter tip and a soft material.

1.2.2 Corrosion simulation

Corrosion is also widely simulated using FEA method. mainly focused on the galvanic coupling between different materials and the effect of ion diffusion [33-38]. Cross et al. modeled localized corrosion due to concentrated ion species [39] and galvanic coupling of multilayers and the optimization of such coatings materials [40] using COMSOL Multiphysics software. Deshpande et al. investigated the micro-galvanic corrosion of the different phase based on the microstructure of Mg alloys [34, 35]. The strong capability to simulate electrochemical problems coupled with ion diffusion, flow dynamics and galvanic coupling makes FEA a perfect tool to simulate corrosion.

1.2.3 Mechanical-electrochemical coupling

Although successful attempts have been made using FEA to simulate wear and corrosion of materials separately, finite element analysis of tribocorrosion which considers the coupling

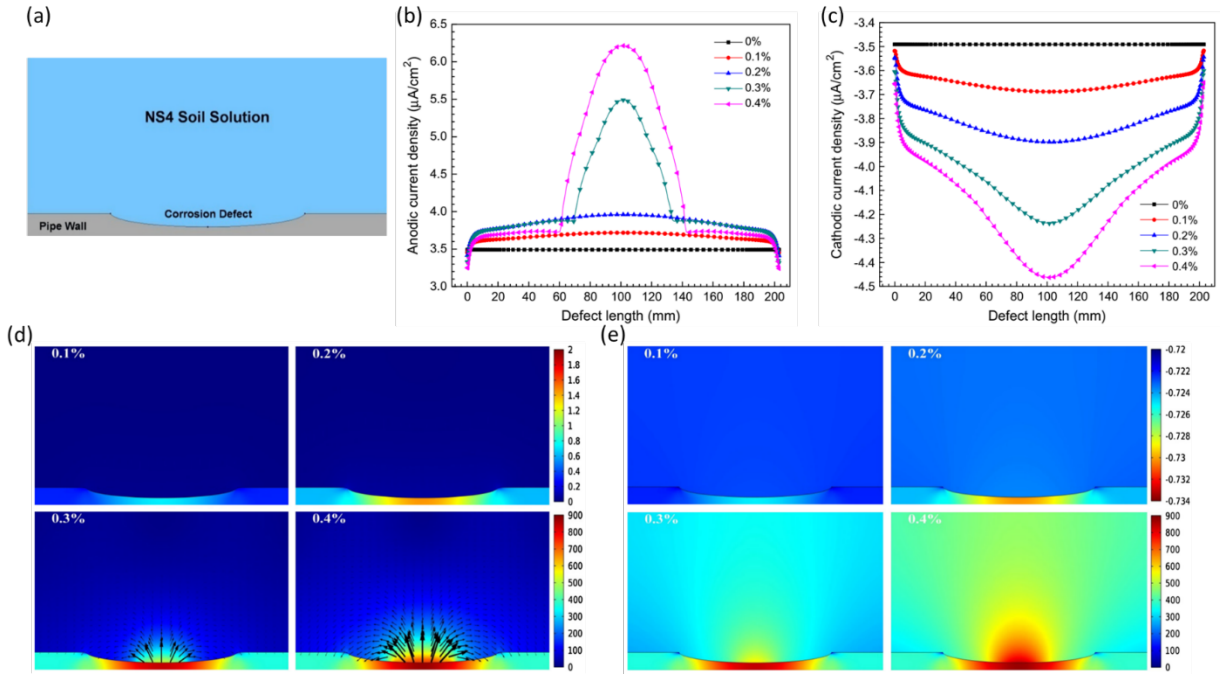

Figure 1.4 Finite element modeling of mechano-electrochemical effect of pipeline corrosion. (a) Model geometry reflecting a defect on a pipeline wall in the corrosive environment. Simulated (b) anodic and (c) cathodic current density along the surface of the wall under different strain level. (d) Potential distribution and (e) current density distribution inside the electrolyte in comparison with the Von Mises stress in the pipe wall under different strain level. [41]

between the mechanical and electrochemical effects is still a relatively unexplored field. One of the leading research projects involving the coupling of mechanics and electrochemistry was conducted by XF Cheng's group to investigate the stress corrosion of pipelines [41, 42]. The electrochemical status of the stressed pipeline surface was numerically analyzed based on Gutman's theory of stress corrosion [25] and some of the representative results are shown in Figure 1.4. However, the model doesn't account for material loss caused by wear. Nevertheless, these simulation attempts provide inspiration for using FEA to simulate wear-corrosion synergy in tribocorrosion phenomenon.

1.3 Research focus and goals

1.3.1 Material systems of interests

Due to its light weight and low cost, Al is widely used in transportation, batteries and marine infrastructures. Al exhibits excellent corrosion resistance due to the protection by its passive layer but is likely to lose the protection from the passive layer which is fragile to mechanical damage and expose of the inner active Al surface to corrosive environment [43]. Thus, the designing of aluminum-based materials with better wear resistance has great significance, not only to their mechanical integrity, but also to their corrosion resistance in mechanically hazardous environment.

Attempts to improve the tribocorrosion of Al-based systems have been made by alloying and engineering the microstructure of the material. A series of research projects have been carrying out on the Al-Mn alloys attempting to find optimized composition for best tribocorrosion performance [16, 44, 45]. By changing the percentage of Mn in the alloys, the mechanical and electrochemical properties of the alloys are modified and better tribocorrosion resistance is achieved. Another proven method to enhance the tribocorrosion resistance of the Al system is by forming metallic multilayers with another metal. In another work [46], Al was combined with Cu, Ti, Mg respectively to form nanostructured metallic multilayers. The Al/Cu multilayers shows the best tribocorrosion performance, unexpectedly surpassing that of Al/Ti. The combination of Al/Cu also improves the overall tribocorrosion resistance of the structure, making it better than bulk Al or Cu alone.

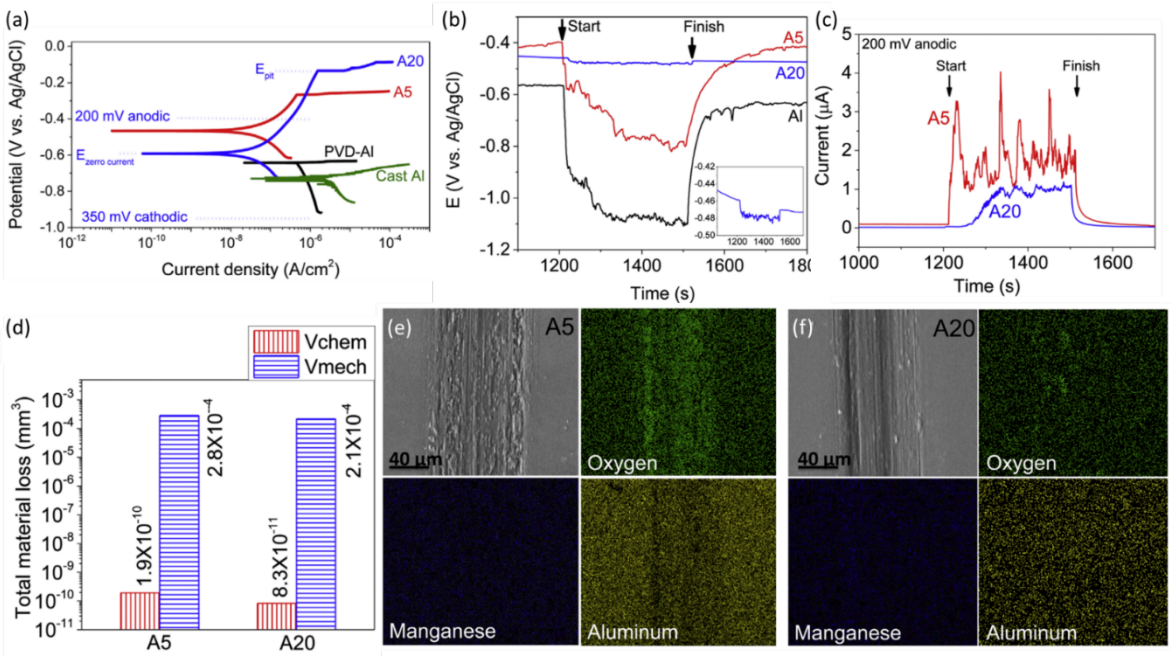

Figure 1.5 Results of tribocorrosion test and characterization of Al-Mn alloys. (a) Potential-dynamic curve of cast Al, PVD Al, A5 (Al alloy with 5 at.% Mn) and A20 (Al alloy with 20 at.% Mn) samples. (b) Negative shift of open-circuit potential during tribocorrosion. (c) Corrosion current increase caused by tribocorrosion. (d) Material loss caused by corrosion and wear under reciprocal tribocorrosion test. (e, f) SEM image and EDS characterization of the wear track of A5 and A20 sample.

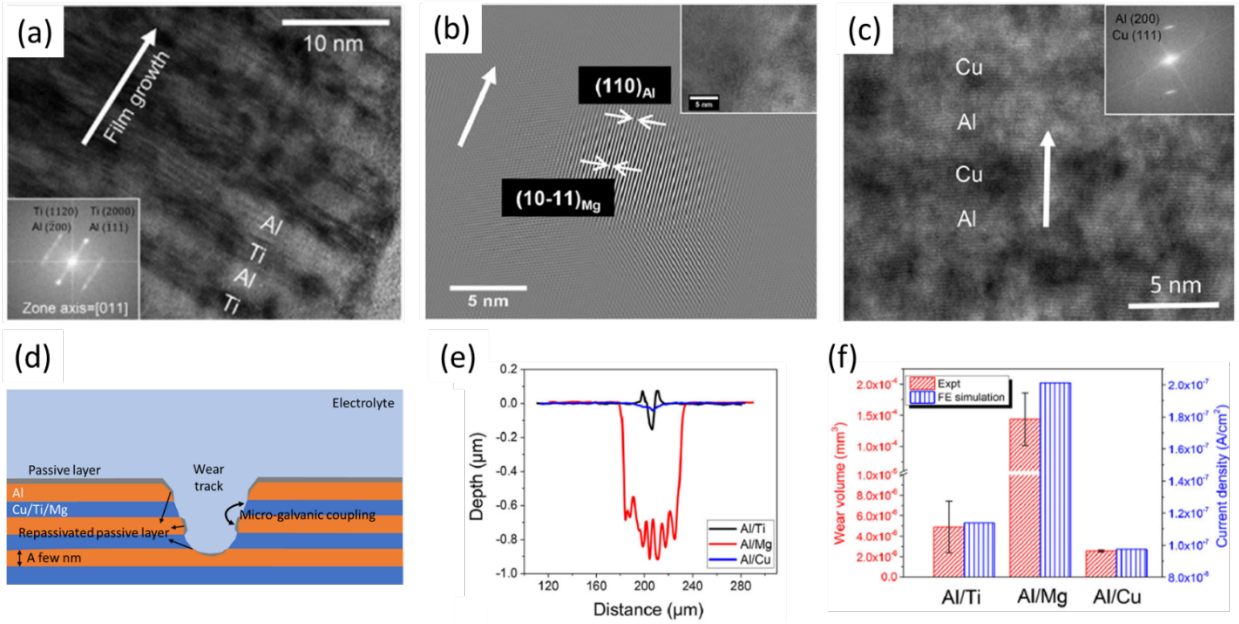

Figure 1.6 Improving tribocorrosion performance by nano-layering. (a-c) TEM images of the Al/Ti, Al/Mg and Al/Cu multilayers. (d) Schematic of the tribocorrosion process of the nano-multilayers. (e) Surface profile of the multilayers after tribocorrosion test. (f) Material loss volume measured from experiment and simulated by FE model. [46]

1.3.2 Research goals

The goal in this dissertation is to create a comprehensive FEA model to investigate the tribocorrosion phenomenon of Al, Al alloys and structures. The model aims to combine the existing contact mechanics model and stress corrosion model, along with an innovative wear evaluation algorithm, depassivation/repassivation model and crystallographic effect to account for the mechanical-electrochemical coupling. The models developed in this thesis is capable of analyzing the material's mechanical and electrochemical response to the tribocorrosion, predicting the volume loss and surface profile evolution and optimize the composition and structure design of materials. The experimental results of Al-Mn alloys, Al/Cu multilayers and pure Al were compared with the simulation results predicted by these case studies for validation purposes, focusing on the effect of alloy composition, microstructure and crystal orientation. The developed model will act as a steppingstone for more complicated tribocorrosion model and a guidance for future material optimization.

1.4 Organization of the dissertation

Study 1. Finite element modelling of the tribocorrosion of Al alloys with different composition (chapter 2)

The effect of material composition on tribocorrosion of bulk materials was investigated using a FE model developed with the consideration of abrasive wear, depassivation/repassivation effect and the coupling of electrochemical kinetics with plastic strain. The model was validated by experimental results of Al-Mn alloys and then used to investigate how Young's modulus, yield strength, exchange current density, and Tafel slopes affect the tribocorrosion resistance of bulk materials, which was summarized by a material loss map to guide the optimization of the tribocorrosion performance of alloys.

Study 2. Finite element modeling of the tribocorrosion behavior of Al/Cu nanostructured metallic multilayers (chapter 3)

A model was built to simulate the tribocorrosion of specially designed Al/Cu nanostructured metallic multilayers. The model successfully accounted for the improved tribocorrosion performance of the Al/Cu multilayers by galvanic coupling effect between Al and Cu. The effect of layer thickness and direction is studied, and the simulation results indicate that thinner layers lead to better tribocorrosion performance, the same as predicted by experiment.

Study 3. Understanding tribocorrosion of aluminum at the crystal level (chapter 4)

Indentation, electrochemical and tribocorrosion test were carried out on single crystal pure Al with different crystal orientations to obtain their mechanical, corrosion and tribocorrosion properties. The tribocorroded samples were characterized by EBSD to obtain the status of the samples in terms of lattice rotation and dislocation density. Different electrochemical parameters were assigned to different crystal orientations based on the EBSD map using a linear interpolation method. With the consideration of the depassivation-repassivation effect, crystal orientation effect and the dislocation density effect, the FE model successfully predicted the current surge during the tribocorrosion.

References

1. Kato, K., *Classification of wear mechanisms/models.* Proceedings of the Institution of Mechanical Engineers, Part J: Journal of Engineering Tribology, 2002. **216**(6): p. 349-355.
2. Davis, J.R., *Surface engineering for corrosion and wear resistance*. 2001: ASM international.
3. Murray, M.J., P.J. Mutton, and J.D. Watson, *Abrasive Wear Mechanisms in Steels.* Journal of Lubrication Technology-Transactions of the Asme, 1982. **104**(1): p. 9-16.
4. Archard, J.F. and W. Hirst, *The Wear of Metals under Unlubricated Conditions.* Proceedings of the Royal Society of London Series a-Mathematical and Physical Sciences, 1956. **236**(1206): p. 397-&.
5. Archard, J.F., *Contact and Rubbing of Flat Surfaces.* Journal of Applied Physics, 1953. **24**(8): p. 981-988.

6. Hokkirigawa, K. and K. Kato, *An Experimental and Theoretical Investigation of Plowing, Cutting and Wedge Formation during Abrasive Wear.* Tribology International, 1988. **21**(1): p. 51-57.
7. Kayaba, T., K. Hokkirigawa, and K. Kato, *Analysis of the Abrasive Wear Mechanism by Successive Observations of Wear Processes in a Scanning Electron-Microscope.* Wear, 1986. **110**(3-4): p. 419-430.
8. Challen, J. and P. Oxley, *An explanation of the different regimes of friction and wear using asperity deformation models.* Wear, 1979. **53**(2): p. 229-243.
9. Green, A.P., *The Plastic Yielding of Metal Junctions Due to Combined Shear and Pressure.* Journal of the Mechanics and Physics of Solids, 1954. **2**(3): p. 197-211.
10. Marcus, P., V. Maurice, and H.H. Strehblow, *Localized corrosion (pitting): A model of passivity breakdown including the role of the oxide layer nanostructure.* Corrosion Science, 2008. **50**(9): p. 2698-2704.
11. Pondicherry, K., D. Fauconnier, and P. De Baets, *Synergism in multi-asperity abrasion-corrosion of martensitic and dual phase steels in three aqueous electrolytes.* Wear, 2020. **452**.
12. Roy, S., et al., *Flow-induced failure mechanisms of copper pipe in potable water systems.* Corrosion Reviews, 2018. **36**(5): p. 449-481.
13. Kim, Y.S., et al., *Influence of a simulated deep sea condition on the cathodic protection and electric field of an underwater vehicle.* Ocean Engineering, 2018. **148**: p. 223-233.
14. Buciumeanu, M., et al., *Tribocorrosion behavior of hot pressed CoCrMo alloys in artificial saliva.* Tribology International, 2016. **97**: p. 423-430.
15. Mraied, H., W.B. Wang, and W.J. Cai, *Influence of chemical heterogeneity and microstructure on the corrosion resistance of biodegradable WE43 magnesium alloys.* Journal of Materials Chemistry B, 2019. **7**(41): p. 6399-6411.
16. Mraied, H. and W.J. Cai, *The effects of Mn concentration on the tribocorrosion resistance of Al-Mn alloys.* Wear, 2017. **380-381**: p. 191-202.
17. Bello, J.O., R.J.K. Wood, and J.A. Wharton, *Synergistic effects of micro-abrasion–corrosion of UNS S30403, S31603 and S32760 stainless steels.* Wear, 2007. **263**(1-6): p. 149-159.

18. Thakare, M.R., et al., *Exposure effects of strong alkaline conditions on the microscale abrasion–corrosion of D-gun sprayed WC–10Co–4Cr coating.* Tribology International, 2008. **41**(7): p. 629-639.
19. Jemmely, P., S. Mischler, and D. Landolt, *Tribocorrosion behaviour of Fe-17Cr stainless steel in acid and alkaline solutions.* Tribology International, 1999. **32**(6): p. 295-303.
20. Stojadinovic, J., et al., *Effect of electrode potential on the tribocorrosion of tungsten.* Tribology International, 2009. **42**(4): p. 575-583.
21. Cao, S.F., S.G. Maldonado, and S. Mischler, *Tribocorrosion of passive metals in the mixed lubrication regime: theoretical model and application to metal-on-metal artificial hip joints.* Wear, 2015. **324**: p. 55-63.
22. Vieira, A.C., et al., *Mechanical and electrochemical deterioration mechanisms in the tribocorrosion of Al alloys in NaCl and in NaNO3 solutions.* Corrosion Science, 2012. **54**: p. 26-35.
23. Li, Z.Y., H.Y. Yu, and D.B. Sun, *The tribocorrosion mechanism of aluminum alloy 7075-T6 in the deep ocean.* Corrosion Science, 2021. **183**.
24. Martin, E., et al., *Influence of microstructure and texture on the corrosion and tribocorrosion behavior of Ti-6Al-4V.* Tribology International, 2010. **43**(5-6): p. 918-924.
25. Gutman, E.m.M., *Mechanochemistry of solid surfaces*. 1994, Singapore ; River Edge, NJ: World Scientific. ix, 322 p.
26. Walter, C., et al., *Finite element simulation of the effect of surface roughness on nanoindentation of thin films with spherical indenters.* Surface & Coatings Technology, 2007. **202**(4-7): p. 1103-1107.
27. Hegadekatte, V., N. Huber, and O. Kraft, *Finite element based simulation of dry sliding wear.* Modelling and Simulation in Materials Science and Engineering, 2005. **13**(1): p. 57-75.
28. Podra, P. and S. Andersson, *Simulating sliding wear with finite element method.* Tribology International, 1999. **32**(2): p. 71-81.
29. Woldman, M., et al., *A Finite Element Approach to Modeling Abrasive Wear Modes.* Tribology Transactions, 2017. **60**(4): p. 711-718.

30. Akchurin, A., R. Bosman, and P.M. Lugt, *A Stress-Criterion-Based Model for the Prediction of the Size of Wear Particles in Boundary Lubricated Contacts.* Tribology Letters, 2016. **64**(3).
31. Nélias, D., V. Boucly, and M. Brunet, *Elastic-Plastic Contact Between Rough Surfaces: Proposal for a Wear or Running-In Model.* Journal of Tribology, 2006. **128**(2): p. 236-244.
32. Bosman, R. and D.J. Schipper, *Transition from mild to severe wear including running in effects.* Wear, 2011. **270**(7-8): p. 472-478.
33. Cross, S.R., S. Gollapudi, and C.A. Schuh, *Validated numerical modeling of galvanic corrosion of zinc and aluminum coatings.* Corrosion Science, 2014. **88**: p. 226-233.
34. Deshpande, K.B., *Numerical modeling of micro-galvanic corrosion.* Electrochimica Acta, 2011. **56**(4): p. 1737-1745.
35. Deshpande, K.B., *Validated numerical modelling of galvanic corrosion for couples: Magnesium alloy (AE44)-mild steel and AE44-aluminium alloy (AA6063) in brine solution.* Corrosion Science, 2010. **52**(10): p. 3514-3522.
36. Wang, Y.C., et al., *Numerical Simulation of Micro-Galvanic Corrosion in Al Alloys: Steric Hindrance Effect of Corrosion Product.* Journal of the Electrochemical Society, 2017. **164**(14): p. C1035-C1043.
37. Yin, L.T., et al., *Numerical Simulation of Micro-Galvanic Corrosion of Al Alloys: Effect of Chemical Factors.* Journal of the Electrochemical Society, 2017. **164**(13): p. C768-C778.
38. Yin, L.T., et al., *Numerical simulation of micro-galvanic corrosion of Al alloys: Effect of density of Al(OH)(3) precipitate.* Electrochimica Acta, 2019. **324**.
39. Cross, S.R. and C.A. Schuh, *Modeling localized corrosion with an effective medium approximation.* Corrosion Science, 2017. **116**: p. 53-65.
40. Cross, S.R., et al., *Computational design and optimization of multilayered and functionally graded corrosion coatings.* Corrosion Science, 2013. **77**: p. 297-307.
41. Xu, L.Y. and Y.F. Cheng, *Development of a finite element model for simulation and prediction of mechanoelectrochemical effect of pipeline corrosion.* Corrosion Science, 2013. **73**: p. 150-160.
42. Xu, L.Y. and F. Cheng, *A finite element based model for prediction of corrosion defect growth on pipelines.* International Journal of Pressure Vessels and Piping, 2017. **153**: p. 70-79.

43. Mischler, S., S. Debaud, and D. Landolt, *Wear-accelerated corrosion of passive metals in tribocorrosion systems.* Journal of the Electrochemical Society, 1998. **145**(3): p. 750-758.
44. Chen, J. and W.J. Cai, *Effect of scratching frequency on the tribocorrosion resistance of Al-Mn amorphous thin films.* Wear, 2019. **426**: p. 1457-1465.
45. Mraied, H., W.J. Cai, and A.A. Sagues, *Corrosion resistance of Al and Al-Mn thin films.* Thin Solid Films, 2016. **615**: p. 391-401.
46. Wang, W., et al., *Ultrahigh tribocorrosion resistance of metals enabled by nano-layering.* Acta Materialia, 2021. **206**.

Chapter 2. Finite element modelling of the tribocorrosion of Al alloys with different composition

This chapter is based on the following published paper in Corrosion Science and reprinted with permission.

K. Wang, Y. Wang, X. Yue, W. Cai, "Multiphysics modeling and uncertainty quantification of tribocorrosion in aluminum alloys", Corrosion Science 178, 109095 (2021)
https://doi.org/10.1016/j.corsci.2020.109095.

2.1 Introduction

The design of robust and reliable metals and alloys that are simultaneously wear and corrosion resistant is crucial for various applications such as oil and gas pipelines, underwater vehicles, batteries, and biomedical devices where high mechanical stress and corrosive environment coexist [1-6]. During tribocorrosion, the coupling of stress (either external or residual) and corrosion is a major potential threat to jeopardize materials' long-term sustainability and structural integrity. The stresses at the contacting asperities not only plastically deform the surface material, leading to the formation of wear debris, tribolayer, and mechanically deformed layer, but also enhance localized corrosion on the wear track [7-9]. Such wear-corrosion synergy is especially significant for passive metals such as aluminum (Al) alloys, which relies on the presence of an ultrathin (~ a few nm) surface oxide layer (i.e., passive layer) for corrosion protection under passivating conditions (e.g., neutral aqueous solution for Al) [8, 10]. When this delicate passive layer is mechanically removed, the wear-corrosion synergy has often been found to enhance the corrosion process and accelerate total material loss [1, 11-14], although the opposite has also been reported [15, 16]. For example, Jemmely et al. [11] reported an experimental investigation on the tribocorrosion behavior of Fe–17Cr stainless steel under reciprocal wear using alumina pin as a counter body in acid and alkaline solutions. They found that the interdependence of the mechanical and the electrochemical response is affected by the solution pH, in which the metal exhibited different repassivation behavior. Vieira

et al. [14] studied the tribocorrosion resistance of Al alloys in NaCl and $NaNO_3$ solutions and proposed a theory attributing the enhanced localized corrosion to the galvanic coupling between the passive area and depassivated wear track during tribocorrosion. While many studies reported a positive wear-corrosion synergy, the opposite has also been reported. For example, Bello et al. [15] observed a negative synergy in S31603 and S32760 stainless steels under a low abrasion rate. It was argued that under such conditions, the tribocorrosion material loss is smaller than that of pure wear condition due to the simultaneous mechanical and electrochemical attack, where corrosion-induced passive film on the surface reduced the overall two-body abrasion.

So far, most works focus on experimental study and phenomenological modeling of tribocorrosion [12], only limited work has been done to develop a numerical simulation framework that couples materials' mechanical and electrochemical responses as well as their synergy. Despite limited research, several studies have been carried out to investigate wear [17-20], corrosion [21-24], and stressed corrosion [25-27] of metals and alloys using finite element analysis (FEA) based methods. For example, Xu et al. published a series of works [25, 26] investigating the corrosion of steel in pipelines under tensile stress using FEA methods. Wang et al. created a model using a combination of cellular automata and FEA methods for metastable pitting corrosion under mechanical stress [27]. However, such models cannot be directly applied to tribocorrosion, where the material degradation and deformation is multi-physics in nature, requiring consideration of the time-dependent surface evolution and material loss caused by elastic/plastic deformation, corrosion, and stress-corrosion synergy on the wear track. This work aims to develop an experimentally validated computational framework to model and predict tribocorrosion behavior of metals, using Al alloys as examples. It is believed that the developed model, material property extraction, validation, and uncertainty quantification processes can be extended to metal systems beyond Al alloys in future studies.

Due to its lightweight, high specific strength, and good corrosion resistance, Al alloys have been heavily used in seawater such as offshore infrastructures, ships, and undersea vehicles, whose structural integrity and useful lifetime rely heavily on the tribocorrosion properties of the alloy [28, 29]. The pure corrosion mechanism of Al in seawater (often approximated as neutral 0.6 M NaCl solution) has been subjected to extensive prior study [8, 30]. Despite diverse corrosion kinetics that is heavily dependent on their composition and microstructure, the thermodynamics of Al alloy corrosion is well understood. The anodic reaction is mainly aluminum oxidation, expressed as

$Al = Al^{3+} + 3e^-$, which has a standard equilibrium potential of -1.662V (vs. SHE) [31]. The cathodic reaction is governed by oxygen reduction in neutral solution via $O_2 + 2H_2O + 4e^- = 4OH^-$, with a standard equilibrium potential of 0.82V [31]. According to Nernst equation, the equilibrium potential of aluminum oxidation is affected by the concentration of aluminum ions following the equation:

$$E_{\frac{Al}{Al^{3+}}} = -1.66 + \frac{0.059}{3}\log(Al^{3+}), \tag{2.1}$$

and the equilibrium potential of oxygen reduction is affected by the pH of the solution following

$$E_{\frac{H^+}{H2}} = 0.82 - 0.059pH. \tag{2.2}$$

The corrosion kinetics of Al and its alloys is often measured experimentally using polarization methods. For example, Fig. 2.1 demonstrates the potentiodynamic polarization curve of pure Al in neutral 0.6 M NaCl. Assuming the electrochemical reaction takes place directly on the metal and the system has only one time constant, given the theoretical equilibrium potential (i.e. E_a and E_c for the anodic and cathodic reaction respectively), kinetic parameters such as Tafel slopes and exchange current densities (i_a and i_c) of the reactions could be obtained.

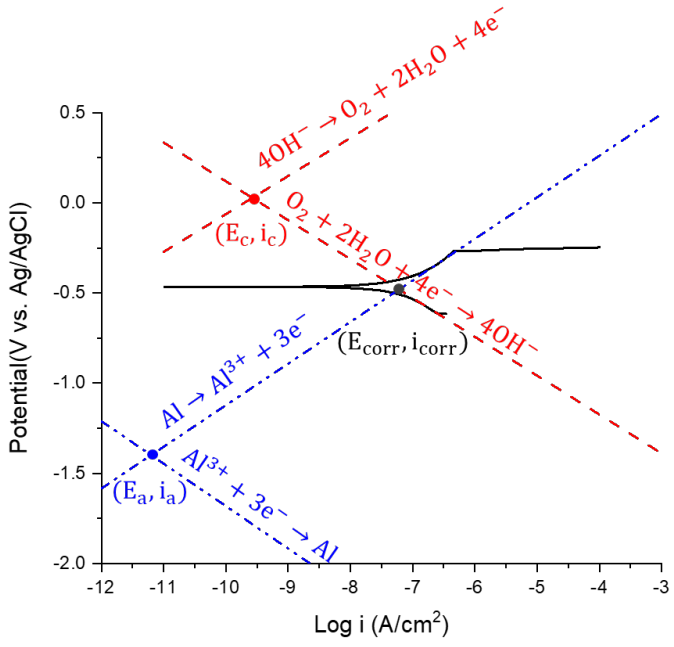

Figure 2.1 Typical potentiodynamic polarization curve of Al corrosion in 0.6 M NaCl at pH=6.4.

During tribocorrosion of Al alloys in seawater, our prior work showed that both alloy composition and testing parameters affect the overall tribocorrosion kinetics [6, 28]. Briefly, two tribocorrosion resistant Al-Mn alloys were prepared by magnetron sputtering with 5.2 at% and 20.5 at% Mn (named A5 and A20 respectively hereafter). Both the mechanical strength and corrosion resistance of Al increased with Mn% content in the alloy. During the tribocorrosion test in 0.6 M NaCl solution with a pH of ~ 6.4, it was found that when the surfaces of the samples were scratched, the open circuit potential experienced a cathodic shift and the current flowing through the electrode/electrolyte interface increased, indicating a positive wear-corrosion synergy. In addition, A20 experienced less wear-corrosion synergy and higher repassivation rate than that of A5. In a follow-up study [28], it was found that the total tribocorrosion rate, including both mechanical and chemical wear, increased with increasing scratching frequency (hence depassivation rate). The percentage of depassivated area on the wear track of A20 decreased from 70% to 63% when the sliding frequency was increased from 0.1 Hz to 1 Hz.

The goals of this work are to (1) develop an experimentally validated finite element based multiphysics model to quantify the effects of materials' mechanical and electrochemical properties on their tribocorrosion behavior, (2) evaluate the effects of applied surface stress as well as residual subsurface stress/strain on the corrosion kinetics, (3) develop a tribocorrosion map for material loss prediction based on both mechanical (e.g., elastic modulus and yield strength) and electrochemical (e.g., Tafel slopes) properties, and (4) quantify the FEA model uncertainty using surrogate models. In the present work, the developed FEA model will be validated using A5 and A20, whose corrosion, mechanical, and tribocorrosion properties have been well characterized by our prior experimental work [6, 28, 32]. In addition, the difference in alloy composition between the two allows the evaluation of different mechanical and corrosion properties on the overall tribocorrosion response. This model differs from existing phenomenological models in a way that it considers not only the dynamic process of scratching, but also the time-dependent evolution of the dissolving surface during tribocorrosion. The model paves way for a numerical method of investigating materials' tribocorrosion resistance, which could be further developed to analyze the reliability of structures and devices under extreme conditions where stress and corrosion coexist. Finally, since materials' behavior during tribocorrosion is complicated and nonlinear, uncertainty quantification (UQ) was carried out to evaluate the accuracy of the FEA model. Traditionally, Monte Carlo simulation [33] is considered as a standard approach to implementing UQ in the

simulation of complex nonlinear systems. This method will repeat simulations multiple times assuming different values of unknown input parameters, which makes the computational cost grow significantly when the system has a large number of unknown parameters (e.g., various mechanical and electrochemical properties in tribocorrosion). To reduce the computation cost, two data-driven surrogate models, Gaussian Process (GP) [34] and Neural Network (NN) with dropout [35], were used here to evaluate the UQ of the developed FEA simulations [36, 37]. The structure of the paper is as follows. FEA model setup is presented in Section 2.2. Section 2.3 discusses the procedures for extracting material properties from experiments. Section 2.4 summarizes FEA model results and validation from theories and prior experiments. Section 2.5 discusses the uncertainty quantification study. Concluding remarks are presented in Sections 2.6.

2.2 FEA model setup

2.2.1 Model geometry setup and meshing

FEA models were developed using the COMSOL Multiphysics software of version 5.3. The simulation contains three parts: nanoindentation, corrosion, and tribocorrosion. The first part is required to simulate the nanoindentation behavior of the alloys to correctly extract key mechanical properties of the alloy, Young's modulus and hardness, which are then used as inputs in the tribocorrosion model. It is noted here while these properties are typically reported from experimental measurements using the Oliver-Pharr method [38], it is shown later in section 2.3, that directly using such values leads to measurable discrepancies between simulated and measured load-displacement curves. The second part considers pure corrosion of the indented surface, and the third part simulates material loss due to simultaneous scratch and corrosion.

Fig. 2.2 shows the geometry and meshing of the simulation. A conical diamond tip with a radius of 1 μm and an alumina ball tip with a radius of 2 mm were used for the indentation and tribocorrosion test, respectively, in consistent with the experiments. 2D axisymmetric model was used to save computational time and resource for indentation simulation. As shown in Fig. 2.2(b), the conical indenter with a semiapical angle of 70.3° was smoothed at the tip using the fillet option [39]. For tribocorossion, a ball-on-plate configuration shown in Fig. 2.2(c) was used for the 3D model geometry. Both dimensions of the counter body and sample were the same as those from

experiments. The 3D FE model was simulated by half in geometry due to the presence of mirror symmetry along the symmetry (x-z) plane (Fig. 2.2(d)). Friction coefficient for both samples is set to be 0.6, as measured from experiment. The meshing schemes are shown in Fig. 2.2(b) and (d), where mesh size increases from the contact areas to areas far away. Specifically, for the indentation model, triangular mesh of 0.02~0.05 μm was used in the contact area and 0.2 μm far away. For the tribocorrosion model, the mesh size was 0.1 mm in the contact area and 0.5 mm far away. All meshing sizes were chosen after convergence analysis by balancing computational time and model accuracy where further reducing the mesh size does not affect the simulation results.

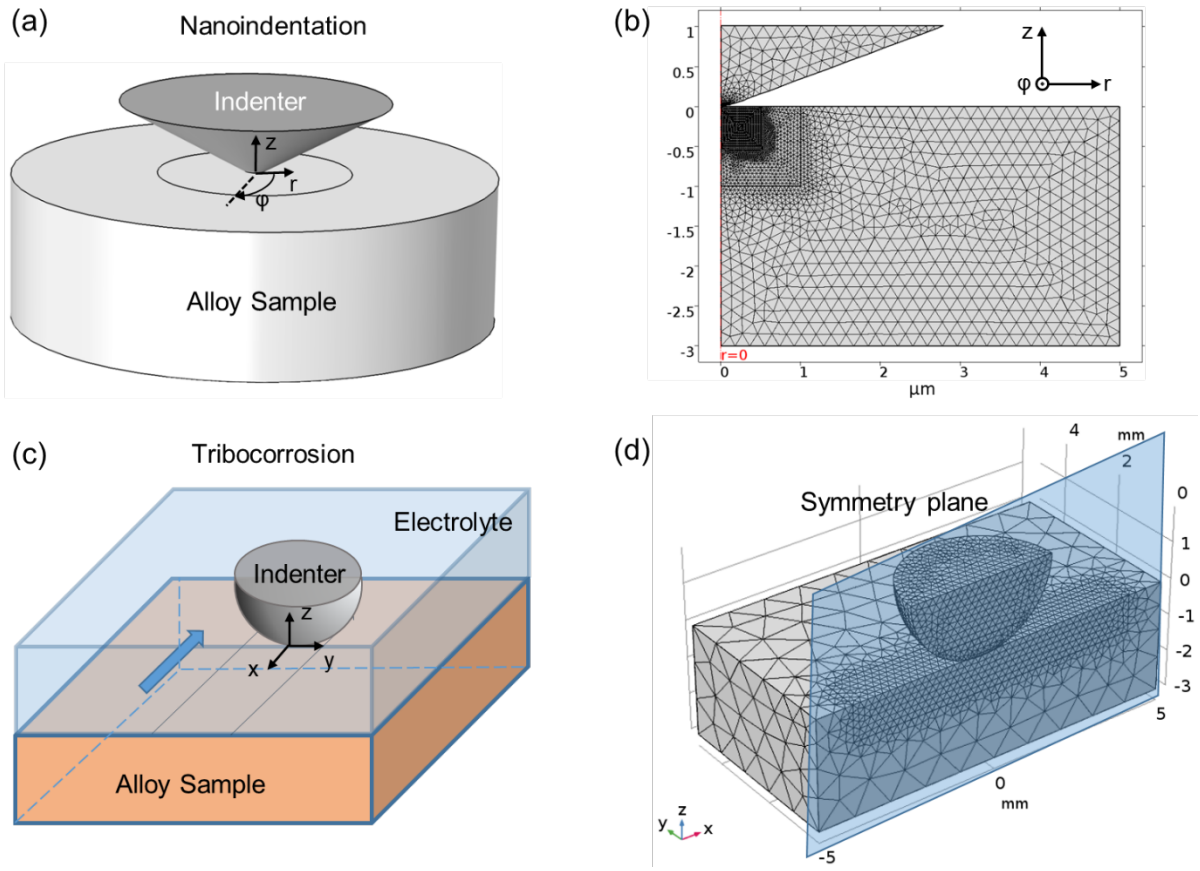

Figure 2.2 (a, c) Schematic and (b, d) FEA meshing setup of the nanoindentation and tribocorrosion test model.

2.2.2 Equations and boundary conditions for contact mechanics

With the meshed geometry, mechanical module within COMSOL was applied to investigate the stress and strain responds to the external force. The contact problems are solved by defining a

contact pair with a source boundary, which is the boundary of the harder material typically, and a destination boundary, which is the softer material in comparison. The normal contact pressure between destination and source boundaries is matched using the augmented Lagrangian method.

The Al alloy and indenter are modeled as elastic-perfectly plastic materials with no strain hardening during plastic deformation. The correlation between stress and strain within the elastic limit of the material could be expressed as:

$$\begin{bmatrix} \sigma_x \\ \sigma_y \\ \sigma_z \\ \sigma_{xy} \\ \sigma_{yz} \\ \sigma_{xz} \end{bmatrix} = D\left(\begin{bmatrix} \varepsilon_x \\ \varepsilon_y \\ \varepsilon_z \\ \varepsilon_{xy} \\ \varepsilon_{yz} \\ \varepsilon_{xz} \end{bmatrix} - \begin{bmatrix} \varepsilon_x \\ \varepsilon_y \\ \varepsilon_z \\ \varepsilon_{xy} \\ \varepsilon_{yz} \\ \varepsilon_{xz} \end{bmatrix}_{inel} \right), \tag{2.3}$$

where σ and ε stands for the 3D stress and strain components, ε_{inel} stands for the inelastic part of the strain, and D is the elasticity tensor defined as a function of elastic modulus (E) and Poisson's ratio (ν) as:

$$D = \frac{E}{(1+\nu)(1-2\nu)} \begin{pmatrix} 1-\nu & \nu & \nu & 0 & 0 & 0 \\ \nu & 1-\nu & \nu & 0 & 0 & 0 \\ \nu & \nu & 1-\nu & 0 & 0 & 0 \\ 0 & 0 & 0 & \frac{1-2\nu}{2} & 0 & 0 \\ 0 & 0 & 0 & 0 & \frac{1-2\nu}{2} & 0 \\ 0 & 0 & 0 & 0 & 0 & \frac{1-2\nu}{2} \end{pmatrix}. \tag{2.4}$$

The yield surface was calculated using von Mises criterion, which could be generally expressed as

$$F = \sqrt{3J_2} - \sigma_y = 0. \tag{2.5}$$

In eqn. (5), the first term is the von Mises stress, in which $J_2 = \frac{1}{6}\Big((\sigma_x - \sigma_y)^2 + (\sigma_y - \sigma_z)^2 + (\sigma_z - \sigma_x)^2 \Big) + \sigma_{xy}^2 + \sigma_{yz}^2 + \sigma_{xz}^2$, and the second term is the yield strength (σ_y). The load is defined using the surface integration reaction pressure on the top surface of the indenter, imposed using auxiliary sweep method with a total of 10 steps of equal increment and decrement respectively in the range of 0 to the maximum load to simulate a quasi-dynamic process. The bottom boundary of the sample is set as a fixed constraint with no normal displacement.

2.2.3 Material removal by abrasive wear

After simulating the sliding contact, a strain-based material removal model was applied to simulate the wear debris generation process where contacting asperities experience highly plastic deformation and detach from the bulk. Following that proposed by Nélias et al. [40] and Bosman et al. [41], it is assumed that material removal would occur when the plastic strain ε_p exceeds a critical value ε_c. In this work, ε_c is chosen to be 0.05, which is the threshold when material experience transition from small strain deformation to severe wear [40]. The algorithm is realized by assessing the state of every element starting from that closest to the surface along the -z direction. If the obtained ε_p is larger than ε_c, the element is considered as a worn element and removed. The same process was then repeated on the element beneath it until an element with $\varepsilon_p < \varepsilon_c$ was found (unworn element). The final worn track surface profile is obtained after all surface locations are evaluated using this method.

2.2.4 Equations and boundary conditions for corrosion

The current density ($\boldsymbol{i}$) and the electrolyte potential (ϕ) satisfy the differential equations of:

$$\begin{cases} \nabla \cdot \boldsymbol{i_l} = Q_l \\ \boldsymbol{i_l} = -\sigma_l \nabla \phi_{elec} \end{cases}, \tag{2.6}$$

where Q_l is the charge density in the solution, which is 0 in a solution with equal positive and negative ions. σ_l is the conductivity of the solution, which is 0.05 S/m for 0.6 NaCl aqueous solution. At the electrolyte/electrode interface, the local current density (i_{loc}) was assumed to satisfy the Tafel equation:

$$i_{loc} = 10^{\frac{\eta}{A}} i_0, \tag{2.7}$$

in which the overpotential (η) is defined as $\eta = \phi_{ext} - \phi_{elec} - E_{eq}$. ϕ_{ext} is the external potential connected to the metal, which is 0 V in our case. ϕ_{elec} is the electrolyte potential and E_{eq} is the corresponding equilibrium potential of the reaction happened at this interface. The boundary

conditions at the interface are expressed as

$$\begin{cases} \phi_{ext} = 0 \\ \mathbf{n} \cdot \boldsymbol{i_l} = \sum_m i_{loc,m} \end{cases}. \tag{2.8}$$

Once the local current distribution is calculated by solving the equations above, the dissolution speed normal to the metal surface ($\mathrm{v_n}$) is calculated according to Faraday's laws:

$$\mathrm{v_n} = \frac{\mathrm{i}_{loc}\mathrm{M}}{\mathrm{nF}\rho}, \tag{2.9}$$

where M is the molar mass, n is the number of electrons transferred in dissolving 1 metal atom, F is the Faraday's constant (96485 C/mol), and ρ is the density of the metal. The electrolyte-electrode interface was set as a free-deforming surface while the other boundaries of the sample are non-deforming ones which doesn't allow normal displacement. The elements on the free-deforming surface shrink according to the calculated dissolution speed from eqn. (2.9).

The depassivation and repassivation process was simulated using the thickness-dependent electrical resistor property of the surface film. The conductivity of the intact surface film (σ) was set to be $1 \times 10^{-12} S/m$, corresponding to that of Al_2O_3. The initial film thickness is set to be 4 nm, as observed in experiments [42]. During scratch induced depassivation, this thin layer is assumed to be destroyed on the wear track. In the subsequent repassivation, the film thickness grows from zero according to the dissolution rate and the electrical resistance at the surface increases. Suppose the corroded thickness of Al at a certain location and time is d, the accumulated passive layer thickness is $1.29d$, calculated from their molar volume ratio (i.e. M_{Al2O3}/M_{Al}). A resistant barrier with local conductivity per unit area of $1.29\sigma d$ is applied.

2.2.5 Wear-corrosion synergy and tribocorrosion

The wear-corrosion synergy during tribocorrosion was modeled by incorporating the change in electrochemical performance caused by mechanical deformation. Specifically, the anodic potential (φ_a) is assumed to shift cathodically from its equilibrium value (φ_{a0}) depending on the elastic and plastic strain following [25, 43]:

$$\varphi_a = \varphi_{a0} - \frac{\sigma V_m}{nF} - \frac{TR}{nF} \ln\left(K_\alpha\left(\varepsilon_p\right)\right), \tag{2.10}$$

where the second and third term is the shift of equilibrium potential due to elastic and plastic deformation respectively. In eqn. (11), the stress σ is taken as the stress within the elastic deformation and for the area that is plasticly deformed, it equals to the yield strength, V_m is the molar volume of aluminum ($V_m = 9.99 \times 10^{-6} m^3/mol$), T is temperature (T=298 K at room temperature), R is the ideal gas constant (R=8.3145J/(mol · K)), ε_p is the effective plastic strain, and $K_\alpha(\varepsilon_p)$ is a function denoting the dislocation density increment under plastic strain (ε_p), obtained by interpolating data from [44].

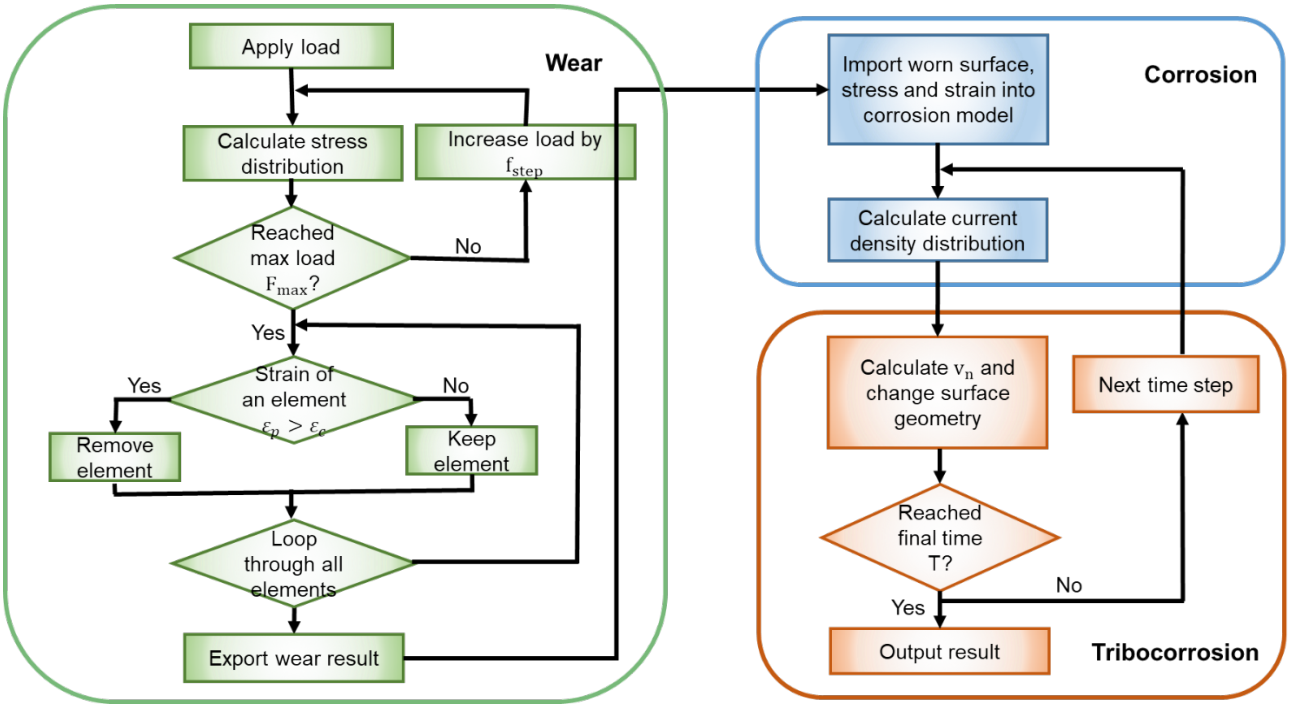

Figure 2.3 Flowchart of the FEA tribocorrosion model.

The flowchart of the whole tribocorrosion model is illustrated in Fig. 2.3. In the simulation for tribocorrosion test, the deformed surface geometry and plastic strain after unloading obtained from wear simulation was imported as input to calculate φ_a following the eqn. (11) above at each single location on the sample surface. All the other parameters and settings are the same as the pure corrosion model.

2.3 Extraction of material properties from experiments

2.3.1 Extraction of mechanical properties

Prior nanoindentation results of A5 and A20 are used to extract Young's modulus (E) and hardness (H) of both samples. As shown in Fig. 2.4(a), directly using E and H values obtained experimentally from the Oliver and Pharr method (listed in Table 1) leads to a large discrepancy between the experimental and simulated load-displacement curves. An accurate capture of such relationship is critical to model tribocorrosion, during which each location along the wear track experiences cyclic loading and unloading as the indenter passes through.

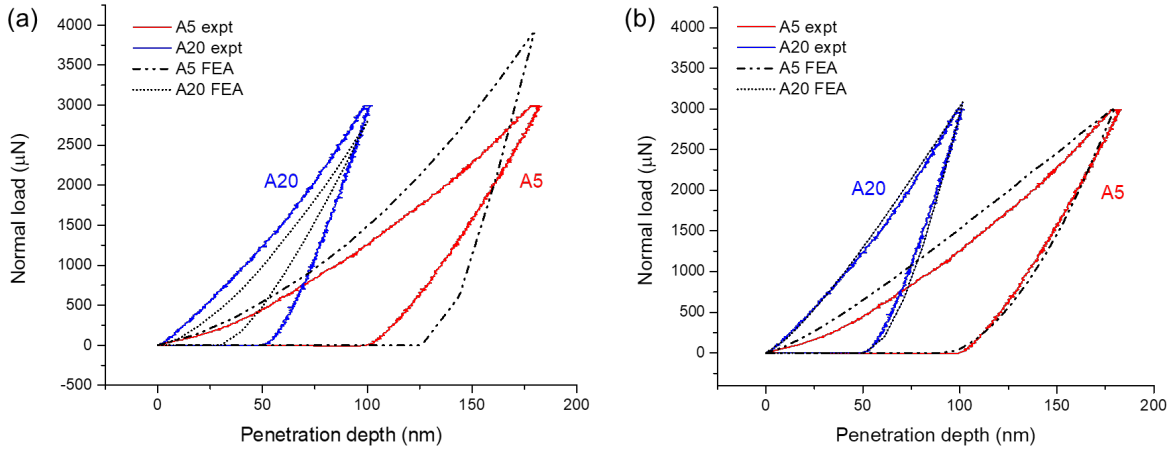

Figure 2.4 Comparison of nanoindentation load-displacement curves between experiments and FEA simulations for A5 and A20 samples using (a) experimentally obtained, and (b) FEA fitted mechanical property data.

To extract the mechanical properties that can be used in the FEA indentation simulation to reproduce the experimentally measured load-displacement curves, the following procedure was developed using the optimization module of COMSOL. Starting from an initial guess of E and σ_y, a corresponding load-displacement curve is generated through FEA simulation. The sum of the square of the difference between experimental and FEA simulation results at assigned data point is called the least-square objective. The parameters that minimize the least-square objective were found using BOBYQA method in the optimization module. Finally, these fitted E and H values are shown in Table 2.1 for A5 and A20. Fig. 2.4(b) demonstrates good agreement between experiment and simulation by using these fitted parameters. Such mechanical properties are then used in the tribocorrosion simulation in section 4.

Table 2.1 Summary of mechanical properties from experiments and FEA simulation. E and σy represents elastic modulus and yield strength respectively.

Sample ID	Experiment		FEA simulation	
	E (GPa)	σ_y (GPa)	E (GPa)	σ_y (GPa)
A5	77.65	0.53	55.11	1.26
A20	97.54	1.80	108.83	2.59

2.3.2 Extraction of corrosion properties

The corrosion properties of Al alloys were extracted from the experimentally measured polarization curves of A5 and A20, as shown in Fig. 2.5. Because all potentials were measured versus a Ag/AgCl reference in the experiment, all potential is reported with respect to Ag/AgCl for all following calculation and results. After considering the ion concentration and pH value, the equilibrium potential is -1.98 V vs. Ag/AgCl for the cathodic and -0.25V vs. Ag/AgCl for the anodic reaction, calculated using equations (1) and (2). First, the anodic and cathodic Tafel slopes are generated by fitting two straight lines tangent to the polarization curve at 100 mV higher and lower than the open circuit potential respectively (Fig. 2.5). The exchange current densities for anodic and cathodic reactions are then determined based on the procedure described in Fig. 2.1. The complete set of corrosion parameters are summarized in Table 2 for both alloys.

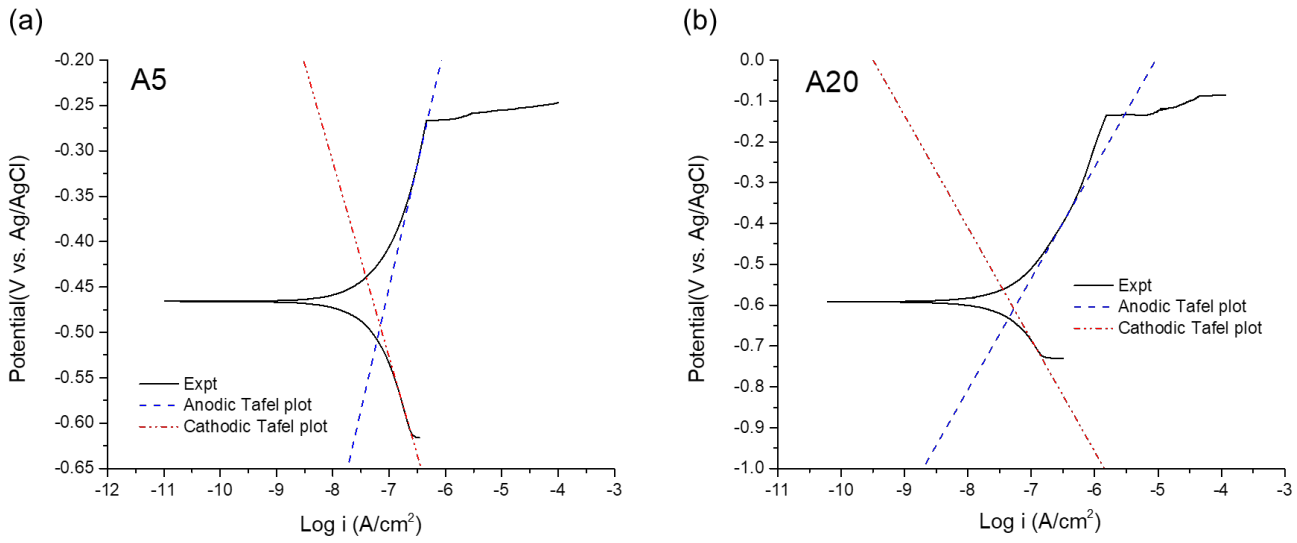

Figure 2.5 The experimentally measured potentiodynamic polarization curves and fitted Tafel plots for (a) A5 and (b) A20.

2.4 FEA simulation results and validation

2.4.1 Contact mechanics validation using analytical theory

The FEA model was first validated using analytical Hertzian contact theory [45] by simulating an elastic non-adhesive ball-on-plate contact problem. The ball was assumed to be 4 mm in diameter, with E=1144.98 GPa and ν=0.3, indenting on a plate under 10 N load. The plate material was assumed to have E=108.83 GPa and ν=0.3. Fig. 2.6 shows the FEA results of maximum shear stress distribution along the loading direction in the plate material as a function of distance from the surface. It can be seen that the simulated results are in good agreement with those calculated by Hertzian theory, validating the FEA model for an accurate representation of the contact mechanics between two bodies.

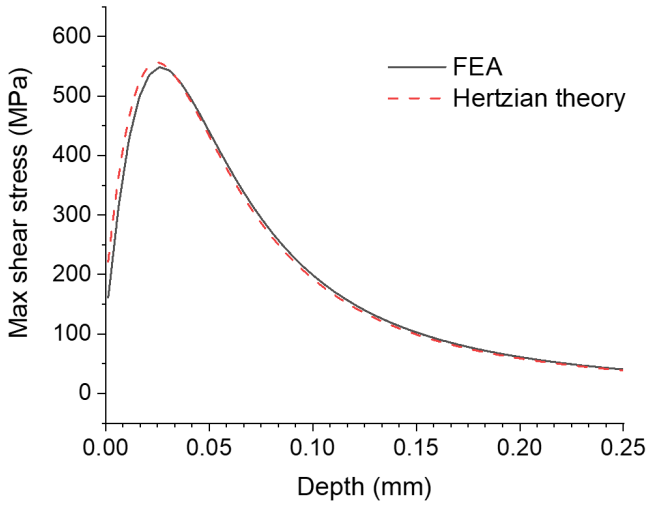

Figure 2.6 Maximum subsurface shear stress as a function of distance from the surface of a plate during ball-on-plate indentation calculated from FEM simulation (solid line) and Hertzian contact theory (dashed line).

2.4.2 FEA simulation results and experimental validation

Next, the FEA model was applied to simulate the pure wear, pure corrosion, and tribocorrosion of A5 and A20, following the procedures detailed in section 2.2, using material properties extracted from section 2.3. The 3D plot in Fig. 2.7 shows the von Mises stress and plastic strain distribution

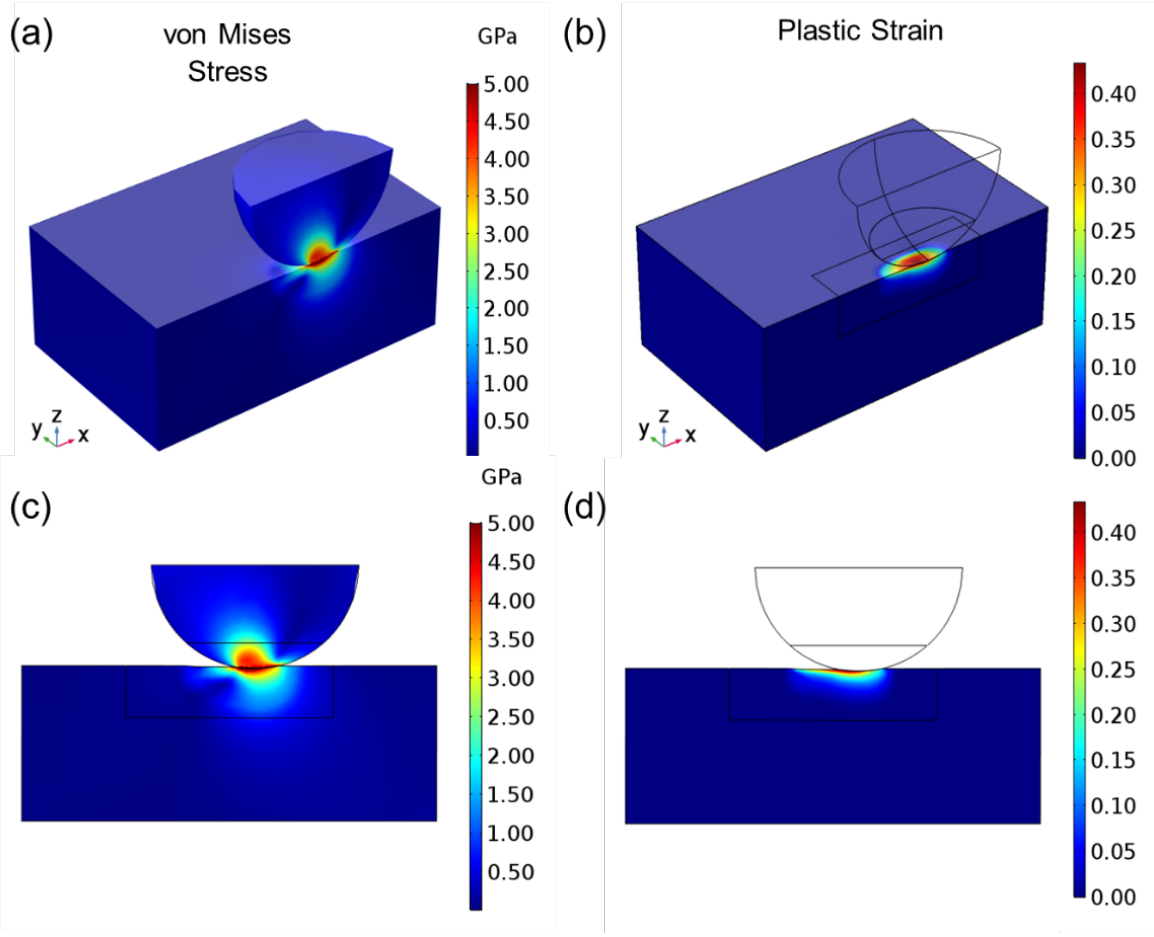

Figure 2.7 FEA simulation results of 3D (a) stress and (b) strain distribution in A5 sample under wear, and the corresponding 2D plot of (c) stress and (d) strain in x-z plane.

inside A5 sample during wear. To make a more straightforward comparison between mechanical state of A5 and A20, the y-z plane at x=0 was sliced out to demonstrate the 2D plot of stress and strain distribution, as shown in Fig. 2.8. Fig. 2.8 (a) and (e) show the von Mises stress (σvM) distribution inside the sample and indenter at the maximum load, which corresponds to the situation when the counter body slides right onto this cross-sectional area of the sample during wear. Fig. 2.8 (b, f) and (c, g) show the residual stress σvM and plastic strain distribution respectively when the indenter has passed the area (note all elastic strains were completely recovered during unloading). The wear tracks were generated by the algorithm as discussed in section 2.2.3 using the result of plastic strain are plotted in Fig. 2.8 (d, h). It could be observed that A5 suffers more severely plastic deformation than A20, with a larger plastic zone size and higher maximum strain of 25%. The friction coefficient also affects the mechanical response of the sample. In the FEA model, three values of μ (0, 0.3, and 0.6) were studied. As demonstrated in

Fig. 2.9, as μ decreases, the stress and strain decreases, especially for regions close to the surface.

For μ=0.6 and 0.3, the maximum stress and strain is concentrated at the surface. When μ decreases to 0, which resembles the case of a perfectly frictionless surface, the maximum stress and strain both shifts to below the surface, in agreement with Hertzian contact theory. For simplicity, corrosion simulations presented hereafter is carried out assuming μ=0.

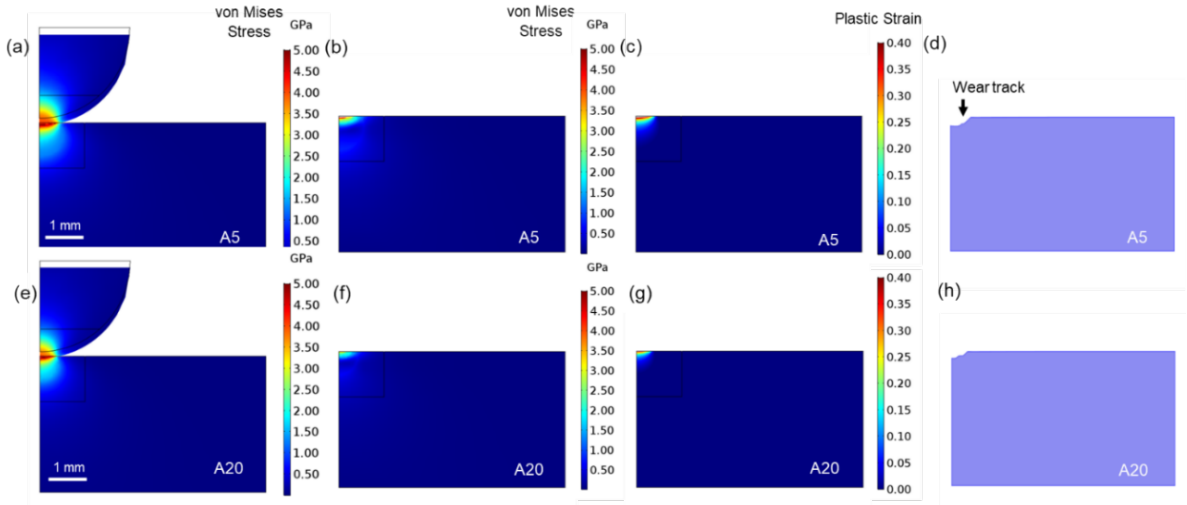

Figure 2.8 FEA simulation results of wear tests. (a, e) Subsurface stress during indenter contact, (b, f) subsurface stress, (c, g) plastic strain, and (d, h) the wear track morphology of A5 and A20 after the indenter has passed. All plots are represented from the y-z cross-section (as defined in Fig. 2.7).

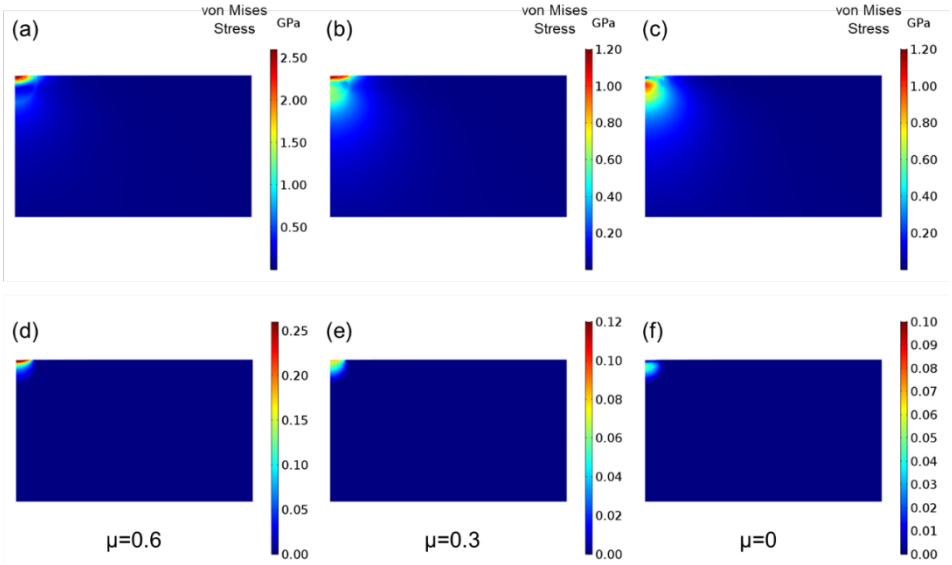

Figure 2.9 FEA simulation results of stress and plastic strain left in the A5 sample with different friction coefficient μ: (a, d) μ=0.6, (b, e) μ=0.3, (c, f) μ=0 on the y-z cross-section (as defined in Fig. 2.7).

Pure corrosion simulation results of A5 and A20 (after wear and unloading) are shown in Fig. 2.10. It is noted that the depassivation and wear-corrosion synergy effect is turned off in this step to resemble the case of pure corrosion. The deformed surface geometry, instead of flat surfaces, was used to demonstrate that the synergy effect observed later during tribocorrosion is not caused by the geometry of the wear track. The electrolyte potential (φ_{elec}) distributed uniformly in the solution, as shown in Fig. 2.10 (a) and (b). Since the open circuit potential φ_{oc} is related to the electrolyte potential as $\varphi_{oc} = -\varphi_{elec}$, the simulated φ_{oc} is -0.493 V and -0.609 V vs. Ag/AgCl for A5 and A20 respectively. These values are in good agreement with experimentally measured open circuit potential, which is -0.450 V and -0.564 V vs. Ag/AgCl for A5 and A20 respectively. During pure corrosion, material loss takes place uniformly across the surface at a constant rate over time, as shown in Fig. 2.10(c) and (d). The simulated corrosion rate is 0.83 and 0.60 µm/year for A5 and A20 respectively, in agreement with their experimentally measured corrosion current trend [32].

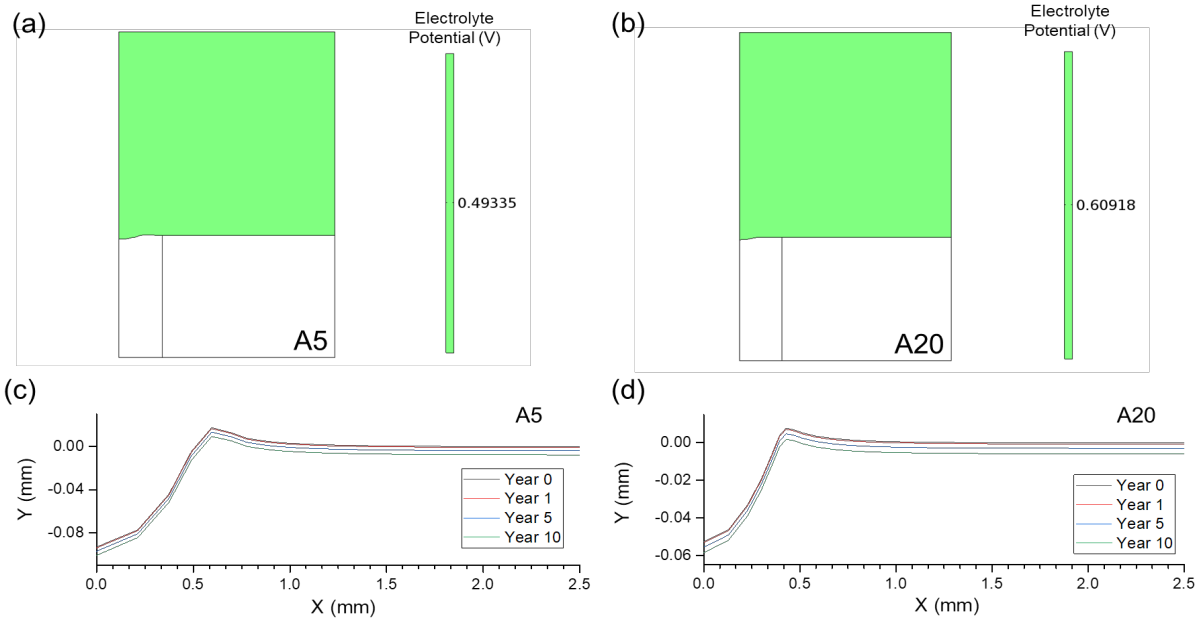

Figure 2.10 FEA simulation results of the open circuit potential for (a) A5 and (b) A20 sample, and surface profile evolution as a function of time for (c) A5 and (d) A20 after pure corrosion in 0.6 M NaCl aqueous solution.

The tribocorrosion simulation results are shown in Figs. 2.11-15, using the same testing parameters as the experiments (i.e. 0.5 N normal load, 5 mm/sec sliding speed, in 0.6 M NaCl aqueous solution [6]). The wear-corrosion synergy was included by accounting the effect of deformation on corrosion, following procedures detailed in section 2.2.4. In Fig. 2.11(a) and (b),

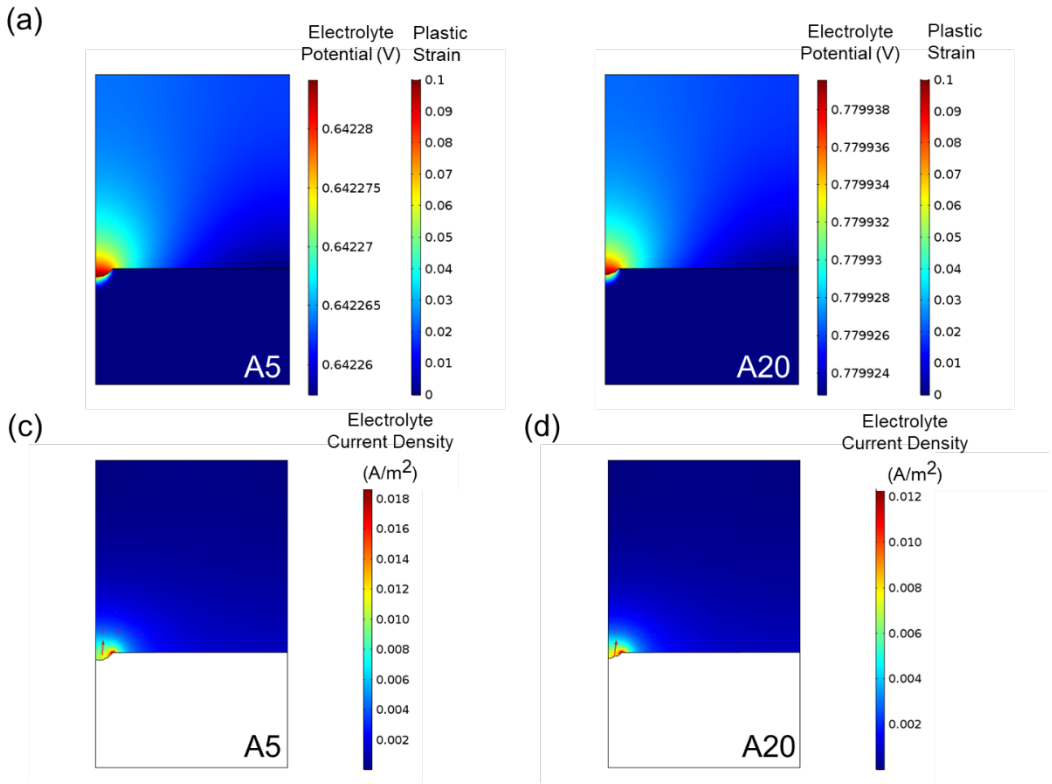

Figure 2.11 FEA simulated (a, b) electrolyte potential and subsurface plastic strain distribution, and (c, d) electrolyte current density distribution for A5 and A20 after tribocorrosion under 0.5 N load, 0.5 mm/s sliding speed in 0.6 M NaCl aqueous solution.

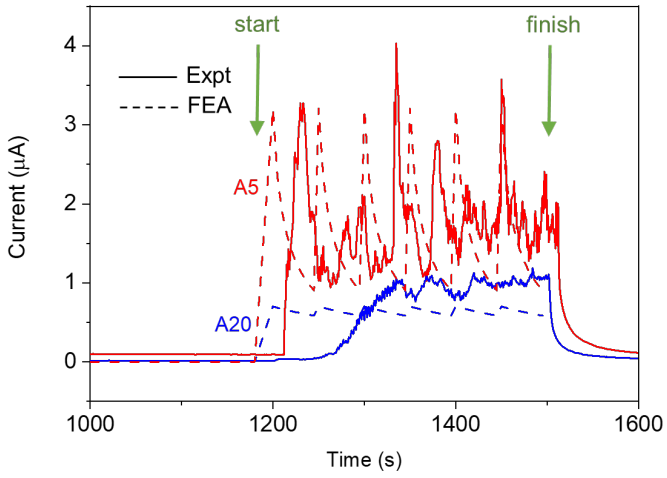

Figure 2.12 Comparison of corrosion current change during tribocorrosion of A5 and A20 between experiments (solid lines) and FEA simulation (dashed lines). Arrows indicate the start and finish time of scratching during tribocorrosion.

the resulting potential distribution inside the electrolyte is plotted along with the strain distribution to demonstrate how the mechanical state of material affects the electrochemical dynamics. It could be seen that the electrolyte potential distribution at the center, where the plastic strain is higher, shifts to a higher value than the rest area for both samples. This leads to a significant increase in electrolyte current density near the deformed area, for example, ~ 0.006 A/m2 for A5, which means faster material dissolution locally.

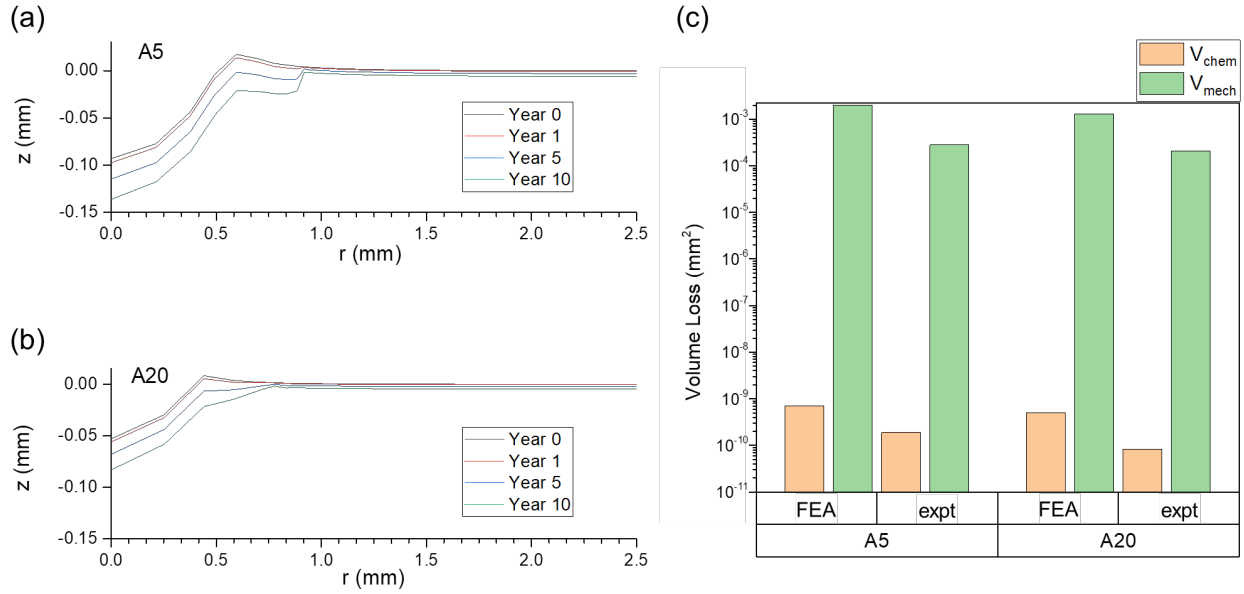

Figure 2.13 FEA simulated surface profile change during tribocorrosion for (a) A5 and (b) A20, and (c) comparison between FEA simulated and experimentally measured mechanical and chemical wear for A5 and A20.

Within the wear track, the simulated current flow during tribocorrosion is compared to those measured experimentally, as shown in Fig. 2.12. The sudden increase in current at the beginning of the scratching process due to mechanoelectrical coupling and depassivation, as well as the quasi-periodic fluctuation of corrosion current due to the cyclic depassivation/repassivation process, all agree well with experimental data. The difference in the evolution of surface profile is manifested later in the long-term simulation, as shown in Fig. 2.13 (a) and (b). Due to the wear-corrosion synergy effect, the indented area corrodes at an obviously faster rate than the rest areas. The corrosion rate drops to a deficient value at places far away from the deformed area (at $r > 0.9$ mm for A5, and at $r > 0.7$ mm for A20). The overall volume loss of both samples is also larger than the pure corrosion circumstance. To decouple the mechanical and chemical wear during

tribocorrosion, the total volume loss due to wear (V_{mech}) and corrosion (V_{corr}) is plotted separately in Fig. 2.13(c), where the volume loss of each sample is calculated using the area integration of the sample domain. It can be seen that the FEA results show the same trend between A5 and A20 as the experiments, with values of the same order of magnitude.

Interestingly, the FEA model also predicts that the mechanochemical synergy is time-dependent. By subtracting the volume loss due to pure corrosion from the volume loss of total corrosion during tribocorrosion, the volume loss caused by wear-corrosion synergy was calculated. The synergy could be further divided into two parts: residual strain induced synergy S_{strain} and depassivation induced synergy $S_{depassivation}$. The former accounts for the accelerated material loss due to the presence of subsurface strain, and the later due to the mechanical removal of the passive layer. Fig. 2.14 shows that $S_{depassivation}$ is gradually reduced with time, which is a result of repassivation in the wear track. On the other hand, S_{strain} shows little change as residual strain remains almost unchanged beneath the surface. This also indicates that the sliding frequency could affect the overall synergy. For example, high frequency wear could constantly depassivate the wear track and keep $S_{depassivation}$ at a high value. The depassivation induced synergy would sharply increase at the instance when wear takes place but only have a short-term effect after the scratching stops. In a larger timescale, S_{strain} would sustain its acceleration effect on corrosion in a long period of time even after the scratching stops. This implies that the repassivation ability has more mechanochemical coupling effect during or shortly after scratching, while the mechanical properties have a long-term coupling effect until the deformed layer is completely dissolved.

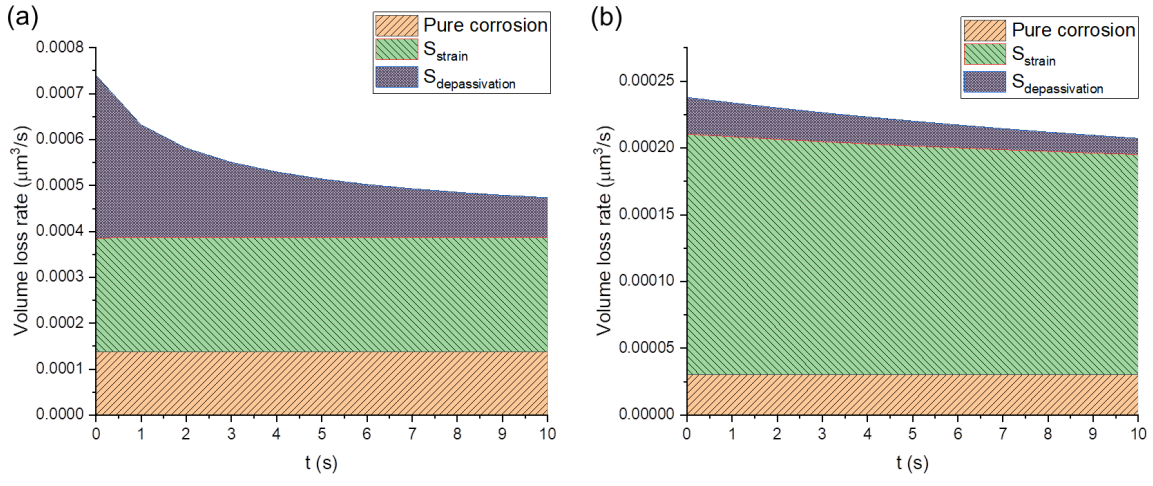

Figure 2.14 Volume loss rate from pure corrosion, strain induced synergy and depassivation induced synergy for (a) A5 and (b) A20 with respect to time.

It is worth noting that this model only takes apparent contact area in macroscale into account for simulating depassivation. Experimental investigation by Gilbert et al. has indicated that the depassivation for tribocorrosion is actually related to surface morphology at asperity scale [46]. A model developed by Ghanbarzadeh et al. successfully address the influence of surface roughness on wear-corrosion synergy [47]. The microscale surface topology was taken into account to calculate 'real contact area' for depassivation based on the boundary element method (BEM). The BEM method is a 2D evaluation depending solely on the elements on the surface plane, while the FEM model proposed in this work is a 3D model which would have much more elements and thus significantly larger amount of computation to have the same element size. It is thus unrealistic to include asperities the same way as the model by Ghanbarzadeh et al. However, the model in this work is capable of producing results of subsurface mechanical state and could be further developed to incorporate subsurface microstructures or anisotropic properties.

2.4.3 Prediction of tribocorrosion map

To further explore a generalized relationship between the material properties and wear/corrosion resistance of metals, a parameter sweep was carried out and the tribocorrosion rate (unit: mm^2), defined as the total material loss (unit: mm^3) divided by the sliding distance (unit:mm), is plotted as contour maps against these parameters, as shown in Fig. 2.15. To evaluate the effects of mechanical properties on the material loss due to mechanical deformation and chemical dissolution, the Young's modulus was swept from 55 MPa to 95 MPa with 6 MPa step size, the yield strength from 1.0 MPa to 5.0 MPa with 0.5 step size, while the corrosion parameters were taken from A5 sample and kept constant. As shown in Fig. 2.15 (a), materials with lower Young's modulus and higher yield strength are more wear-resistant, which is as expected. Interestingly, it's worth noting that even with the same corrosion properties, the corrosion rate shows a significant difference after deformation. The materials with more optimal mechanical properties would suffer less corrosion, since there will be fewer surface defects caused by plastic deformation.

Fig. 2.15 (c, d) shows the effects of corrosion parameters on the tribocorrosion behavior, where the cathodic Tafel slope was varied from -280 to -210 mV/decade, the cathodic exchange current density from 2.0×10^{-8} to 2.0×10^{-7} A/cm^2, the anode Tafel slope from 250 to 290 mV/decade, and the anodic exchange current density from 1.0×10^{-13} to 5.0×10^{-13} A/cm^2. Fig. 15 (c)

shows that the V_{corr} is insensitive to the cathodic Tafel slope but increases with increasing cathodic exchange current. Fig. 2.15 (d) shows V_{corr} increases with increasing anodic exchange current density and reducing anodic Tafel slope. Summarizing results in Fig. 2.15 indicate that materials with low anodic and cathodic exchange current density, low anodic Tafel slope, high yield strength, and low Young's modulus are highly tribocorrosion resistant, thus providing a design guideline for future metals and coatings to be used under extreme conditions.

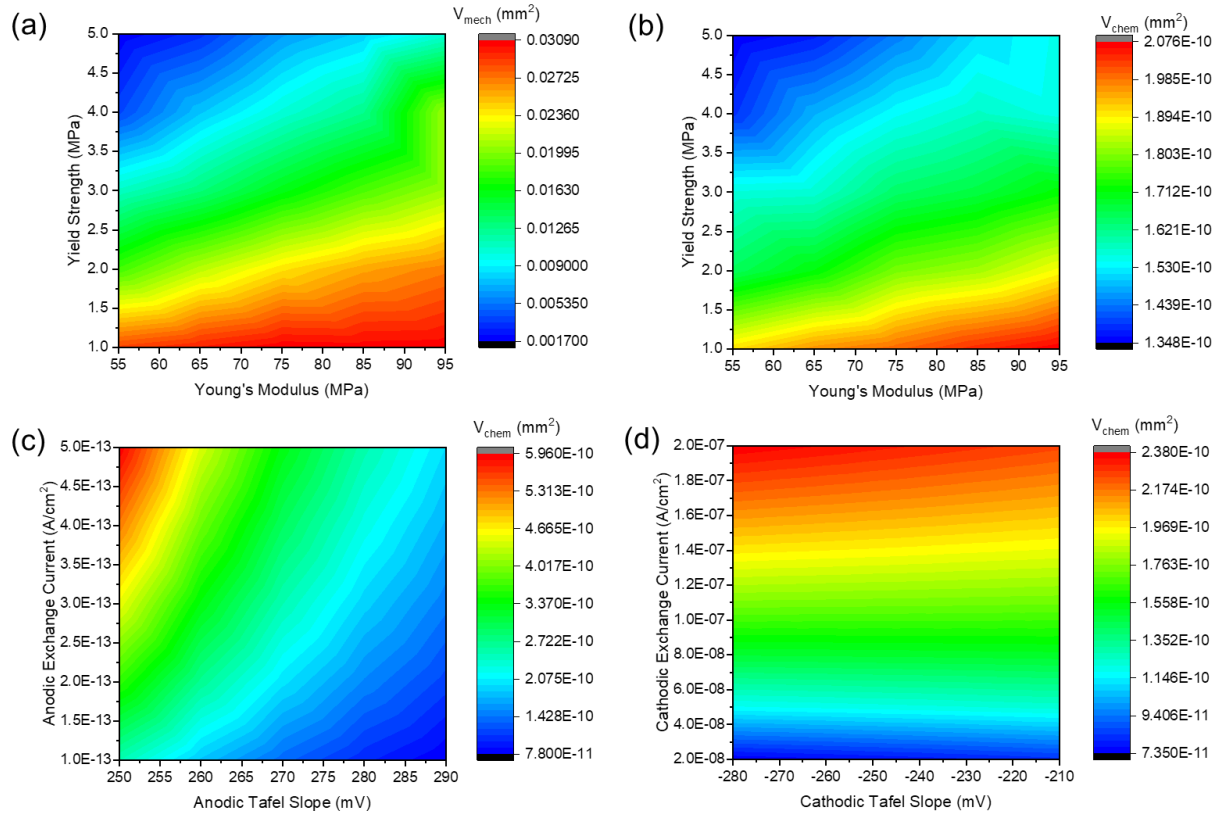

Figure 2.15 FEA predicated volume loss rate due to (a) wear and (b) corrosion for materials with different Young's modulus and yield strength, and corrosion rate for materials with different (c) anodic and (d) cathodic reaction properties.

2.5 Uncertainty quantification (UQ) study

Sections 3 and 4 introduced the detailed setup of the FEA model and simulation results given different input parameters. Apart from the specific simulation result, the confidence interval of each simulation result is especially important in the system with uncertainties in input parameters

and parametric variability. However, because of the computational cost of the FEA model, it is computationally expensive and time-consuming to apply the Monte Carlo simulations method [33] directly for uncertainty quantification. In this work, Gaussian Process (GP) [34] and Neural Network (NN) with dropout [35], two data-driven surrogates, were selected to approximate the FEA model and realize efficient uncertainty quantification [36, 37].

The simulation results from the FEA model were preprocessed and split into training and testing data. In data preprocessing, each variable, including six input variables (i.e. Young's modulus, yield strength, anodic and cathodic Tafel slopes, anodic and cathodic exchange current densities) and one output (tribocorrosion rate) variable, was normalized into $(0, 1)$ by using the max-min normalization method. Since each variable has different physical meanings and scales, normalization was necessary to reduce the possibility that the output of the data-driven model be dominated by extremely large or small values in these variables. After normalization, 89 simulations were selected as training data to build the surrogates and 17 simulations were selected as testing data to evaluate the surrogates.

In the GP model, instead of finding a deterministic function, it derives the probability distribution over all possible functions that fit the data [34]. The distribution over functions enables the GP to not only generate the predicted value but also generate a confidence interval (CI) associated with each prediction. Similarly, NN with dropout can also be regarded as a distribution over all possible functions [35], which enables the model to estimate the expectation and variance of the predictive distribution empirically. The advantages of these two surrogates include (i) they are proved to be powerful methods in modeling non-linear functions; (ii) both of them are efficient to reduce the computational cost of the original FEA simulations; (iii) as data-driven surrogates, they can learn model parameters from historical data to estimate the average and variance of output value for new samples (i.e. new FEA simulations).

After building the surrogates on the training data, the surrogates were evaluated on the testing data. Firstly, the accuracy of surrogates was evaluated. Only surrogate model with high accuracy could precisely approximate the FEA model and replace FEA in UQ analysis. Because the scale of the output is around 10^{-10}, the mean absolute percentage error (MAPE) was selected as the evaluation metric to avoid the impacts of ultra-small scale. There might be slight differences between the outputs from the surrogate model and FEA, but as long as the differences are within

a certain confidence interval (CI), i.e. 95% CI, the UQ analysis given by the surrogates are meaningful to our FEA. The results of surrogates show that the MAPE of GP is 1.1%, while the MAPE of NN with dropout is 1.5%. GP is marginally better than NN with dropout. The confidence intervals of these two models are plotted in Fig. 2.17, where the vertical axis $f(x)$ represents the output values and the horizontal axis x represents the index of observations (17 in total). These results show that most of predictions given by GP and NN were quite close to observations, which means that the surrogates are accurate enough to replace FEA in UQ analysis. Specifically, only one observation from FEA was found outside the 95% CI according to NN with dropout, while all the FEA results in section 4 were located within 95% CI according to the GP surrogate. Based on these results, several additional conclusions can be drawn: (1) UQ analysis and the corresponding confidence interval could be used to augment each simulation result given by FEA; (2) GP is more accurate than NN with dropout for UQ of tribocorrosion datasets; (3) the learned GP model can be used to approximate the UQ in FEA and calculate CI for new simulation inputs.

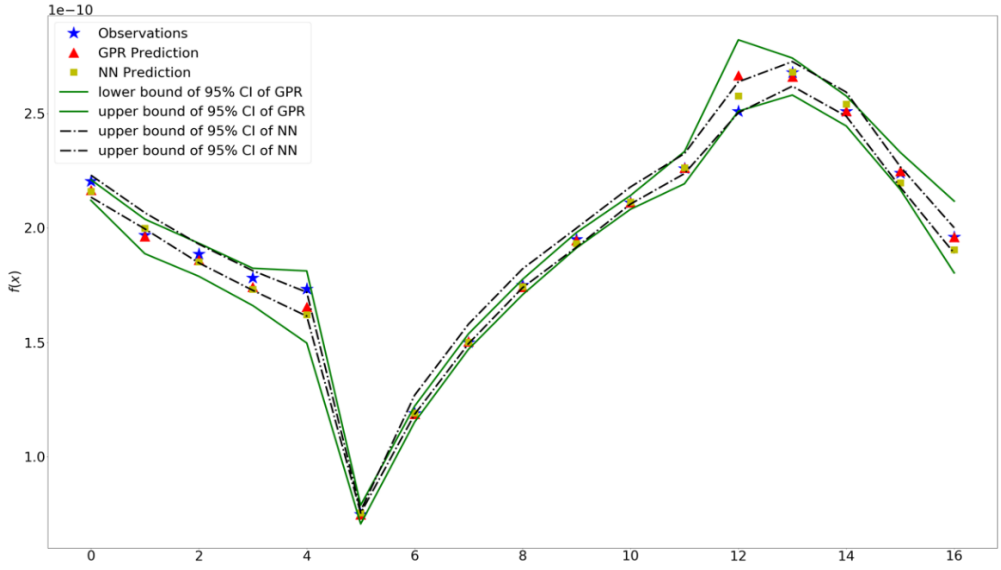

Figure 2.16 Visualization of UQ analysis where the vertical axis $f(x)$ represents the output values and the horizontal axis x represents the index of observations.

2.6 Conclusions

A multiphysics FEA model was successfully built for metal tribocorrosion and validated using experimental results of Al alloys. A procedure for material property extraction from experiments

was developed to extract Young's modulus, yield strength, exchange current density, and Tafel slopes to be used as model inputs. Using the developed FEA model, the effects of material properties on the degradation mechanism during tribocorrosion was studied. The results showed accelerated corrosion at areas near the wear track that suffered from severe deformation, as well as a time-dependent behavior of the wear-corrosion synergy due to non-uniform subsurface residual stress. The model helped not only in understanding the mechanism of tribocorrosion, but also predicted material loss under different mechanical and electrochemical properties, providing a guideline for future material design and optimization against tribocorrosion. Finally, the FEA results were successfully augmented with a confidence interval by implementing uncertainty quantification using data-driven surrogates. Gaussian Process was chosen over Neural Network due to its better correspondence with the FEA result. In this way, the FEA model not only generate specific simulation results but also the confidence interval for each simulation, which takes the uncertainties and variabilities in input parameters into consideration.

References

1. Pondicherry, K., D. Fauconnier, and P. De Baets, *Synergism in multi-asperity abrasion-corrosion of martensitic and dual phase steels in three aqueous electrolytes.* Wear, 2020. **452**.
2. Roy, S., et al., *Flow-induced failure mechanisms of copper pipe in potable water systems.* Corrosion Reviews, 2018. **36**(5): p. 449-481.
3. Kim, Y.S., et al., *Influence of a simulated deep sea condition on the cathodic protection and electric field of an underwater vehicle.* Ocean Engineering, 2018. **148**: p. 223-233.
4. Buciumeanu, M., et al., *Tribocorrosion behavior of hot pressed CoCrMo alloys in artificial saliva.* Tribology International, 2016. **97**: p. 423-430.
5. Mraied, H., W.B. Wang, and W.J. Cai, *Influence of chemical heterogeneity and microstructure on the corrosion resistance of biodegradable WE43 magnesium alloys.* Journal of Materials Chemistry B, 2019. **7**(41): p. 6399-6411.
6. Mraied, H. and W.J. Cai, *The effects of Mn concentration on the tribocorrosion resistance of Al-Mn alloys.* Wear, 2017. **380-381**: p. 191-202.

7. Vargel, C., *Corrosion of aluminium*. 1st ed. 2004, Amsterdam ; Boston: Elsevier. xxxii, 626 p.
8. Szklarska-Smialowska, Z., *Pitting corrosion of aluminum.* Corrosion Science, 1999. **41**(9): p. 1743-1767.
9. Speidel, M.O., *Stress-Corrosion Cracking of Aluminum-Alloys.* Metallurgical Transactions, 1975. **A 6**(4): p. 631-651.
10. Streinz, C.C., et al., *Analysis of Passive Film Growth by Dynamic Imaging Microellipsometry.* Journal of the Electrochemical Society, 1992. **139**(3): p. 711-715.
11. Jemmely, P., S. Mischler, and D. Landolt, *Tribocorrosion behaviour of Fe-17Cr stainless steel in acid and alkaline solutions.* Tribology International, 1999. **32**(6): p. 295-303.
12. Mischler, S., S. Debaud, and D. Landolt, *Wear-accelerated corrosion of passive metals in tribocorrosion systems.* Journal of the Electrochemical Society, 1998. **145**(3): p. 750-758.
13. Mischler, S., A. Spiegel, and D. Landolt, *The role of passive oxide films on the degradation of steel in tribocorrosion systems.* Wear, 1999. **225**: p. 1078-1087.
14. Vieira, A.C., et al., *Mechanical and electrochemical deterioration mechanisms in the tribocorrosion of Al alloys in NaCl and in NaNO3 solutions.* Corrosion Science, 2012. **54**: p. 26-35.
15. Bello, J.O., R.J.K. Wood, and J.A. Wharton, *Synergistic effects of micro-abrasion–corrosion of UNS S30403, S31603 and S32760 stainless steels.* Wear, 2007. **263**(1-6): p. 149-159.
16. Thakare, M.R., et al., *Exposure effects of strong alkaline conditions on the microscale abrasion–corrosion of D-gun sprayed WC–10Co–4Cr coating.* Tribology International, 2008. **41**(7): p. 629-639.
17. Chatterjee, A., et al., *Nanoscratch study of hard HfB2 thin films using experimental and finite element techniques.* Wear, 2010. **268**(5-6): p. 677-685.
18. Park, Y.J. and G.M. Pharr, *Nanoindentation with spherical indenters: finite element studies of deformation in the elastic-plastic transition regime.* Thin Solid Films, 2004. **447**: p. 246-250.
19. Walter, C., et al., *Finite element simulation of the effect of surface roughness on nanoindentation of thin films with spherical indenters.* Surface & Coatings Technology, 2007. **202**(4-7): p. 1103-1107.

20. Zhao, J.X., F. Sadeghi, and H.M. Nixon, *A finite element analysis of surface pocket effects in Hertzian line contact.* Journal of Tribology-Transactions of the Asme, 2000. **122**(1): p. 47-54.
21. Cross, S.R., S. Gollapudi, and C.A. Schuh, *Validated numerical modeling of galvanic corrosion of zinc and aluminum coatings.* Corrosion Science, 2014. **88**: p. 226-233.
22. Wang, Y.C., et al., *Numerical Simulation of Micro-Galvanic Corrosion in Al Alloys: Steric Hindrance Effect of Corrosion Product.* Journal of the Electrochemical Society, 2017. **164**(14): p. C1035-C1043.
23. Yin, L.T., et al., *Numerical Simulation of Micro-Galvanic Corrosion of Al Alloys: Effect of Chemical Factors.* Journal of the Electrochemical Society, 2017. **164**(13): p. C768-C778.
24. Yin, L.T., et al., *Numerical simulation of micro-galvanic corrosion of Al alloys: Effect of density of Al(OH)(3) precipitate.* Electrochimica Acta, 2019. **324**.
25. Xu, L.Y. and F. Cheng, *A finite element based model for prediction of corrosion defect growth on pipelines.* International Journal of Pressure Vessels and Piping, 2017. **153**: p. 70-79.
26. Xu, L.Y. and Y.F. Cheng, *Development of a finite element model for simulation and prediction of mechanoelectrochemical effect of pipeline corrosion.* Corrosion Science, 2013. **73**: p. 150-160.
27. Wang, H.T. and E.H. Han, *Simulation of metastable corrosion pit development under mechanical stress.* Electrochimica Acta, 2013. **90**: p. 128-134.
28. Chen, J. and W.J. Cai, *Effect of scratching frequency on the tribocorrosion resistance of Al-Mn amorphous thin films.* Wear, 2019. **426**: p. 1457-1465.
29. Ferreira, S.C., et al., *Microstructural characterization and tribocorrosion behaviour of Al/Al3Ti and Al/Al3Zr FGMs.* Wear, 2011. **270**(11-12): p. 806-814.
30. Frankel, G.S., *Pitting corrosion of metals. A review of the critical factors (vol 145, pg 2186, 1998).* Journal of the Electrochemical Society, 1998. **145**(8): p. 2970-2970.
31. Jones, D., *Principles and Prevention of Corrosion*. 1996: Prenti~e-Hall, Inc.
32. Mraied, H., W.J. Cai, and A.A. Sagues, *Corrosion resistance of Al and Al-Mn thin films.* Thin Solid Films, 2016. **615**: p. 391-401.
33. Rubinstein, R.Y. and D.P. Kroese, *Simulation and the Monte Carlo Method: Third Edition*. 2016. 1-414.

34. Crevillen-Garcia, D., et al., *Gaussian process modelling for uncertainty quantification in convectively-enhanced dissolution processes in porous media.* Advances in Water Resources, 2017. **99**: p. 1-14.
35. Gal, Y. and Z. Ghahramani. *Dropout as a bayesian approximation: Representing model uncertainty in deep learning*. in *international conference on machine learning*. 2016.
36. Wang, G.G. and S. Shan, *Review of metamodeling techniques in support of engineering design optimization.* Journal of Mechanical Design, 2007. **129**(4): p. 370-380.
37. Razavi, S., B.A. Tolson, and D.H. Burn, *Review of surrogate modeling in water resources.* Water Resources Research, 2012. **48**.
38. Oliver, W.C. and G.M. Pharr, *Measurement of hardness and elastic modulus by instrumented indentation: Advances in understanding and refinements to methodology.* Journal of Materials Research, 2004. **19**(1): p. 3-20.
39. Sakharova, N.A., et al., *Comparison between Berkovich, Vickers and conical indentation tests: A three-dimensional numerical simulation study.* International Journal of Solids and Structures, 2009. **46**(5): p. 1095-1104.
40. Nelias, D., V. Boucly, and M. Brunet, *Elastic-plastic contact between rough surfaces: Proposal for a wear or running-in model.* Journal of Tribology-Transactions of the Asme, 2006. **128**(2): p. 236-244.
41. Bosman, R. and D.J. Schipper, *Transition from mild to severe wear including running in effects.* Wear, 2011. **270**(7-8): p. 472-478.
42. Tak, Y.S. and K.R. Hebert, *Initial Events during the Passivation of Rapidly Dissolving Aluminum Surfaces.* Journal of the Electrochemical Society, 1994. **141**(6): p. 1453-1459.
43. Gutman, E.m.M., *Mechanochemistry of solid surfaces*. 1994, Singapore ; River Edge, NJ: World Scientific. ix, 322 p.
44. Hordon, M. and B.J.A.M. Averbach, *X-ray measurements of dislocation density in deformed copper and aluminum single crystals.* 1961. **9**(3): p. 237-246.
45. Fischer-Cripps, A.C., *The hertzian contact surface.* Journal of Materials Science, 1999. **34**(1): p. 129-137.
46. Smith, S.M. and J.L. Gilbert, *Compliant interfaces and fretting corrosion of modular taper junctions in total hip implants: The micromechanics of contact.* Tribology International, 2020. **151**.

47. Ghanbarzadeh, A., et al., *A New Asperity-Scale Mechanistic Model of Tribocorrosive Wear: Synergistic Effects of Mechanical Wear and Corrosion.* Journal of Tribology, 2019. **141**(2).

Chapter 3. Finite element modeling of the tribocorrosion behavior of Al/Cu nanostructured metallic multilayers

This chapter is based on the following published paper in Wear and reprinted with permission.

K. Wang and W. Cai, "Modeling the Effects of Individual Layer Thickness and Orientation on the Tribocorrosion Behavior of Al/Cu Nanostructured Metallic Multilayers", Wear, (2021), https://doi.org/10.1016/j.wear.2021.203849.

3.1 Introduction

Passive metals such aluminum and titanium alloys, and stainless steels are widely used in marine and offshore industries [1, 2], aerospace and transportation [3], and undersea vehicles and infrastructures [4] due to their high strength and corrosion resistance. However, the naturally formed passive layers on these alloys are thin and delicate, leaving the materials vulnerable to mechanical damage, which in turn, jeopardize their resistance to corrosion. This problem is especially prominent during tribocorrosion, where wear and corrosion act synergistically on the surface. Optimization of tribocorrosion resistance usually requires more than that of wear and corrosion resistance alone as numerous experiments indicate that there is typically a tradeoff between wear and corrosion resistance in engineering metals [5]. Hence the optimization of one property might exacerbate the other.

A promising solution of mitigating the wear and corrosion resistance tradeoff lies in an emerging category of materials named nanostructured metallic multilayers (NMMs), where each constituting layer has a thickness of a few to tens of nm. Past research shows that NMMs often exhibit better hardness, wear, and corrosion resistance than their monolithic counterparts [6-10]. For example, Misra et al. synthesized Cu/Nb nanolayers with excellent wear resistance, benefitted from the obstruction of dislocation propagation across the interfaces [11, 12]. On the other hand, a research by Fei and Wilcox shows Zn/Ni NMMs exhibit better corrosion resistance than pure Zn

and Ni metal due to refined microstructure, decreased surface roughness, and the formation of a more compact and protective oxide film [13]. Although limited research has been conducted on the tribocorrosion resistance of NMMs, these separate wear and corrosion studies indicate great potentials of achieving high tribocorrosion resistance in NMMs.

The individual layer thickness is a key parameter that affects both wear and corrosion resistance of the metallic multilayers. In a research investigating mechanical properties of sputter-deposited Cu–Nb multilayers, Misra et al. [14] report their observation of the strength dependence on layer thickness: the hardness increases as the layer thickness decreases until reaching a maximum at 2 nm; further decreasing the layer thickness leads to a slight drop in hardness. They exploited three different mechanisms including Hall-Petch scaling law, confined layer slip model, and atomistic dislocation transmission, to explain this phenomenon This thickness effect is also observed in Ag/Fe and Ag/Ni multilayer systems by Li et al. [15]. They found that as the layer thickness decreased from a few hundreds to tens of nanometers, both the hardness and wear resistance of the material were improved. As for the corrosion behavior, Flores et al. [16] observed that even though reducing the thickness of layers increased the tendency to corrode during the corrosion initialization process, the overall corrosion resistance in long term was improved.

Following these experimental attempts, computational efforts were also made to help better understand the mechanism lays underneath the behavior of metallic multilayers. Finite element analysis (FEA) is a powerful tool in modelling phenomenon caused by this layered structure and capture the state of deformation and degradation within the material. Zhao et al. [17] used FEA to simulate the mechanical response of the TiSiN-based multilayer coating during a nanoindentation test. They explained the formation of the ring, lateral and radial cracks at layer interfaces by analyzing the stress distribution in the multilayer. Mayer et al. [18] investigated the effects of layer orientation and layer waviness on the mechanical behavior of Al-SiC nanolaminate with FEA and further predicted that wavy layers could produce more compliant behavior than flat layers. However, little research has been done so far on simulating tribocorrosion process of metallic multilayers.

This research aims to investigate the effects of layer thickness and orientation on the tribocorrosion behavior of NMMs in 0.6 M NaCl aqueous solution through FEA modeling, using aluminum copper multilayers (Al/Cu) as an example. Al is chosen as it is a widely used passive

metal due to its light weight and excellent corrosion resistance. Cu is chosen as a more wear resistant non-passive metal with the same face-centered-cubic (fcc) crystal structure as Al. The outmost layer is assigned to be Al due to its passivity in neutral seawater while the underneath Cu layers provide mechanical support to the structure to maintain its integrity. The model was built to simulate the stress and strain distribution due to wear, the potential and current distribution during corrosion, and predict the time-dependent surface evolution and material removal rate during tribocorrosion. This model provides a numerical framework to probe the mechanical and electrochemical state of NMMs which is hard to obtain through experiments. It also makes the prediction of tribocorrosion induced material degradation of NMMs with different microstructure with great efficiency. The model was verified in terms of mechanical response by Hertzian theory-predicted stress distribution. Finally, the effects of different layer thickness and orientation on the tribocorrosion mechanisms of NMMs were discussed based on these simulation results. These simulation results confirm the recent experimental findings on the superior tribocorrosion resistance of Al/Cu multilayers [19]. The simulation study provided further insights to the underlying mechanism of the improvement in tribocorrosion resistance.

3.2 Theoretical Background and Model Setup

In this research, a tribocorrosion scenario was investigated where a ball-shaped alumina tip performs a single scratch on the sample surface immersed in 0.6 M NaCl aqueous solution, as shown in **Fig. 3.1**. A commercial finite element software COMSOL 5.3 was used and the element removal algorithm was realized with COMSOL Livelink for Matlab. The model involves the solution of a two-body contact problem between the tip and the sample, which causes abrasive wear, and an electrochemical problem of galvanic corrosion between layers of different metals. An axisymmetric 2D geometry setup was employed for computational efficiency. Previous researches have verified with experiments that the stress distribution profile captured by the axisymmetric contact model is sufficient to predict wear volume loss [20-22]. For simplicity, in this model, the total material loss was modeled as a two-step process, where wear proceeded first as a transient state, followed by corrosion of the worn surface.

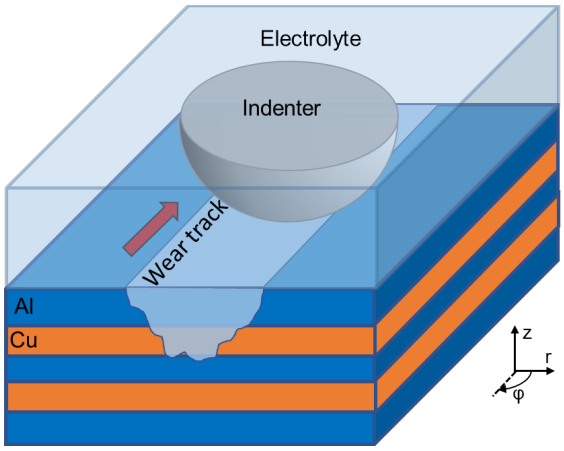

Figure 3.1 Schematic of tribocorrosion testing of metallic multilayers used for the FEA model.

3.2.1 Abrasive Wear

The geometry of the axisymmetric wear model is shown in **Fig. 3.2 (a)**. The sample is a 200×200 nm square and the counter body is assumed to be a spherical tip with a radius of 0.5 microns. The top layer is Al, followed by Cu. The load was exerted on the top boundary of the indenter while the bottom boundary of the sample was fixed. The sample was meshed in square-shaped elements with an element size of 1 nm while the region near the tip of the indenter is set to be a triangular mesh of 0.5 nm element size, as shown in **Fig. 3.2 (b)**. The out-of-plane scratch length is 5 mm and the sliding velocity of the indenter is 0.2 mm/s.

The layers were set as linearly-elastic and perfectly-plastic materials, with elastic modulus, Poisson's ratio and yield strength of Al and Cu summarized in Table 3.1 [23, 24]. The plasticity is implemented using the von Mises yield criteria [25, 26], which could be generally expressed as

$$F = \sqrt{3J_2} - \sigma_y = 0, \tag{3.1}$$

where the first term is the von Mises stress, in which $J_2 = \frac{1}{6}((\sigma_{11} - \sigma_{22})^2 + (\sigma_{22} - \sigma_{33})^2 + (\sigma_{33} - \sigma_{11})^2) + \sigma_{12}^2 + \sigma_{23}^2 + \sigma_{13}^2$, and the second term is the yield strength (σ_y). σ_{11}, σ_{22}, σ_{33}, σ_{12}, σ_{13} and σ_{23} are components of stress tensor, where 1, 2, 3 corresponds to x, y, z direction in Cartesian coordinates. In the axisymmetric cylindrical coordinates, the equation could be expressed as $J_2 = \frac{1}{6}((\sigma_r - \sigma_z)^2 + {\sigma_r}^2 + {\sigma_z}^2) + {\sigma_{rz}}^2$, where σ_r and σ_z are normal stress in the r and z direction (as defined in Fig. 1), and σ_{rz} is the shear stress. The strain generated beyond this

limit is the effective plastic strain ε_{pl}, which is irrecoverable after the load is removed. The indenter tip was set as a linearly-elastic material with the mechanical property of alumina. The detailed parameters are obtained from COMSOL's built-in database [27] and are also listed in **Table 3.1**.

Table 3.1 Summary of mechanical parameters of Al and Cu used in the FEA model. E and σ_y represent the Young's modulus and yield strength respectively.

Material	E (GPa)	σ_y (GPa)	ν	Reference
Al	77.62	0.223	0.33	[23]
Cu	117.23	0.330	0.34	[24]
Al_2O_3	300.00	N/A	0.222	[27]

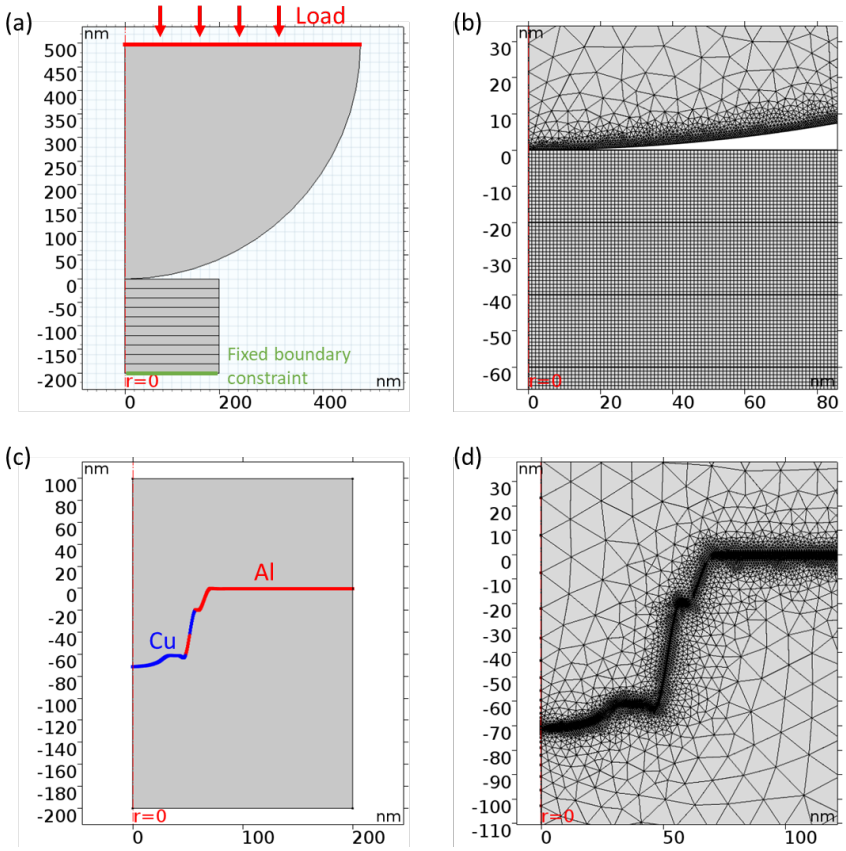

Figure 3.2 FEA model of the (a, b) mechanical contact and (c, d) corrosion process geometry setup and meshing.

In abrasive wear, materials not only go through plastic deformation referred to as ploughing, which could be calculated using the eqn. (3.1) above, but would also suffer from cutting which accounts for material removal when small debris of material experience highly plastic deformation and detach from the bulk. A wear model with running-in effect based on FEA result and validated by experiments [28] was adopted to simulate the material removal. This algorithm is based on a research by Nélias et al., [29] which claims that material removal would occur when plastic strain exceeds a threshold value and material debris is detached from the surface. This threshold value is affected by many tribological factors including coefficient of friction, surface adhesive force, sliding velocity, and wear cycles, etc. Despite its complexity, this critical plastic strain ε_c could be calibrated using a few rounds of experiments. The acquirement of the precise value of this ε_c is not the main focus of this work, so a sweep through a few representative values of ε_c (from 0 to 0.02) in the wear model was done to demonstrate the model can account for different severity of wear.

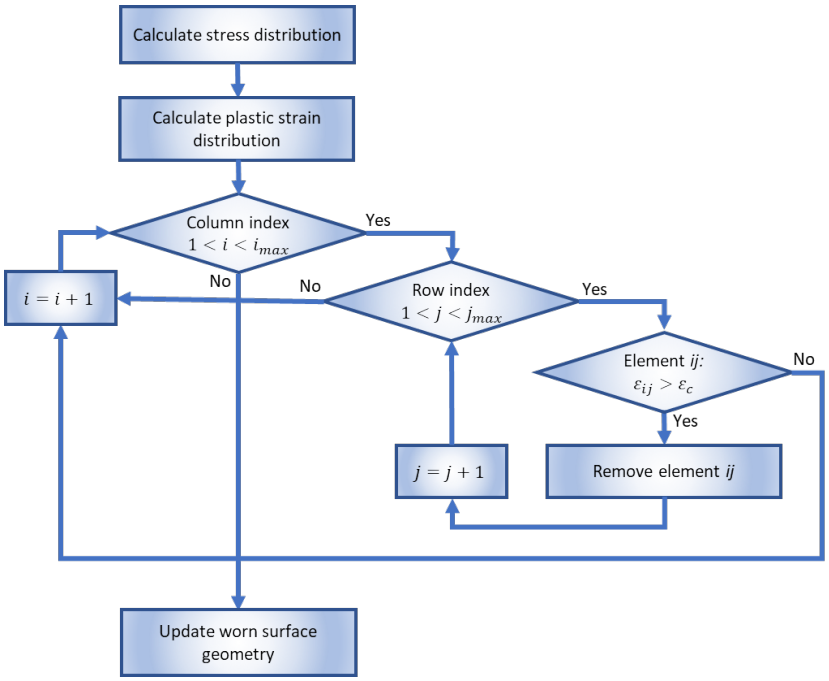

Figure 3.3 Flowchart of the algorithm for material removal in the FEA model.

The general algorithm of the wear process is demonstrated in **Fig. 3.3**. In this model, first, the FEA simulation was run to calculate the stress and strain distribution of the multilayers. For a given point on the sample surface, starting from the element closest to the surface along the -z

direction, ε_{pl} of each element was evaluated. If the obtained ε_{pl} is larger than ε_c, the element is considered as a worn element and removed. The same process was then repeated on the element beneath it until an element with $\varepsilon_{pl} < \varepsilon_c$ was found (unworn element). The element removal operation at this location could then be terminated and the loop proceeds to the next location on the sample surface. The final worn surface is obtained after all surface locations are evaluated using this method.

3.2.2 Aqueous Corrosion

After the wear process is simulated, a corrosive environment is added to the model. Because the electrical conductivity of Al and Cu are both very high, the potential inside the sample will reach an equilibrium of uniform distribution instantly. Thus, the whole sample could be treated as a bulk electrode instead of a layered geometry to avoid convergence issue that could occur in surface evolution when the zigzagged surface intersects with the layer interface. The difference in the corrosion reactions of different layers is achieved by dividing the surface into different sections according to their Z coordinates and assigning the respective reactions, as demonstrated in **Fig. 3.2 (c)**.

The reaction kinetics at the surface is assumed to follow the Butler-Volmer equation as

$$i_{loc} = i_0 \left(\exp\left(\frac{\alpha_a F \eta}{RT}\right) - \exp\left(\frac{-\alpha_c F \eta}{RT}\right) \right), \tag{3.2}$$

where i_{loc} is the local current density at the electrode surface, i_0 is the exchange current density, α_a and α_c is the transfer coefficient for anodic and cathodic reaction respectively. F, R, T stands for Faraday constant (96485 C/mol), ideal gas constant (R=8.3145J/(mol·K)) and absolute temperature respectively. The overpotential η is defined as $\eta = -\phi_l - E_{corr}$, in which ϕ_l is the electrolyte potential at the sample surface and E_{corr} is the corrosion potential of the metal. E_{corr}, i_0, α_a and α_c are unique electrochemical parameters characterizing the dissolution reaction of Al and Cu and are obtained from Tafel extrapolation of experimentally measured potentiodynamic curve and are listed in **Table 3.2** [19, 30]. All potentials are converted to the values with respect to an Ag/AgCl reference for all inputs and calculations.

Table 3.2 Summary of electrochemical parameters of Al and Cu used in the FEA model. E_{eq} and i_0 are the equilibrium potential and corrosion current density respectively, and α_a and α_c are the transfer coefficient for the anodic and cathodic reaction respectively.

Material	E_{corr} (V vs. Ag/AgCl)	i_0 (A/m^2)	α_a (V/decade)	α_c (V/decade)	Reference
Al	- 0.73	0.0083	0.23	0.23	[30]
Cu	- 0.21	0.012	0.21	0.14	[19]

Inside the electrolyte, the current density ($\boldsymbol{i_l}$) and the electrolyte potential (ϕ_l) satisfy the differential equations of:

$$\begin{cases} \nabla \cdot \boldsymbol{i_l} = Q \\ \boldsymbol{i_l} = -\sigma_l \nabla \phi_l \end{cases}, \tag{3.3}$$

where Q stands for the charge sources, which is 0 in the electrolyte in our case, and σ_l is the conductivity of the electrolyte, which is set as 5 S/m as generally measured for sea water.

At the electrolyte/electrode interface, the current density satisfies the boundary condition of $\mathbf{n} \cdot \boldsymbol{i_l} = i_{loc}$ for continuum. The time-dependent electrochemical state of the system was evaluated by solving these differential equations. The material dissolution rate normal to the surface is calculated by taking the current density from above into the Faraday's law:

$$v_n = \frac{i_{loc} M}{nF\rho}, \tag{3.4}$$

where M is the molar mass, n is the number of electrons transferred in dissolving 1 metal atom, F is the Faraday's constant (96485 C/mol), and ρ is the density of the metal. For the corrosion of Al, the number of electrons transferred is 3. Cu dissolves into a monovalent Cu^+ ion and 1 electron is transferred. The molar mass and density of Al and Cu are listed in **Table 3.3**.

Table 3.3 Summary of material parameters of Al and Cu used in Faraday's law.

Table Material	Electron transferred	Molar Mass (g/mol)	ρ (g/cm^3)
Al	3	26.98	2.70
Cu	1	63.55	8.96

Apart from active dissolution, repassivation also occurs on the aluminum surface, during which a layer of thin but dense oxide (mainly Al_2O_3) layer is formed and acts as a barrier to protect the bulk Al. Established theoretical explanation commonly treats this passive layer as a combination of resistance and capacitance in parallel, which is justified by electrochemical impedance spectroscopy measurements [31]. In this model, the passive layer is treated as an electrical resistant film whose resistance increases as the film grows thicker. The simulation of the repassivation process was realized using a film resistance option for the electrode surface in COMSOL. Suppose the loss of Al at a location is d in thickness, the accumulated passive layer thickness is $1.29d$ calculated from their molar volume ratio (i.e. M_{Al2O3}/M_{Al}). Along with the dissolution of the Al, the model generates a resistant barrier with local conductivity per unit area of $1.29\sigma d$, where σ is the conductivity of Al_2O_3, which equals to $1 \times 10^{-12} S/m$. For the Al surface outside wear track where the passive layer is intact, a constant film thickness of 4 nm is set, consistent with existing experimental observations [32]. This will significantly reduce the current exchanges between the electrode and electrolyte, simulating the passivation effect. Previous experimental results point out that repassivation of Al typically takes around 1~2 min to complete after tribocorrosion [23, 33], so the simulation time for corrosion is controlled to be a total of 120 s with a 10 s timestep. There have been evidences that the corroded Cu in NaCl solutions forms CuCl which is non-adhesive and dissolvable [1, 34]. Thus, Cu is treated as active corroding metal with no protective layer. The depassivation/repassivation effects and the galvanic coupling between the exposed inner layers accounts for the synergy between wear and corrosion. Even though some simulation work also involves the change of E_{corr} due to plastic strain to account for synergistic effect [35, 36], such method is not applied in this work since it is not compatible with the wear model with the strain-based criterion introduced above. Such effect is considered minor as compared to the synergy caused by depassivation/repassivation and galvanic corrosion. The meshing near the wear track is plotted in **Fig. 3.2 (d)**. The meshing is set to a finer element size of 1 nm along the sample surface where galvanic coupling between layers is more concentrated and potential gradient is large, while the rest of the model were meshed with coarser elements ranging up to 20 nm. Triangle mesh is used to better accommodate the rugged shape of the surface.

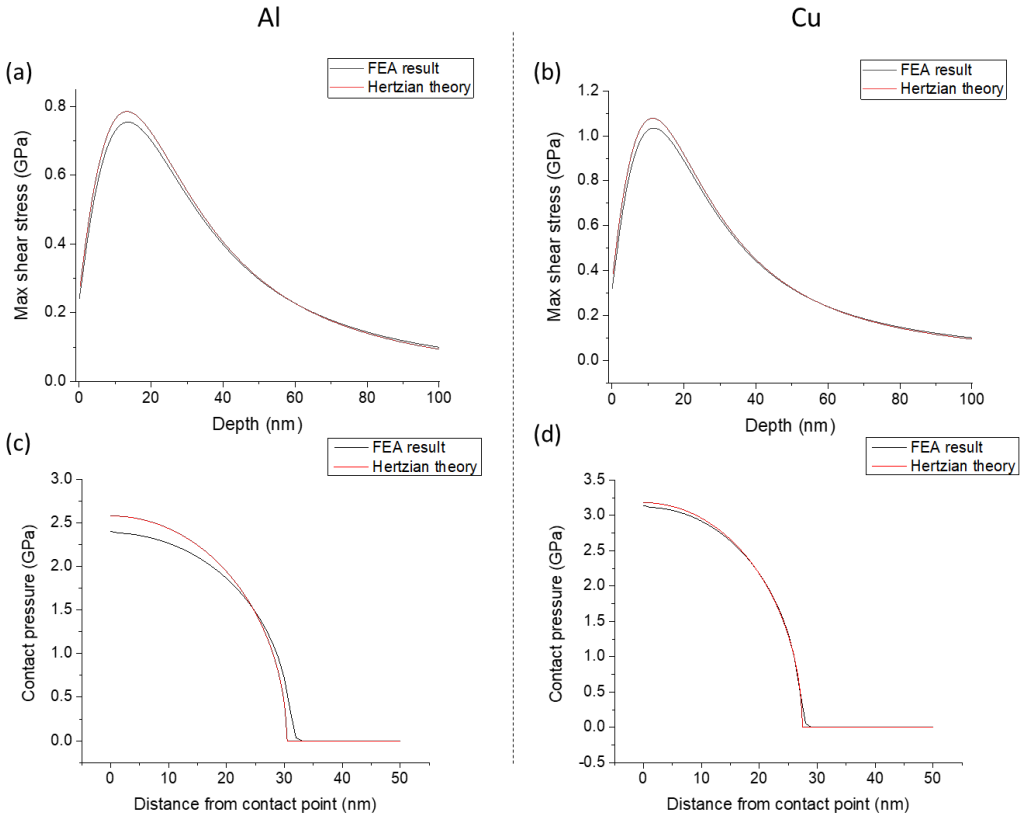

Figure 3.4 Comparison between FEA simulation and Hertzian contact theory results: (a, b) maximum shear stress as a function of depth along the loading axis, and (c, d) surface contact pressure as a function of distance from the loading point of Al and Cu.

3.3 Simulation results

3.3.1 Subsurface deformation and wear

The contact problem of pure bulk materials without considering the plasticity could be verified with analytical solution of Hertzian contact pressure and shear stress. The contact problem of the indenter with monolithic Al and Cu under 5 μN load is studied using both analytical Hertzian contact theory and FEA simulation. As shown in **Fig. 3.4**, the result of contact pressure against the distance to the contact point along r axis and maximum shear stress against the depth from the surface along z axis obtained by FEA model is in good agreement with that from the calculation by Hertzian theory, proving the feasibility of using FE model to study wear.

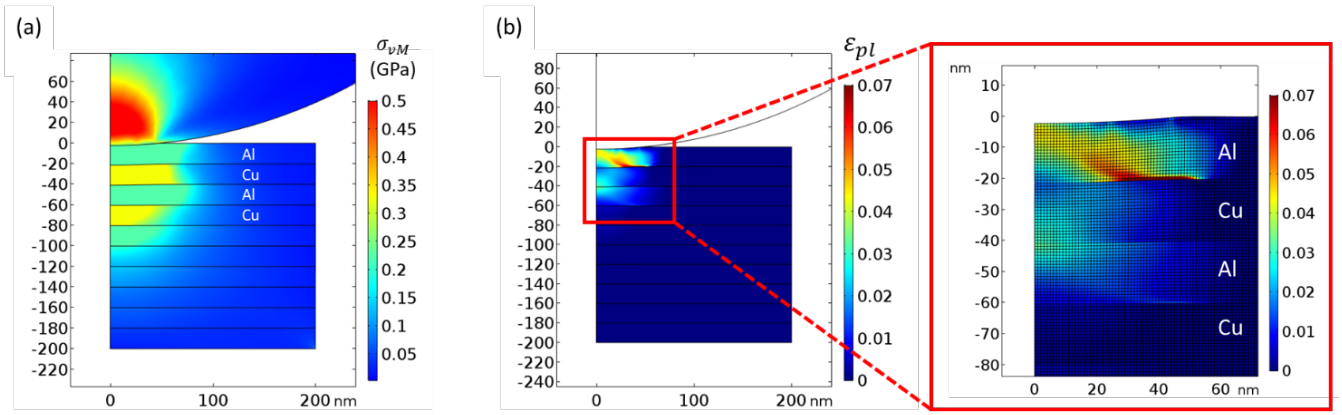

Figure 3.5 FEA model predicted (a) von Mises stress and (b) effective plastic strain distribution of Al/Cu NMM under 5 μN load.

Al/Cu NMMs with an individual layer thickness (h) of 20 nm was chosen to explore the wear mechanism of multilayers. The sample underwent a wear test with an applied normal load of 5 μN from the spherical surface on the top of the tip. **Fig. 3.5 (a) and (b)** shows the effective stress and strain distributions across different layers inside the sample respectively when the tip indents the sample. A magnified plot of the contact zone is shown in **Fig. 3.5 (b)**, which demonstrates the maximum strain occurs within the top Al layer, near the Al/Cu interface. It could be inferred from these results that the Al layers suffers more plastic deformation than their adjacent Cu layers, while the Cu layers carry more load than the softer Al layers. These observations are consistent with those measured experimentally, where layer compression was found to be more significant in the softer layers of Al/Ti and Cu/Ag NMMs [37, 38]. The effects of critical strain on the worn surface profile were studied by varying the ε_c values from 0, 0.001, 0.002 and 0.02, which rendered a set of surfaces with different wear severity, as shown in Fig. 6. It can be seen that as the critical strain increases, the overall material loss is reduced. The worn surface depth is generally higher near the loading point (r=0) and decreases rapidly approaching the edge of the contact area. This overall morphology of worn surface is indeed in good agreement with those observed experimentally on NMMs after indentation and wear tests [39, 40]. Due to limited length of the article, for the rest of this work, the case of $\varepsilon_c = 0.002$ was chosen for all tribocorrosion simulations for consistent investigation and discussion.

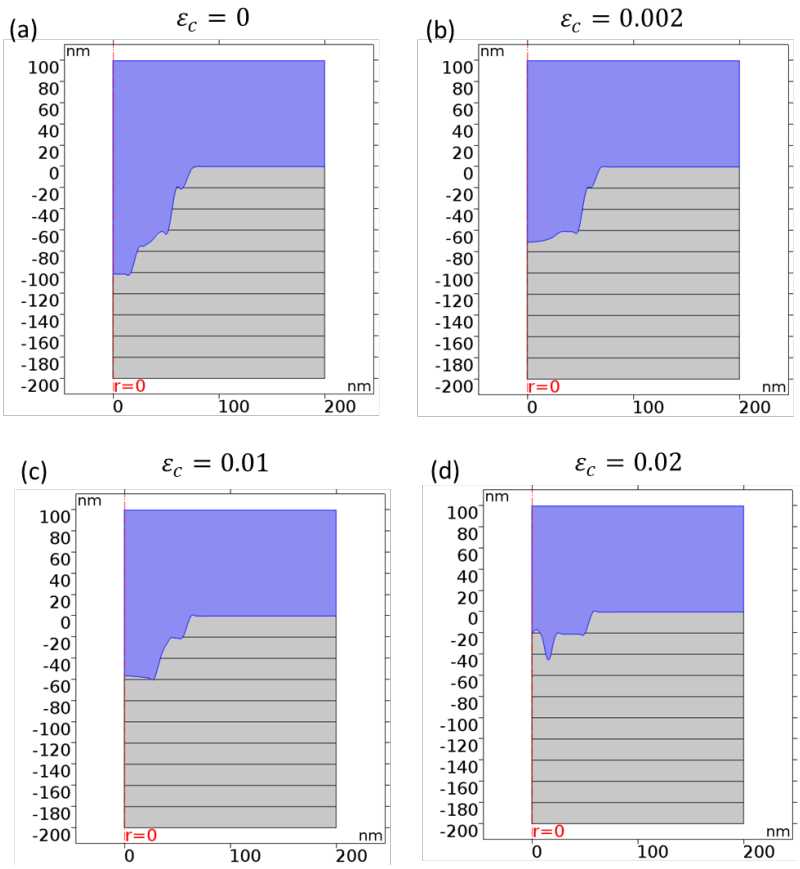

Figure 3.6 FEA model predicted worn surface of Al/Cu NMM (h=20 nm) as a function of critical strain ε_c with value of (a) $\varepsilon_c = 0$, (b) $\varepsilon_c = 0.002$, (c) $\varepsilon_c = 0.01$, and (d) $\varepsilon_c = 0.02$. The blue region denotes the electrolyte.

3.3.2 Corrosion of the worn surface

Using the worn sample surface generated under 5 μN load, the electrolyte potential and current density distribution during the corrosion of the worn surface was simulated. As shown in **Fig. 3.7**, the Al layers, which has lower corrosion potential than Cu, serve as the sacrificial anode locally and protect the exposed Cu surface from corroding. The corrosion current mainly flows from Cu into Al layers. This is similar to the experimental observations in seawater corroded Al-Cu alloys that Cu was preserved on the corroded surface while Al suffers from accelerated corrosion [41]. It is interesting to note that due to the micro-galvanic coupling, the corrosion current near the Al/Cu interfaces is often higher than that far away. In the present case, the highest corrosion current occurs near the interface between the first Al/Cu interface due to the higher surface protrusion from wear.

The time-dependent evolution of the surface is demonstrated in **Fig. 3.7 (c)**, which shows that a higher corrosion rate occurs within the Al than the Cu layers. In addition, the overall material loss is higher within the wear track than far away. It should also be noted that the material loss rate is not a constant over time due to repassivation of the Al layers. As shown in **Fig. 3.7 (d)**, the material loss rate decreases with time, as a result of passive layer's continued growth, making it more effective in limiting the corrosion current flowing through the interface as the (repassivation) time increases.

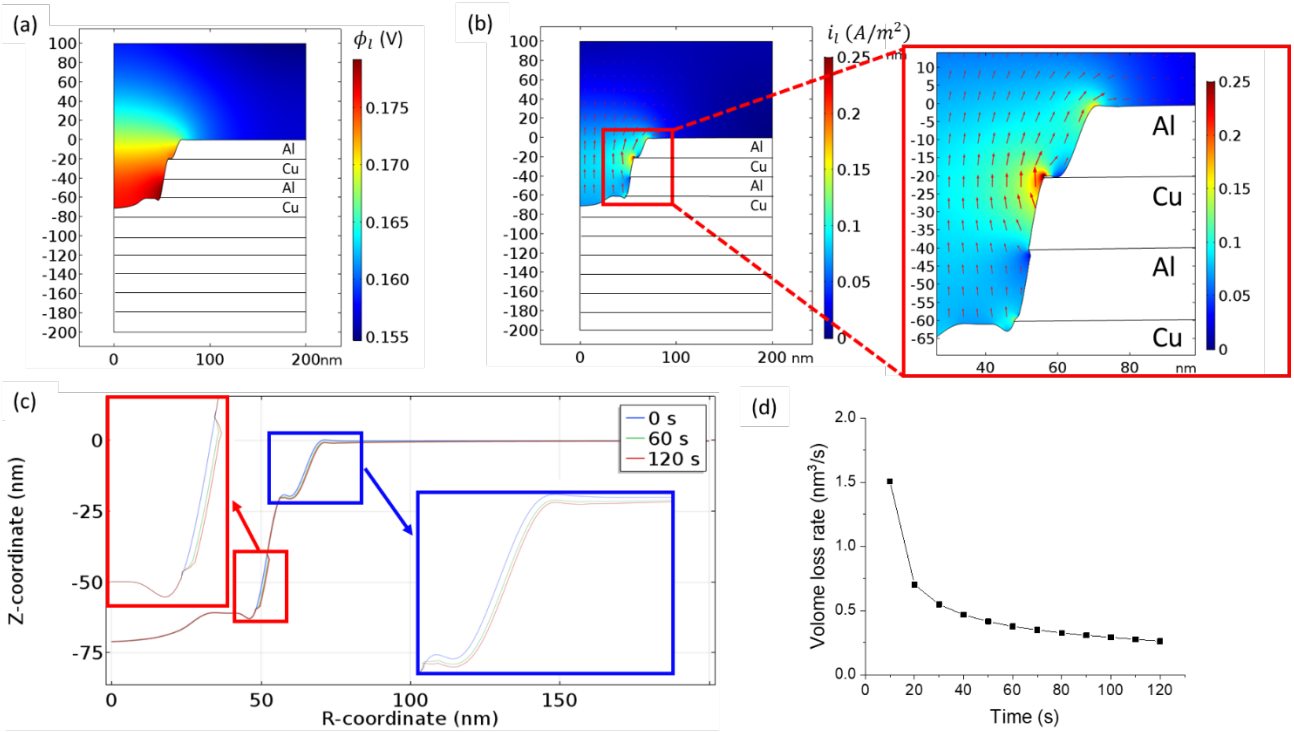

Figure 3.7 FEA model predicted (a) electrolyte potential, (b) current density distribution, (c) surface evolution, and (d) total material volume loss due to tribocorrosion as a function of time of Al/Cu NMM (20 nm individual layer thickness) after tribocorrosion process under 5 μN load.

3.3.3 Effects of applied load

Fig. 3.8 shows the mechanical response and worn surface of Al/Cu NMM (h=20 nm) under different load. As the applied load increases, the contact area and depth of the NMM increases, so are the wear track width and depth. In all cases, the maximum strain occurs within the top Al layer, near the Al/Cu interface. A summary of material loss by wear and corrosion normalized by sliding distance under different load is plotted in **Fig. 3.9 (a)**. The 2D model simulates the cross-section

of the sample and the results for material loss (denoted by w) in all the following graphs are normalized by the sliding distance (l) of the indenter. It is worth noting that even though higher load leads to significantly larger wear track, causing more surface exposure to the corrosive environment, this does not necessarily lead to a significant increase in corrosion rate (**Fig. 3.9(a)**).

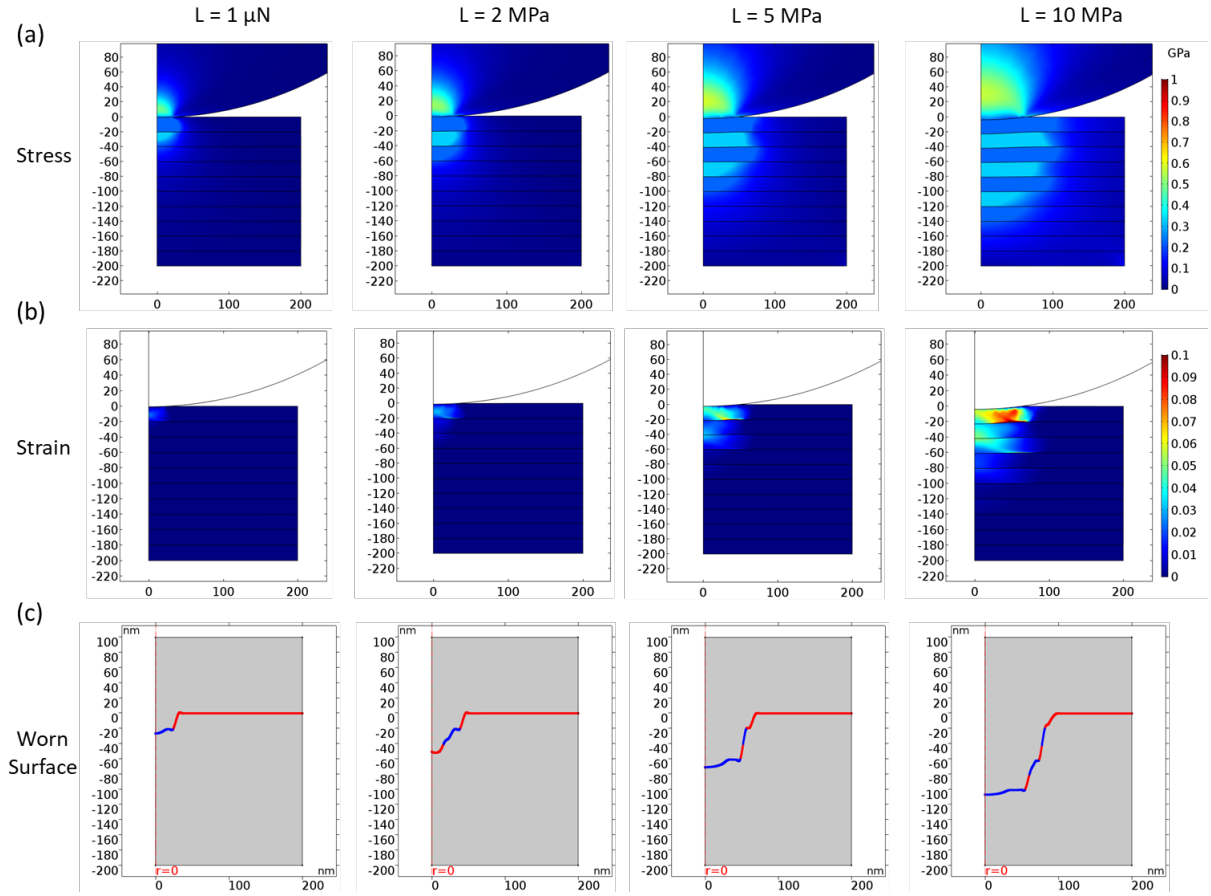

Figure 3.8 FEA model predicted (a) stress, (b) strain distribution, and (c) worn surface profile of Al/Cu NMM (20 nm individual layer thickness) under different load L (1- 10 μN). The red line denotes the Al layers and the blue line denotes the Cu layers.

This is mainly because even though the total wear track is broader under higher loads, a large portion of the newly exposed surface is Cu, which almost does not corrode in this process. Here, a wear-corrosion synergy term is defined by the difference between the total corroded volume of the worn surface and that from pure corrosion of the (unworn) NMM, both normalized by the sliding distance. In **Fig. 3.9 (b)**, the material loss under the same corrosive environment is shown, where the orange and green bar is the material loss rate (volume/sliding distance) caused by pure corrosion and wear-corrosion synergy. The red, blue, green dashed lines represent the theoretical material loss of passive Al, active corroding Al with repassivation effect, and pure Cu respectively

under pure corrosive environment. It can be seen that the total tribocorrosion rate of the Al/Cu NMMs falls in between the pure corrosion rate of passive Al and active Al, and significantly lower than that of Cu. This shows that wear-corrosion synergy accelerates corrosion rate and plays an import part in material degradation during tribocorrosion. It also manifests the design of Al/Cu multilayer structure has indeed achieved better tribocorrosion resistance than pure Al and Cu.

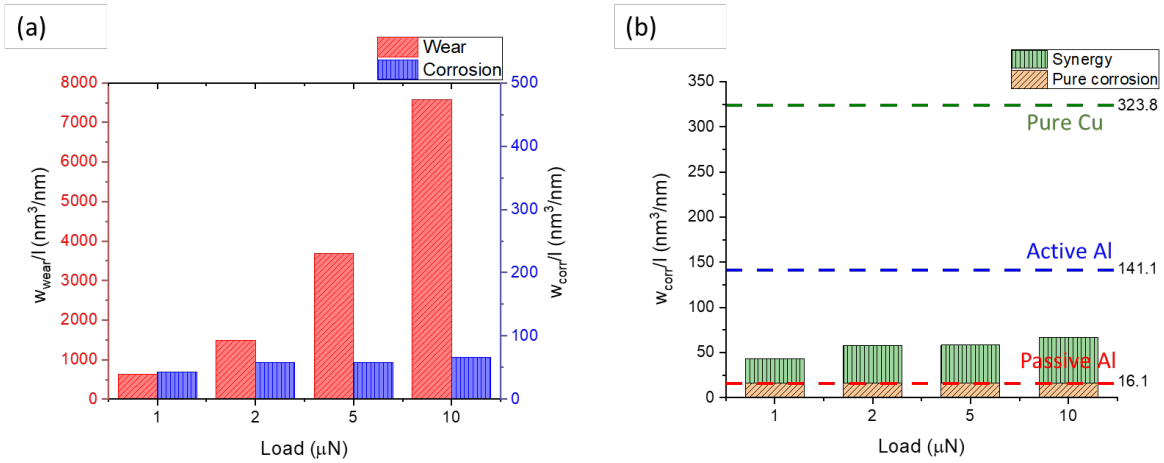

Figure 3.9 FEA model predicted (a) material loss rate (i.e. volume loss/sliding distance) due to wear and corrosion process, and (b) material loss rate from wear-corrosion synergy vs. pure corrosion of Al/Cu NMM (20 nm individual layer thickness) under different load. Dashed lines in (b) represent tribocorrosion rate with the same exposed surface area for surface of passive Al (red), active Al (blue), and Cu (green) respectively.

3.3.4 Effects of layer thickness

The FEA model predicted subsurface stress and strain, and the worn surface profile of Al/Cu NMMs as a function of individual layer thickness (h) from 10 nm to 100 nm are shown in **Fig. 3.10**. As introduced earlier, the plastic deformation of NMMs when the layer thickness is only a few nanometers involves atomic scale interaction between dislocations and interfaces and could not be modeled by FEA, so extremely small h values (e.g. h<10 nm) are not considered here where the Hall-Petch breakdown is expected. It could be seen that at finer layers, the buffering effect of Cu layers was increased and the area of material failure was reduced. A more straightforward indication is shown in **Fig. 3.11**, which summarizes the material loss caused by wear and corrosion in the tribocorrosion test as a function of layer thickness. Both wear and corrosion resistance of the NMM improves with decreasing layer thickness. This is in good agreement with prior experimental observations [14, 37].

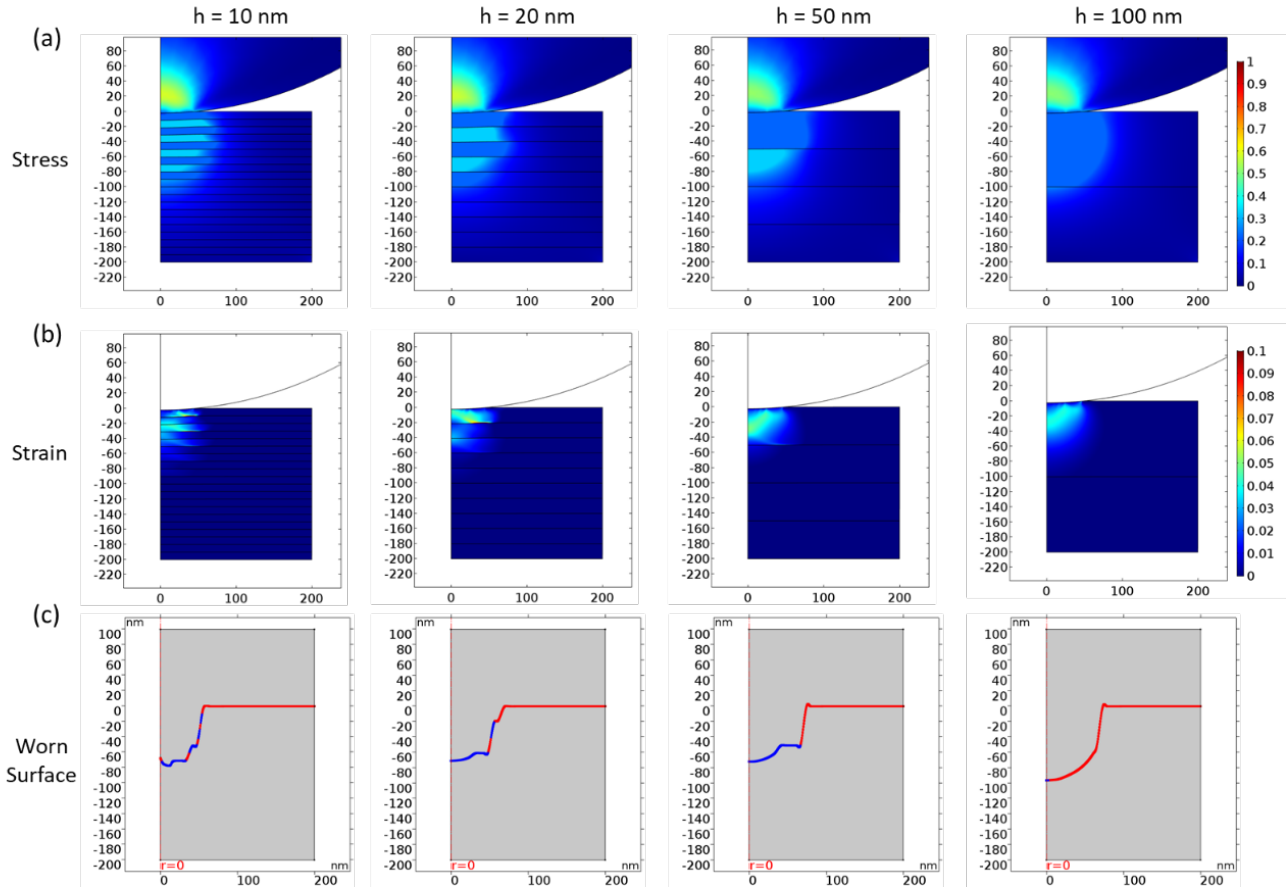

Figure 3.10 FEA model predicted (a) stress, (b) strain distribution, and (c) worn surface profile of Al/Cu NMMs with various individual layer thickness h (10-100 nm) under a load of 5 μN.

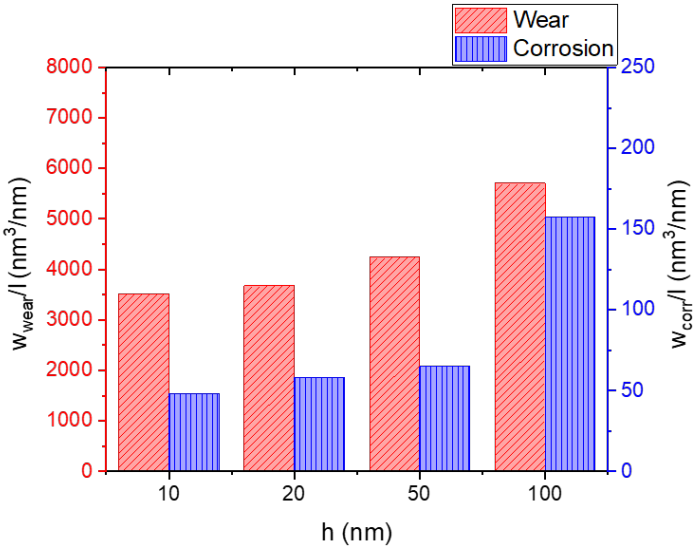

Figure 3.11 Summary of FEA model predicted material volume loss rate due to wear and corrosion processes of Al/Cu NMMs as a function of individual layer thickness from 10-100 nm.

3.3.5 Effects of layer orientation

To evaluate the effects of layer (hence interface) orientation, the wear and tribocorrosion behavior of Al/Cu NMM with vertically aligned layers were studied using the FEA model. The individual layer thickness is kept at 20 nm and the load at 5 μN for easy comparison with the prior simulation results. The results are summarized in **Figs. 3.12-13**. It could be seen that similar to the horizontal layered NMM, the local strain is higher in the Al layers and stress higher in the Cu layers, especially near the Al/Cu interfaces. The worn surface morphology is however quite different, where the Al layers wore deeper than Cu layers, leading to significant surface roughness within the wear track (**Fig. 3.12(c)**). The difference in the worn surface profile and interface direction lead to different corrosion and tribocorrosion rate. As shown in **Fig. 3.13**, the galvanic coupling for vertical layered NMM is more intense, causing a higher corrosion rate than horizontal layered NMMs.

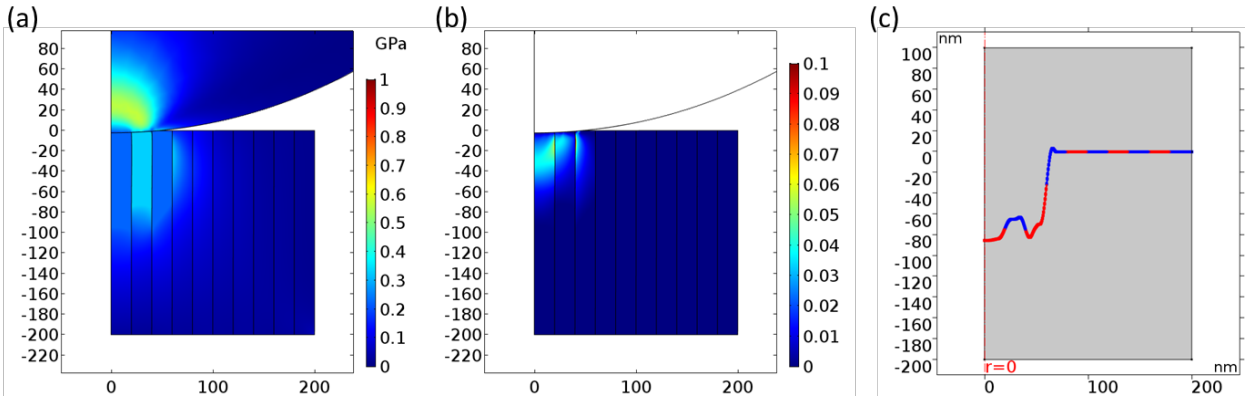

Figure 3.12 FEA model predicted (a) stress, (b) strain (b) strain distribution, and (c) worn surface profile of Al/Cu NMMs with vertically aligned layers of 20 nm under a load of 5 μN.

3.4 Discussion

From the simulation results of wear, it could be inferred that Cu layers experience lower plastic strain than Al layers due to their higher yield strength that helps buffer the yielding of the NMM. This causes significant difference at the edge of wear area since Cu layer may offer protection to the Al layer underneath, preventing material degradation at local areas where Al has already given in. On the other hand, the Al layers act as a sacrificial anode to protect Cu layer from corrosion. Even though this accelerates the dissolution of Al at the beginning, the current interchange between Al and Cu layers helps the repassivation process as time increases. The NMM system quickly

reaches a steady state where Cu doesn't corrode and the corrosion rate of Al is reduced to a very small value. All together, these layered structures lead to the better wear resistance of Al/Cu NMM than pure Al and better tribocorrosion resistance than both Al and Cu.

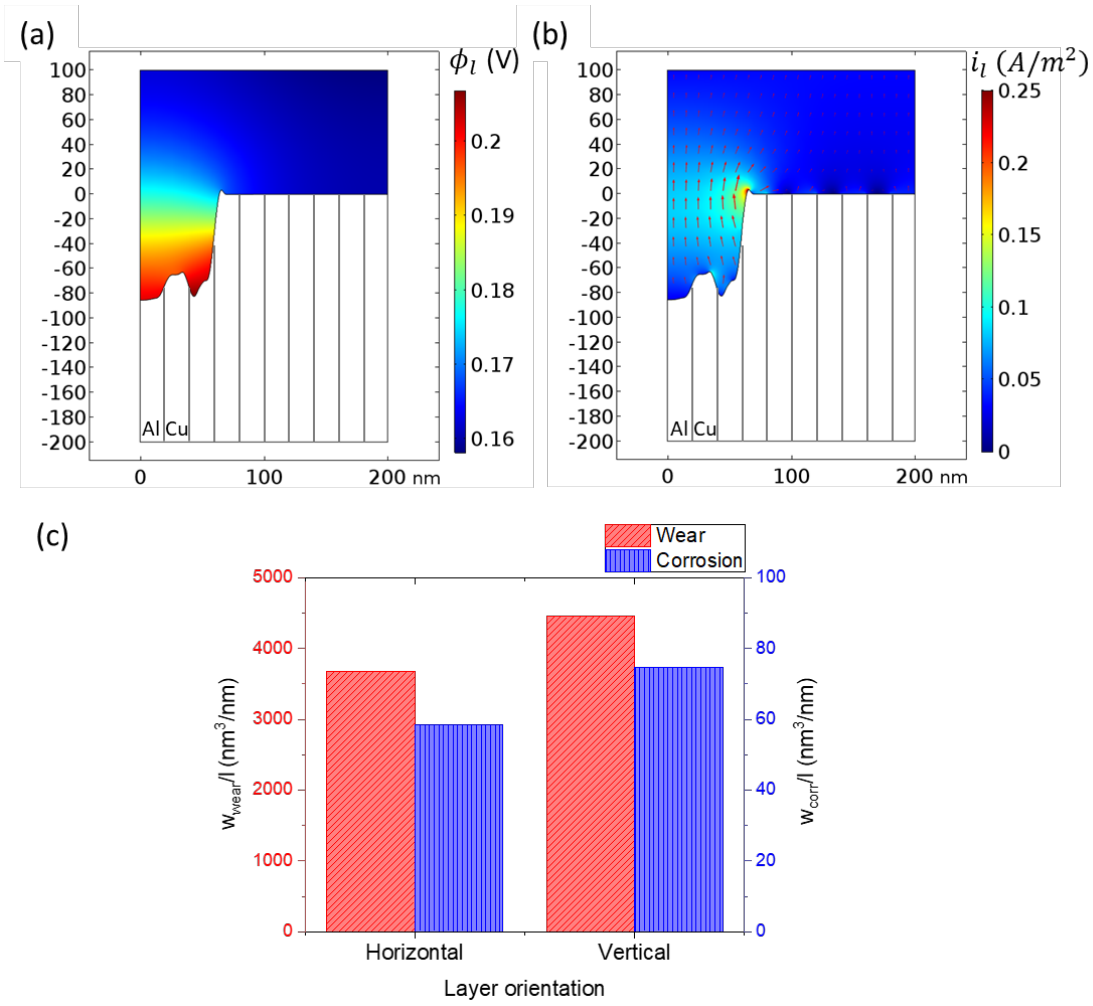

Figure 3.13 FEA model predicted (a) electrolyte potential, and (b) current density distribution of Al/Cu NMMs with vertically aligned layers of 20 nm under a load of 5 μN. (c) Summary of material volume loss rate as a function of layer orientation of Al/Cu NMM.

In terms of layer thickness effect, thinner layers allow a denser arrangement of Cu layers preventing debris formation and material loss, which leads to shallower and narrower wear tracks. Despite the fact that the FEA model didn't account for atomic interactions at layer interfaces and nanoscale dislocation propagations, the model suggests that this structural effect could partially explain the mechanical properties' dependence on layer thickness of the multilayers. In corrosion, thinner layers lead to more concentrated current exchange between the layers. This enhances the cathodic protection of Cu layers as well as promoting the formation of passive layer at exposed Al

layers. This also resembles the experimental observation in intergranular corrosion of Al-Cu alloy [42].

Finally, the FEA model predicts a significant effect of layer orientation on the overall tribocorrosion behavior of NMMs. In the case of vertical layers, deeper material loss was found in the softer Al layers, eventually resulting in higher volume loss from both wear and corrosion process. On the other hand, in parallel layered NMM, Cu layers block the material removal and help sustain the integrity of the layers underneath. This also leads to less exposure of depassivated Al surface area, causing a less severe anodic corrosion of the Al layers and faster repassivation process. Thus, the integrity of vertically aligned multilayers is more likely to be threatened by tribocorrosion than the horizontally aligned multilayers. As a last note, it is worth pointing out that the current simulation treated the surfaces of both indenter and sample as ideally smooth in geometry and did not take contacting asperities into account. For example, Ghanbarzadeh et al. developed an asperity-scale mechanistic model to investigate the influence of surface asperities on wear-corrosion synergy [43]. More accurate treatment of surface contact between the Al/Cu multilayers and the counter body requires systematic characterization of the real contact area experimentally, which is left for future work.

3.5 Conclusions

In this research, a finite element model incorporated with an element removal algorithm is developed to investigate the wear and corrosion in the tribocorrosion process of Al/Cu nanostructured metallic multilayers. The mechanical module of the model was used to simulate the structural interaction between layers and predict the stress, strain distribution as well as the wear track morphology. The electrochemical module of the model takes dynamic process of galvanic corrosion between layers and repassivation of the passive metal layers into account and simulates potential distribution, current density and surface evolution of the corrosion process near the wear track. The developed model was used to study the tribocorrosion of Al/Cu multilayers of different layer thicknesses and orientation under different loading conditions. Key findings include:

(1) the combination of a wear resistant cathodic metal (Cu) and an anodic metal with passive layer (Al) lead to improved tribocorrosion resistance than their monolithic counterparts.

(2) thinner layer thickness (within the range of 10~100 nm) leads to enhanced wear and tribocorrosion resistance in NMMs.

(3) multilayers with layer orientation perpendicular to the surface suffers more severe tribocorrosion than those with parallel arrangement.

The developed model could potentially be extended to investigate tribocorrosion performance of metals and coatings with other complex microstructure (e.g., eutectic structure, dual phase, precipitates of various shape, size, and orientation) under a wide range of loading and corrosion conditions.

References

1. Liu, T., et al., *Corrosion behavior of super-hydrophobic surface on copper in seawater.* Electrochimica Acta, 2007. **52**(28): p. 8003-8007.
2. Roy, S., et al., *Flow-induced failure mechanisms of copper pipe in potable water systems.* Corrosion Reviews, 2018. **36**(5): p. 449-481.
3. Twite, R.L. and G.P. Bierwagen, *Review of alternatives to chromate for corrosion protection of aluminum aerospace alloys.* Progress in Organic Coatings, 1998. **33**(2): p. 91-100.
4. Kim, Y.S., et al., *Influence of a simulated deep sea condition on the cathodic protection and electric field of an underwater vehicle.* Ocean Engineering, 2018. **148**: p. 223-233.
5. Macdonald, D.D., *Passivity - the key to our metals-based civilization.* Pure and Applied Chemistry, 1999. **71**(6): p. 951-978.
6. Was, G.S. and T. Foecke, *Deformation and fracture in microlaminates.* Thin Solid Films, 1996. **286**(1-2): p. 1-31.
7. Schweitz, K.O., et al., *Hardness in Ag/Ni, Au/Ni and Cu/Ni multilayers.* Philosophical Magazine a-Physics of Condensed Matter Structure Defects and Mechanical Properties, 2001. **81**(8): p. 2021-2032.
8. Creus, J., et al., *Mechanical and corrosion properties of dc magnetron sputtered Al/Cr multilayers.* Surface & Coatings Technology, 2008. **202**(16): p. 4047-4055.

9. Xie, T.T., et al., *Structure, corrosion, and hardness properties of Ti/Al multilayers coated on NdFeB by magnetron sputtering.* Vacuum, 2012. **86**(10): p. 1583-1588.
10. Izadi, S., H. Mraied, and W.J. Cai, *Tribological and mechanical behavior of nanostructured Al/Ti multilayers.* Surface & Coatings Technology, 2015. **275**: p. 374-383.
11. Hoagland, R.G., J.P. Hirth, and A. Misra, *On the role of weak interfaces in blocking slip in nanoscale layered composites.* Philosophical Magazine, 2006. **86**(23): p. 3537-3558.
12. Mara, N.A., et al., *Deformability of ultrahigh strength 5 nm Cu/Nb nanolayered composites.* Applied Physics Letters, 2008. **92**(23).
13. Fei, J.Y. and G.D. Wilcox, *Electrodeposition of zinc-nickel compositionally modulated multilayer coatings and their corrosion behaviours.* Surface & Coatings Technology, 2006. **200**(11): p. 3533-3539.
14. Misra, A., J.P. Hirth, and R.G. Hoagland, *Length-scale-dependent deformation mechanisms in incoherent metallic multilayered composites.* Acta Materialia, 2005. **53**(18): p. 4817-4824.
15. Li, J., et al., *Comparison of size dependent strengthening mechanisms in Ag/Fe and Ag/Ni multilayers.* Acta Materialia, 2016. **114**: p. 154-163.
16. Flores, M., et al., *The influence of the period size on the corrosion and the wear abrasion resistance of TiN/Ti multilayers.* Surface & Coatings Technology, 2005. **200**(5-6): p. 1315-1319.
17. Zhao, X.L., Z.H. Xie, and P. Munroe, *Nanoindentation of hard multilayer coatings: Finite element modelling.* Materials Science and Engineering a-Structural Materials Properties Microstructure and Processing, 2011. **528**(3): p. 1111-1116.
18. Mayer, C., et al., *Orientation dependence of indentation behavior in Al-SiC nanolaminate composites.* Materials Letters, 2016. **168**: p. 129-133.
19. Wang, W., et al., *Ultrahigh tribocorrosion resistance of metals enabled by nano-layering.* Acta Materialia, 2021. **206**.
20. Ding, J., et al., *A finite element based approach to simulating the effects of debris on fretting wear.* Wear, 2007. **263**: p. 481-491.
21. Hegadekatte, V., N. Huber, and O. Kraft, *Finite element based simulation of dry sliding wear.* Modelling and Simulation in Materials Science and Engineering, 2005. **13**(1): p. 57-75.

22. Podra, P. and S. Andersson, *Simulating sliding wear with finite element method.* Tribology International, 1999. **32**(2): p. 71-81.
23. Mraied, H. and W.J. Cai, *The effects of Mn concentration on the tribocorrosion resistance of Al-Mn alloys.* Wear, 2017. **380-381**: p. 191-202.
24. Hommel, M., O. Kraft, and E. Arzt, *A new method to study cyclic deformation of thin films in tension and compression.* Journal of Materials Research, 1999. **14**(6): p. 2373-2376.
25. Akchurin, A., R. Bosman, and P.M. Lugt, *A Stress-Criterion-Based Model for the Prediction of the Size of Wear Particles in Boundary Lubricated Contacts.* Tribology Letters, 2016. **64**(3).
26. Woldman, M., et al., *A Finite Element Approach to Modeling Abrasive Wear Modes.* Tribology Transactions, 2017. **60**(4): p. 711-718.
27. Multiphysics, C., *Structural Mechanics Module, User's Guide, Ver 5.3.*
28. Bosman, R. and D.J. Schipper, *Transition from mild to severe wear including running in effects.* Wear, 2011. **270**(7-8): p. 472-478.
29. Nelias, D., V. Boucly, and M. Brunet, *Elastic-plastic contact between rough surfaces: Proposal for a wear or running-in model.* Journal of Tribology-Transactions of the Asme, 2006. **128**(2): p. 236-244.
30. Mraied, H., W.J. Cai, and A.A. Sagues, *Corrosion resistance of Al and Al-Mn thin films.* Thin Solid Films, 2016. **615**: p. 391-401.
31. Mansfeld, F., et al., *Pitting and Passivation of Al-Alloys and Al-Based Metal Matrix Composites.* Journal of the Electrochemical Society, 1990. **137**(1): p. 78-82.
32. Tak, Y.S. and K.R. Hebert, *Initial Events during the Passivation of Rapidly Dissolving Aluminum Surfaces.* Journal of the Electrochemical Society, 1994. **141**(6): p. 1453-1459.
33. Chidambaram, D., C.R. Clayton, and G.P. Halada, *Studies on the repassivation behavior of aluminum exposed to dichromate solution.* State-of-the Art Application of Surface and Interface Analysis Methods to Environmental Materials Interactions: In Honor of James E. Castle's 65th Year, Proceedings, 2001. **2001**(5): p. 282-289.
34. Khaled, K.F., *Studies of the corrosion inhibition of copper in sodium chloride solutions using chemical and electrochemical measurements (vol 125, pg 427, 2011).* Materials Chemistry and Physics, 2011. **130**(3): p. 1394-1395.

35. Wang, K.W., et al., *Multiphysics modeling and uncertainty quantification of tribocorrosion in aluminum alloys.* Corrosion Science, 2021. **178**.
36. Xu, L.Y. and Y.F. Cheng, *Development of a finite element model for simulation and prediction of mechanoelectrochemical effect of pipeline corrosion.* Corrosion Science, 2013. **73**: p. 150-160.
37. Wen, S.P., et al., *Investigation of the wear behaviors of Ag/Cu multilayers by nanoscratch.* Wear, 2008. **265**(11-12): p. 1808-1813.
38. Fu, K.K., et al., *Plastic behaviour of high-strength lightweight Al/Ti multilayered films.* Journal of Materials Science, 2017. **52**(24): p. 13956-13965.
39. Berger, M., et al., *The multilayer effect in abrasion - optimising the combination of hard and tough phases.* Surface & Coatings Technology, 1999. **116**: p. 1138-1144.
40. Fu, K.K., et al., *Comparative study on plasticity and fracture behaviour of Ti/Al multilayers.* Tribology International, 2018. **126**: p. 344-351.
41. Badawy, W.A., F.M. Al-Kharafi, and A.S. El-Azab, *Electrochemical behaviour and corrosion inhibition of Al, Al-6061 and Al-Cu in neutral aqueous solutions.* Corrosion Science, 1999. **41**(4): p. 709-727.
42. Galvele, J.R. and S.M. Demicheli, *Mechanism of Intergranular Corrosion of Al-Cu Alloys.* Corrosion Science, 1970. **10**(11): p. 795-+.
43. Ghanbarzadeh, A., et al., *A New Asperity-Scale Mechanistic Model of Tribocorrosive Wear: Synergistic Effects of Mechanical Wear and Corrosion.* Journal of Tribology, 2019. **141**(2).

Chapter 4. A Combined Experimental and Computational Investigation of Crystallographic Orientation Effects During Tribocorrosion of Aluminum Single Crystals

4.1 Introduction

Aluminum (Al) and its alloys are widely used passive metals for applications that require lightweight, anti-corrosion materials, including marine industry, coastal infrastructures, transportation, aerospace and energy devices, etc. [1-6] Pure Al, along with its alloys, benefit from a naturally formed dense oxide layer which protects the metal from further corrosion [7, 8]. However, in complex service conditions, what jeopardizes the longevity of the Al-based structure is more often tribocorrosion, namely the synergistic material degradation caused by wear and corrosion [2, 9-11]. The mechanical damage during wear often leads to significantly increased corrosion rate locally for Al under tribocorrosion scenario due to the depassivation on the wear track, and the microgalvanic coupling between the passivated and depassivated surface regions [12, 13]. Thus, understanding the tribocorrosion behavior and mechanism of Al is extremely important from both scientific and technical perspectives.

Theories based on experimental investigations have been developed to account for the localized, accelerated corrosion inside the wear track for passive metals such as Al and Ti alloys [14-16]. Based on experimental results on Al 7075-T6 alloys, Li et al. [17] proposed that the accelerated corrosion for samples under tribocorrosion is due to galvanic coupling between the worn region which is depassivated and the unworn region which is passive. In another research carried out on stainless steel, Chen et al. [18] found that the phase transformation induced by plastic deformation will lead to micro-galvanic coupling between different phases, causing localized and accelerated corrosion. So far, the developed tribocorrosion models of passive metals often consider the effects of wear and electrochemical testing parameters on the overall material response by treating the material with isotropic properties at the macroscopic scale [11, 19, 20].

In addition to experimental investigations, attempts to build numerical models to explain localized stress corrosion or tribocorrosion has been explored using finite element (FE) method [21]. Cheng [22] proposed a stress corrosion mechanism which is capable of explaining the shift

in equilibrium potential due to the increase in dislocation induced by plastic strain based on theories developed by Gutman [23]. FE models were built based on this mechanism for the case study in stainless steel pipelines and successfully accounted for the localized accelerated corrosion in plastically deformed areas [24, 25]. Another attempt to predict corrosion current and material loss during tribocorrosion for Al-Mn alloys was made by our group [13] using FE simulations, where the depassivation/repassivation effect and potential shift due to plastic strain was taken into account to predict accelerated corrosion during tribocorrosion.

However, none of the prior experimental or computational works considers tribocorrosion at the crystal level, where wear-induced lattice reorientation and dislocation generation could affect the local corrosion kinetics, hence the overall material degradation. Indeed, prior investigations show that crystallographic orientation affects plasticity, wear, and corrosion separately. For example, both experiment and simulation have confirmed the anisotropy in mechanical and electrochemical behavior for metal surface with different crystal orientations [26-29]. For example, Komanduri et al. demonstrated the anisotropy in hardness and friction by simulating indentation and scratching on single crystal Al in various crystal orientations and directions using molecular dynamics simulations [30, 31]. Liu et al. predicted the difference in load-displacement curves, pile-up patterns and lattice rotation angles of Al using crystal plasticity FE method [32]. Filippov et al. confirmed the anisotropy in Young's modulus and hardness for Al single crystal samples using Vickers nano-indentation test. On the other hand, for electrochemical behavior, Yasuda et al. [33], Treacy et al. [34] and Davis et al. [35] reported differences in the open circuit potentials, pitting potentials, and metastable pitting frequencies of single crystal Al samples with different surface orientations. Thus, it is necessary to include the crystallographic effect into the model to have a thorough quantitative understanding of the tribocorrosion mechanism of Al at the crystal level.

In this paper, both experiments and multiphysics FE simulation method were exploited to investigate the tribocorrosion behavior and its underlying mechanism of single crystal pure Al samples. Micro-indentation test and electrochemical test were carried out to characterize the mechanical and electrochemical properties of the Al samples with (100), (110) and (111) surface planes (denoted as (100), (110) and (111) samples hereafter). A linear interpolation method proven by the research by Bland et al. [36] and Barrett et al. [37] was used to interpolate electrochemical properties of a given crystal orientation based on the measured results of (100), (110) and (111)

samples. After the tribocorrosion tests, EBSD characterization of the tribocorroded surfaces was performed and the measured local crystal information (e.g. orientation and dislocation density) were used as model inputs. Finally, a quantitative FE model was developed and validated, which accurately predicted the corrosion current evolution during tribocorrosion by considering the local passivation state, lattice reorientation, and subsurface dislocations. The structure of the project, including experimental data acquisition, simulation, and validation is demonstrated in **Fig. 4.1(a)**. This model has great significance in understanding the fundamental tribocorrosion mechanisms at the crystal level, shedding light on future computational research on tribocorrosion of polycrystal metals and alloys that are of more practical importance.

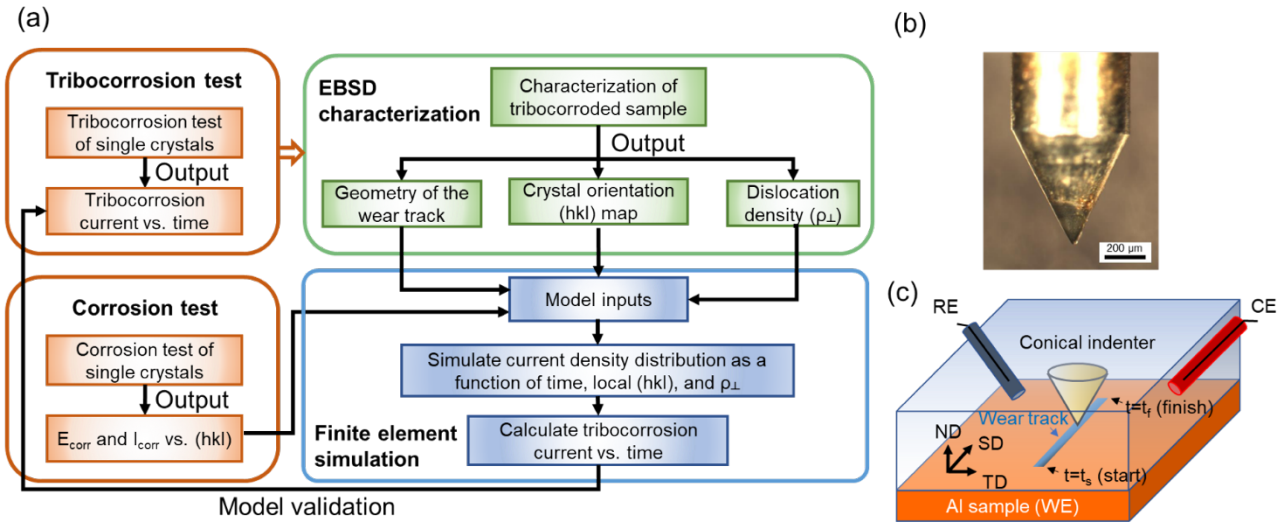

Figure 4.1 (a) Flowchart of the experiment and FE simulation integration, including experimental data acquisition, analysis, simulation, and model validation steps. (b) Optical microscopic image of the conical tip used for the micro-indentation and tribocorrosion experiments, and (c) schematic of the tribocorrosion test, where ND, SD, TD represents the normal, scratching, and transverse direction respectively.

4.2 Experimental Methods

4.2.1 Material, mechanical, electrochemical, and tribocorrosion testing

(100), (110), and (111) single crystal pure Al samples of >99.99% purity and 10×10×0.5 mm size was obtained from MTI Corp, CA. Micro-indentation tests were carried out using a multifunctional tribometer (Rtec MFT-5000, CA) and the load-displacement curves were collected

to characterize the mechanical properties of all samples. A sharp conical diamond tip with a half angle of 30° and 12.5 micron radius, as shown in **Fig. 4.1(b)**, was used as the indenter. A trapezoidal loading function with 0.1 N max load, and 0.005 N/sec loading and unloading rates was used.

The potentiodynamic polarization curves of all samples were measured from a three-electrode setup using a Gamry 600 potentiostat/galvanostat/ZRA in neutral 0.6 M NaCl aqueous solution at room temperature. An exposed area of 1 cm^2 of the sample was used as the working electrode (WE). The counter electrode (CE) and the reference electrode (RE) were the mixed metal oxide coated Ti mesh and 1 M KCl Ag/AgCl electrode respectively. A stabilization step of 5 min at the open circuit potential was run before each potentiodynamic (PD) measurement, after which, the PD tests were conducted within -1.7 to -0.2 V vs. RE. The corrosion potential (E_{corr}), corrosion current density (i_{corr}), anodic and cathodic transfer coefficient (α_a and α_c) was obtained using Tafel extrapolation method from these polarization curves at ±100 mV above and below the open circuit potential. The transfer coefficient α could be calculated from Tafel slope β using equation

$$\alpha = \frac{2.303 k_B T}{e\beta} \tag{4.1}$$

where k_B is the Boltzmann's constant ($1.380649 \times 10^{-23}\, J \cdot K^{-1}$), T is the absolute temperature (293.15K) and e is the charge of an electron ($1.602 \times 10^{-19} C$). It is also noted later that the deviation of Tafel behavior was observed in the cathodic branch at the range below ~ -1.5 V vs. RE, likely due to the diffusion controlled cathodic behavior of H_2 generation.

A schematic of the tribocorrosion test is plotted in **Fig. 4.1 (c)**. The tribocorrosion tests of all samples were carried out using the multifunctional tribometer (Rtec MFT-5000, CA) and the 12.5 micron conical diamond indenter in neutral 0.6 M NaCl aqueous solution at room temperature. To ensure that all samples reach a uniform, stable electrochemical state prior to the tribocorrosion test, all the samples were anodized at a constant potential of -1 V vs. the RE for 3 hours before the test. A single stroke scratching test at 0.1 mm/s speed over 2 mm scratch length was carried out for each sample. The total tribocorrosion current evolution was recorded as a function of scratching time and compared with the simulation results afterwards. The selection of a hard micro-indenter tip and a single stroke wear mode, instead of flat-on-flat reciprocal wear modes allows the easy capture of wear contact area and temporal evolution of surface corrosion kinetics. All reported tests were repeated for at least 2 times.

4.2.2 Materials characterization

The EBSD characterization was carried out on the tribocorroded samples using a FEI Helios 600 FIB microscope at 20 kV and 1.4 nA. The cross-sectional samples (in the ND-TD plane, as defined in **Fig. 4.1(c)**) were prepared by mechanical polished with SiC sandpaper down to 1200 grits, followed by fine polishing using alumina suspension of 1 μm, 0.3 μm and 0.05 μm and a final step of vibratory polishing on the Buehler Vibromet2 polisher with 0.02 μm colloidal silica suspension to remove the residual stress induced by mechanical polishing. EBSD orientation maps of 140 μm × 113 μm sizes were acquired at spot size of 200 nm. The dislocation density was calculated from the EBSD result using the MTEX package [38], based on the method proposed by Pantleon [39], which correlates the dislocation density tensor with the curvature of the crystalline lattice using Nye's tensor [40] $\alpha_{ik} = \kappa_{ki} - \delta_{ki}\kappa_{mm}$, where α_{ik} denotes the ik component of the dislocation density tensor, κ_{ki} denotes the ki component of the lattice curvature tensor, δ_{ki} is the Kronecker delta function. κ_{mm} is the sum of the three diagonal components $\kappa_{mm} = \kappa_{11} + \kappa_{22} + \kappa_{33}$. It's worth noting that the 2D cross-sectional EBSD data lacks information along SD, which is assumed to be negligible due to the similar loading conditions for every cross-sectional plane along SD. Thus, the value for dislocation density is considered to be only slightly underestimated using this method. The initial dislocation density (N_0) of the as-received samples was obtained by averaging the dislocation density from areas far away from the wear track (~ 80 - 100 μm below the surface).

4.3 Multiphysics FE models

Fig. 4.1(a) summarizes the flowcharts of the integration of experiments and FE simulations. Specifically, experimentally measured wear track geometry, EBSD map, and dislocation density map was used as inputs of the FE model, while the measured tribocorrosion current evolution used as model validation, as detailed next. The tribocorrosion model reflecting a 2D cross-section plane normal to the SD was built based on the EBSD data. In this model, three factors are considered to account for the localized, accelerated corrosion in the vicinity of the wear track: (1) galvanic coupling between the different crystal orientations, (2) change of corrosion potential due to the increase in dislocation density, and (3) loss of protection due to depassivation in the wear track.

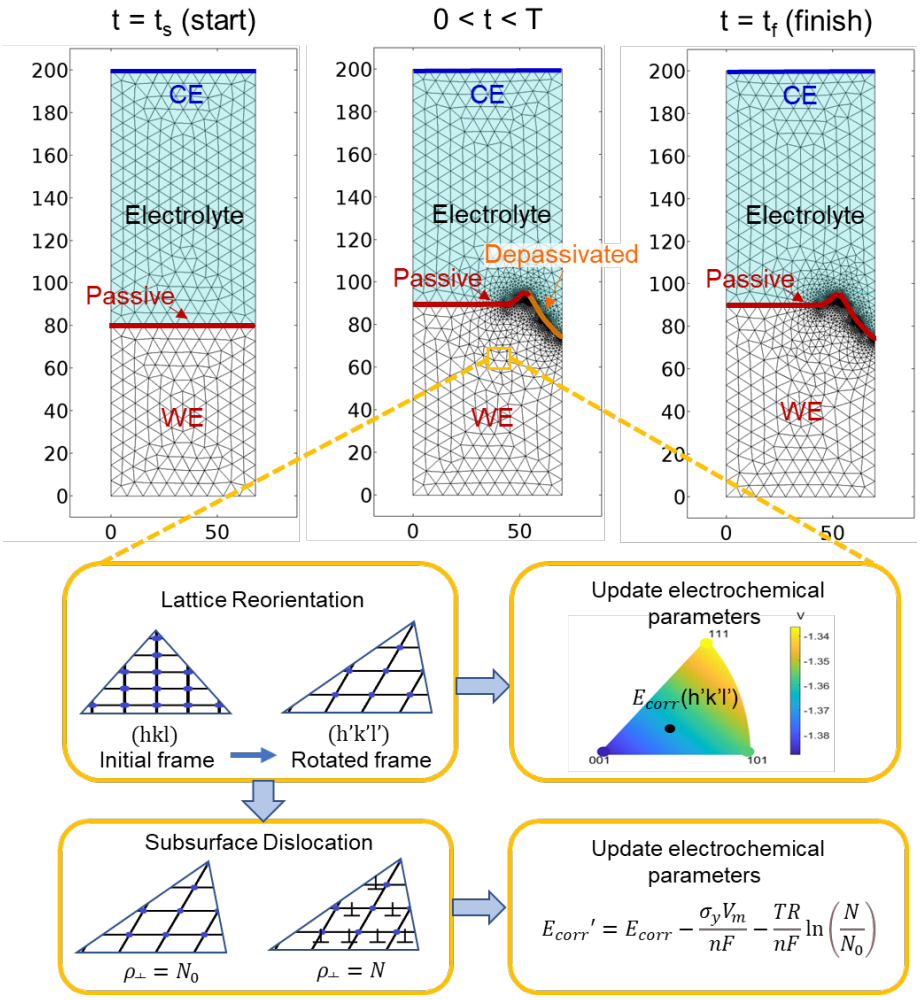

Figure 4.2 Summary of the FE tribocorrosion model setup and geometry, where the whole surface was modeled to be passive before ($t \leq ts$) and after ($t \geq tf$), and partially passive during ($ts < t < tf$) the tribocorrosion test. The local electrochemical parameters (e.g. Ecorr) was modeled by considering the lattice reorientation and dislocation density effects, using experimental inputs.

4.3.1 Geometry and meshing

A 2D model with simple rectangular geometry was built for the electrochemical test, as well as tribocorrosion test prior to scratching, as shown in **Fig. 4.2** for $t < t_s$, where t_s represents the starting time of scratching. The domain in between the Al surface (WE) and Ti surface (CE) is the electrolyte and the domain below the Al surface is the Al electrode. A uniform meshing size of 7.5 μm was assigned for the electrolyte and Al sample.

During tribocorrosion ($t_s < t < t_f$), the geometry of the wear track at the sample surface is determined from EBSD measurements by the boundary between confidence index (CI) larger than 0.1 and smaller than 0.1. As shown in **Fig. 4.2**, the meshing size is coarser (7.5 μm) for sample and electrolyte regions far away from the wear track, while near the wear track, where there is intense galvanic coupling, a finer mesh with a minimum size of 0.025 μm was used. The total worn area was calculated by multiplying the cross-sectional area by the scratching distance, which increased with scratching time.

After the scratching was finished ($t > t_f$), the whole wear track (over the entire scratch length) was assumed to be passive again, where the repassivation kinetics was modeled to be governed by the oxide growth on the wear track, as described next.

4.3.2 Governing equations and boundary conditions for electrochemical test

Using the parameters from the experimental polarization curve, a simulated polarization curve was produced and compared to the one obtained from experiment to prove the validity of the current density predicted under different potential. The applied potential between the WE and CE was swept between -1.6 and -0.8 V with a step size of 0.1 V and the current density was simulated. In the cathodic part of the curve, of which the applied potential is below the open-circuit potential, the corrosion reaction kinetics on Al surface is assumed to follow the Butler-Volmer equation:

$$i_{B-V} = i_{corr}\left(exp\left(\frac{\alpha_a F\eta}{RT}\right) - exp\left(\frac{\alpha_c F\eta}{RT}\right)\right), \tag{4.2}$$

where i_{corr} stands for the equilibrium corrosion current density, α_a and α_c stands for the anodic and cathodic transfer coefficient respectively. η stands for the overpotential, which could be expressed as

$$\eta = E_{app} - E_{el} - E_{corr} \tag{4.3}$$

where E_{app} is the applied potential, E_{el} is the potential drop in the electrolyte and E_{corr} is the corrosion potential obtained from the experiment.

In the anodic part of the curve where the applied potential becomes higher than the open-circuit potential, the Al is anodized and the current density is also affected by the thickness of the passive layer. The passive layer will form at a rate according to Faraday's laws:

$$v_n = \frac{i_{B-V}M}{nF\rho}, \tag{4.4}$$

where M is the molar mass of aluminum oxide, n is the number of electrons transferred in forming one Al_2O_3 molecule, which is 3 in this case, F is the Faraday's constant (96485 C/mol), and ρ is the density of the aluminum oxide. The thickness of the oxide s is calculated based on this passivation rate

$$s(t) = \int_o^t v_n(t)dt = \frac{M}{nF\rho}\int_o^t i_{B-V}(t)dt \tag{4.5}$$

The electrical resistance of aluminum oxide was used to account for the passivation effect of the entire surface. The conductivity of the aluminum oxide σ was taken as $1 \times 10^{-12} S/m$. In this case, the overpotential η needs to further exclude the potential drop on the oxide film and eq. (1) changes to

$$\eta = E_{app} - E_{el} - E_{corr} - i_{B-V}(t)\frac{s(t)}{\sigma} \tag{4.6}$$

The Butler-Volmer current and oxide thickness from the previous time step was used to calculate the overpotential in eq. (5) and then predict the Butler-Volmer current of the new time step. The final Butler-Volmer current density was predicted with 1 min passivation time with a time step of 1s for each applied potential step.

4.3.3 Governing equations and boundary conditions for tribocorrosion

The simulation of tribocorrosion was realized by coupling the Butler-Volmer electrochemical kinetics with crystal orientation and dislocation density, as shown in the **Fig. 4.2**. First, the effect of crystal orientation on local electrochemical properties, including corrosion potential and corrosion current density, was implemented through linear interpolation from the experimental data of three representative orientations using a MATLAB code. By solving (E_0, E_1, E_2) from the following equation set,

$$\begin{cases} E_0 + E_1\, tan(\theta_{(001)}/2)\, cos\, \Phi_{(001)} + E_2\, tan(\theta_{(001)}/2)\, sin\, \Phi_{(001)} = E_{corr(001)} \\ E_0 + E_1\, tan(\theta_{(011)}/2)\, cos\, \Phi_{(011)} + E_2\, tan(\theta_{(011)}/2)\, sin\, \Phi_{(011)} = E_{corr(011)} \\ E_0 + E_1\, tan(\theta_{(111)}/2)\, cos\, \Phi_{(111)} + E_2\, tan(\theta_{(111)}/2)\, sin\, \Phi_{(111)} = E_{corr(111)} \end{cases} \tag{4.7}$$

the corrosion potential of a random orientation (hkl) could be obtained using the equation

$$E_{corr(hkl)} = E_0 + E_1\, tan(\theta_{(hkl)}/2)\, cos\, \Phi_{(hkl)} + E_2\, tan(\theta_{(hkl)}/2)\, sin\, \Phi_{(hkl)} \tag{4.8}$$

The same interpolation method was also applied to obtain corrosion current density i_{corr} for (hkl) plane. Using the interpolated E_{corr} and i_{corr}, local values of E_{corr} and i_{corr} were calculated

based on the crystal orientation obtained from EBSD. Due to the difference between the step size of EBSD data and the meshing size, the maps for E_{corr} and i_{corr} were smoothed with piecewise cubic method between adjacent points.

The effect of dislocation density on electrochemical thermodynamics and kinetics was implemented using the theory developed by Gutman. The increase in dislocation density caused by wear will increase the active corrosion site, resulting in a drop in the corrosion potential following [23, 24]:

$$E_{corr}{}' = E_{\mathrm{corr}} - \frac{\sigma_y V_m}{nF} - \frac{TR}{nF}\ln\left(\frac{N}{N_0}\right) \tag{4.9}$$

where σ_y is the yield strength, V_m is the molar volume of aluminum ($V_m = 9.99 \times 10^{-6} m^3/mol$), T is temperature (T=298 K at room temperature), R is the ideal gas constant (R=8.3145J/(mol · K)), n is the electron involved in the reaction (n=3), F is the Faraday's constant (F=96485 C/mol), N is the local dislocation density and N_0 is the original dislocation density before wear measured from EBSD results.

The passive region was defined as the surface starting from the highest point of the surface to the outside boundary. For the passive region, an 4.5 nm oxide was assigned which is the average of the measured thickness of 3.8~5.1nm for aluminum oxide in NaCl solution environment reported by Natishan et al. [41]. Inside the wear track, the depassivated region, starting from the highest point to the bottom of the wear track, is given an initial oxide thickness of 0 and allowed to grow according to eq. (3) and (4). This corresponds to the situation which the indenter has just slid pass the cross-section plane, removing the passive layer which grows to repassivate the surface afterwards.

4.4 Results and discussions

4.4.1 Mechanical and corrosion properties of Al single crystals

Fig. 4.3 (a) shows the load-displacement curves collected by the indentation tests. A difference in the maximum displacement could be observed, with (111) sample possessing the lowest indentation depth, which is 6.33 μm, indicating it is the hardest orientation, while (100) is the softest with a max. depth of ~ 7.00 μm. This result agrees with the hardness ranking indicated by

experiments from Liu et al. [32]. The maximum displacement for (111) sample is 10.6% larger than that for (100) sample. Using the mechanical properties of samples with different surface orientations listed in **Table 1** from literatures [30, 32], the load-displacement curve was also simulated using the FE method, which matched well with the experimental results. The detailed information could be found in the supplementary materials.

Table 4.1 Mechanical properties of the (100), (110) and (111) Al used in this work.

Al crystal / Mechanical Properties	(100)	(110)	(111)	Ref
E (GPa)	76.1	63.7	72.6	[30]
σ_y (MPa)	61.39	61.63	63.12	[32]

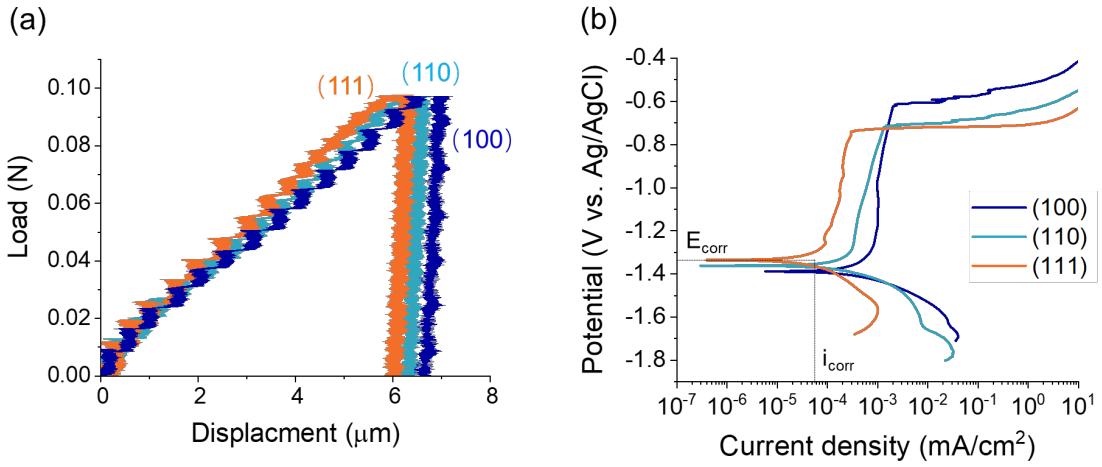

Figure 4.3 Experimentally measured (a) load-displacement curves from dry micro-indentation test, and (b) potentiodynamic polarization curves of (100), (110), and (111) Al single crystal samples in 0.6 M NaCl aqueous solution.

Fig. 4.3 (b) plots the results for the potentiodynamic curves of all samples, reflecting their differences in electrochemical properties, including corrosion potential, pitting potential and corrosion current density. The corrosion potential, corrosion current density, anodic and cathodic transfer coefficient was obtained using Tafel extrapolation method introduced in 4.2.1, and the results are listed in Table 2. These parameters indicate that the corrosion resistance could be ranked (111) > (110) > (100). This ranking agrees with the trend indicated by [33] and [34]. Li et al.

reported different stress corrosion behavior with Al alloys with different texture, with stress corrosion cracks more likely to propagate along the <100> direction, which could also be related to the faster corrosion of the (100) surface [42].

4.4.2 Tribocorrosion behavior

Fig. 4.4 (a) shows the results of tribocorrosion tests for (111) sample under different vertical load during scratching. The scratching process begun at 100s and ends at 120s. A sudden surge of the total current could be observed at the beginning of the scratching process and the current keeps increasing as the worn area expands. The current drops after the scratching process but remains higher than that before the scratching for some time before gradually reducing to the original level. The peak current is not linear with the vertical load. Instead, the higher the vertical load is, the smaller the increase in peak current is.

Fig. 4.4 (b) demonstrates the current change during tribocorrosion test for different samples under the same 0.3 N vertical load. It could be seen that even though the performance for pure wear and pure corrosion follows the ranking: (100) < (110) < (111), the tribocorrosion performance reflected by current increase of three samples are similar. This experimental finding proves once again that the tribocorrosion material loss is not the same as the simple summation of the wear and corrosion. The reason for similar tribocorrosion current will be explained later in the simulation.

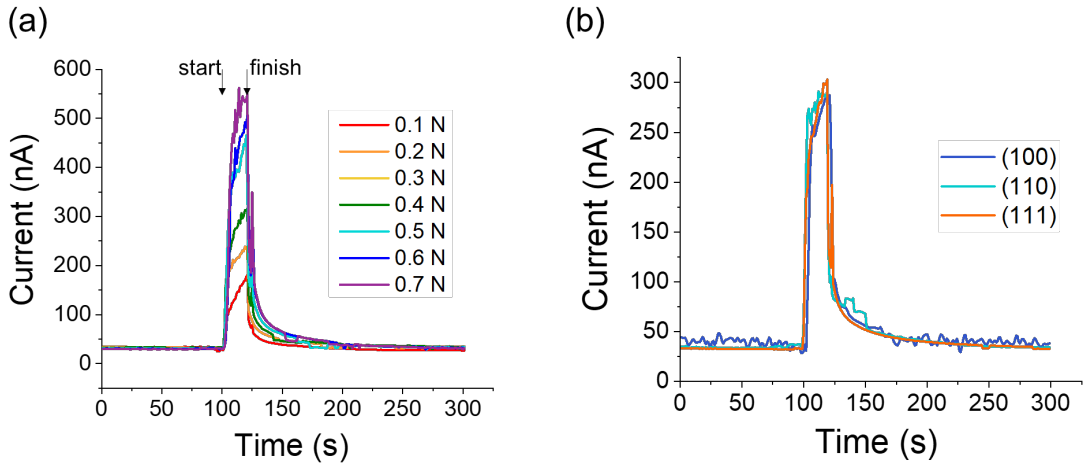

Figure 4.4 Tribocorrosion experiment results: (a) Temporal evolution of corrosion current of (111) Al sample during tribocorrosion test under different loads of 0.1 – 0.7 N. (b) Corrosion current evolution of all samples during tribocorrosion under 0.3 N normal load.

4.4.3 Subsurface characterization of tribocorroded samples

Fig. 4.5-7 shows the results of EBSD characterization of the cross-section plane vertical to the scratching direction (SD) of the tribocorrosion-tested (100), (110) and (111) samples respectively. The wear track generated under the load of 0.3 N is selected. For all three surfaces, the figure (a) is the SEM image of the characterized plane, while (b), (c) and (d) corresponds to the inverse pole figure (IPF) plots with the [37] crystal plane is parallel to the ND, SD and TD of the sample direction respectively. It could be inferred that the plastic deformation propagates more along the transverse direction in the case of (100) and (111) samples, while it propagates equally in the normal direction and transverse direction in the case of (110). This is similar to what is predicted by molecular dynamics simulation by Komanduri et al. [31]. From the SEM images, it could be measured that the wear depth of (100), (110) and (111) sample is 15.8 µm, 15.3 µm and 14.0 µm respectively, consistent with ranking of the hardness data and the results of the indentation test.

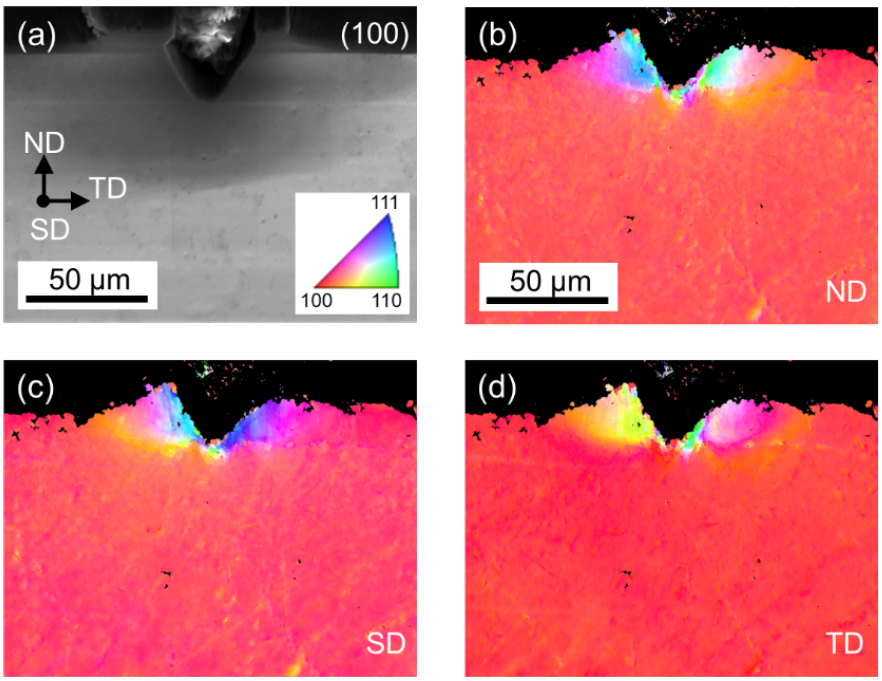

Figure 4.5 (a) SEM image and (b-d) corresponding EBSD maps of (100) Al cross-sectional sample after tribocorrosion test under 0.3 N. Images (b), (c), and (d) are plotted with orientations in the ND, SD, TD directions respectively, as defined in Fig. 1(b). All EBSD maps are color coded per the triangle legend in (a).

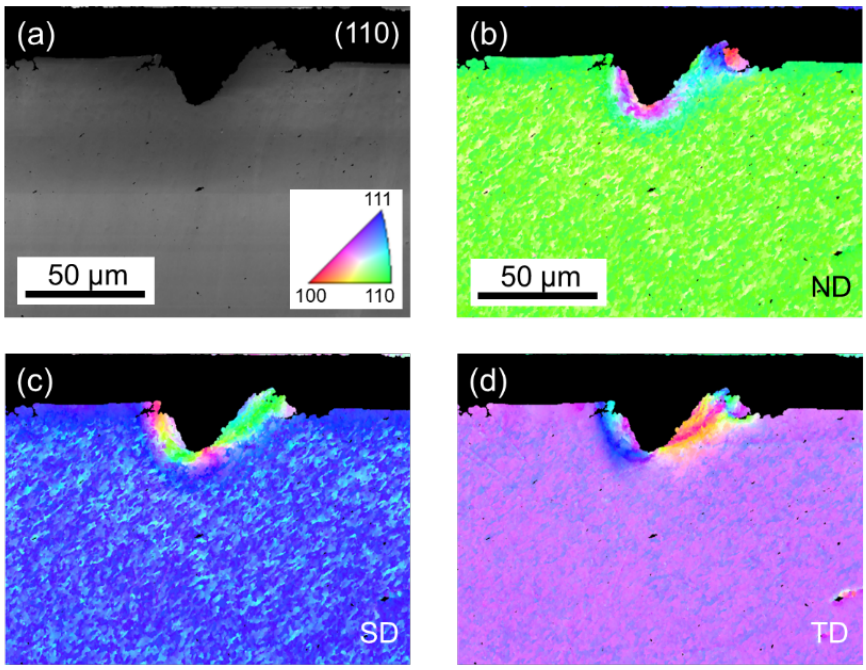

Figure 4.6 (a) SEM image and (b-d) corresponding EBSD maps of (110) Al cross-sectional sample after tribocorrosion test under 0.3 N. Images (b), (c), and (d) are plotted with orientations in the ND, SD, TD directions respectively, as defined in Fig. 1(b). All EBSD maps are color coded per the triangle legend in (a).

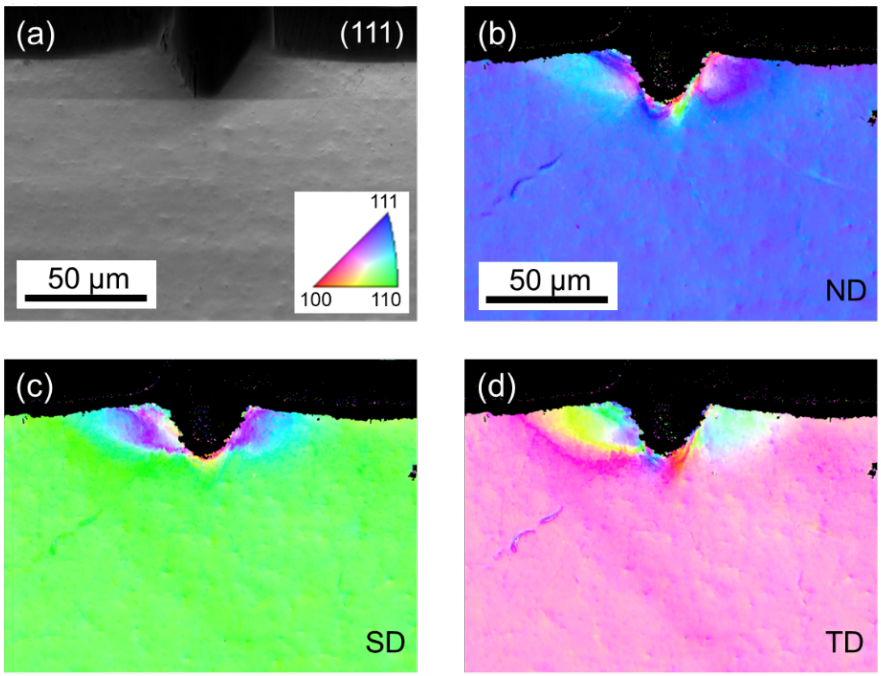

Figure 4.7 (a) SEM image and (b-d) corresponding EBSD maps of (111) Al cross-sectional sample after tribocorrosion test under 0.3 N. Images (b), (c), and (d) are plotted with orientations in the ND, SD, TD directions respectively, as defined in Fig. 1(b). All EBSD maps are color coded per the triangle legend in (a).

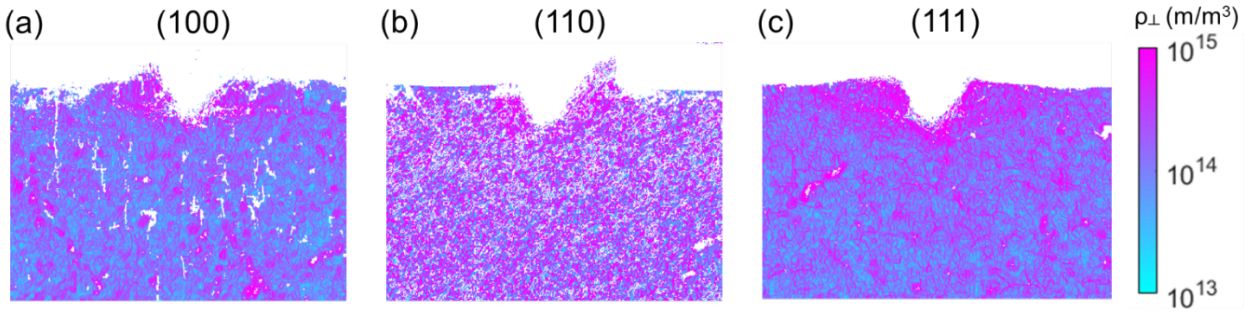

Figure 4.8 Calculated dislocation density maps of (a) (100), (b) (110), and (c) (111) tribocorroded sample obtained from EBSD results shown in Figs. 4.5-7.

The dislocation density left in the sample after tribocorrosion test was obtained using these EBSD data and plotted in **Fig. 4.8**. An increase in the dislocation density at the region near the wear track compared to the region away from the wear track could be observed. The N_0 for (100), (110) and (111) samples are $7.9 \times 10^{13}, 7.2 \times 10^{14} and\ 7.7 \times 10^{13}\ m^2$, obtained from average dislocation density of far away from the wear track. This is similar to the dislocation density change observed in nanocrystalline Al under wear [43].

Table 4.2 Electrochemical properties of the (100), (110) and (111) samples obtained from experimentally measured polarization curves, where E_{corr}, i_{corr}, and α_c and α_a represents the corrosion potential, corrosion current, and the cathodic and anodic transfer coefficient respectively.

Al crystal / **Corrosion Properties**	**(100)**	**(110)**	**(111)**
E_{corr} **(V vs. Ag/AgCl)**	-1.388±0.011	-1.362±0.036	-1.336±0.010
i_{corr} (mA/cm^2)	$(3.83\pm1.04) \times 10^{-4}$	$(1.65 \pm 0.34) \times 10^{-4}$	$(4.35 \pm 0.85) \times 10^{-5}$
α_c	0.4868±0.0025	0.4856±0.0114	0.4841±0.0068
α_a	0.2425±0.0504	0.2341±0.0231	0.2435±0.0219

4.4.4 Tribocorrosion simulation results

Based on the parameters in **Table 2**, polarization curves of different surfaces are predicted by simulation and compared to the experimental curves. As shown in **Fig. 4.9 (a)**, the simulated curves agree well with the experimental curves, proving the effectiveness of the electrochemical kinetics setup in the model as well as the input parameters for (100), (110) and (111) samples.

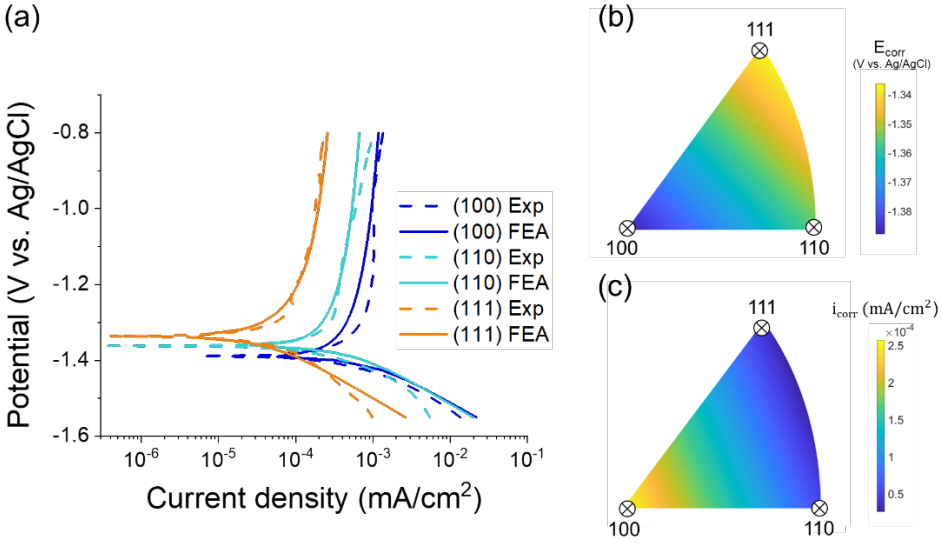

Figure 4.9 (a) Load-displacement curves of all samples predicted by FE indentation simulation in comparison with experiments. (b) Interpolated corrosion potential and (c) corrosion current density map as a function of crystal orientations. Cross marks in (b) and (c) corresponds to experimental measurements, while the rest were interpolated per algorithm detailed in Section 4.3.3.

Using the interpolation method introduced in eq. (4.7) and (4.8) and the electrochemical parameters obtained for (100), (110) and (111) samples, the E_{corr} and i_{corr} for any surface is demonstrated in **Fig. 4.9 (b) and (c)**. The anodic and cathodic transfer coefficient is not interpolated because the variance is negligible.

Combining the interpolated values of E_{corr} and i_{corr} with the IPF data, maps of local E_{corr} and i_{corr} for the deformed samples were obtained as plotted in **Fig. 4.10**. After considering the dislocation density effect using eq. (4.3), $E_{corr}{}'$ is plotted in **Fig. 4.11** in the sample region. The resulting current density distribution in the electrolyte for the tribocorrosion system is also plotted in **Fig. 4.11**, reflecting the higher current density in the vicinity of the wear track.

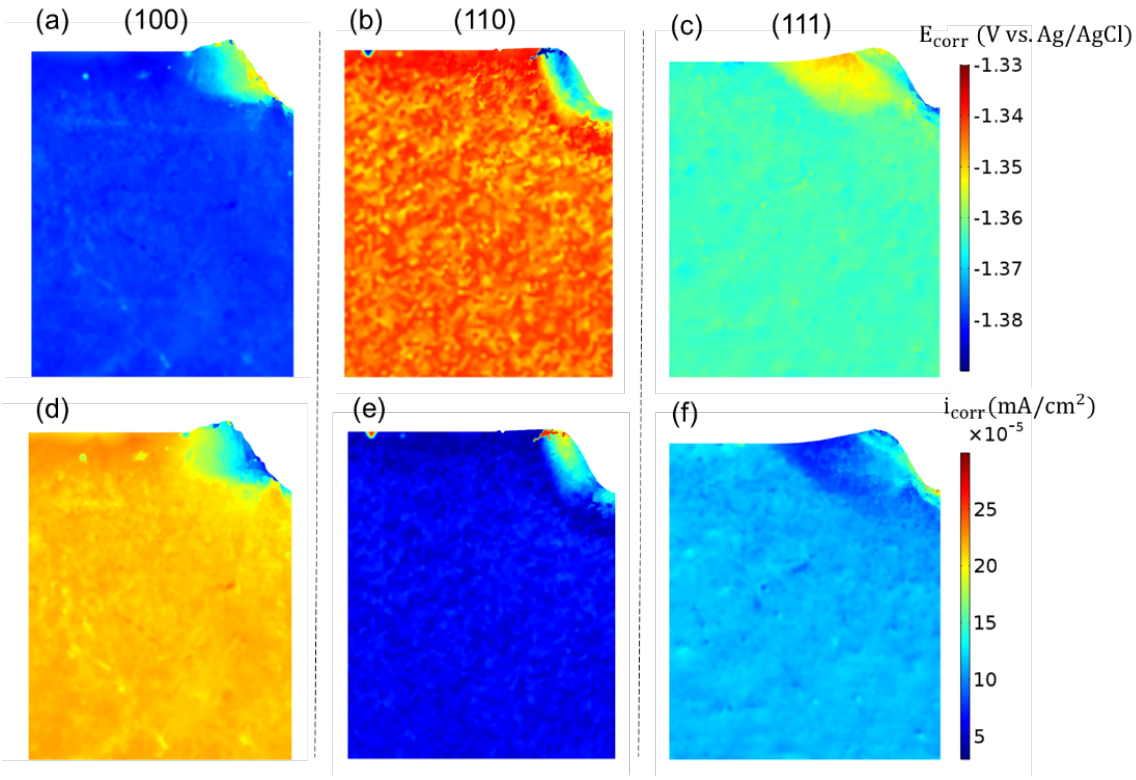

Figure 4.10 (a-c) Interpolated corrosion potential (Ecorr) and (d-f) corrosion current density (icorr) of tribocorroded surfaces of (100), (110), and (111) samples per corrosion maps developed in Figs. 9(b-c).

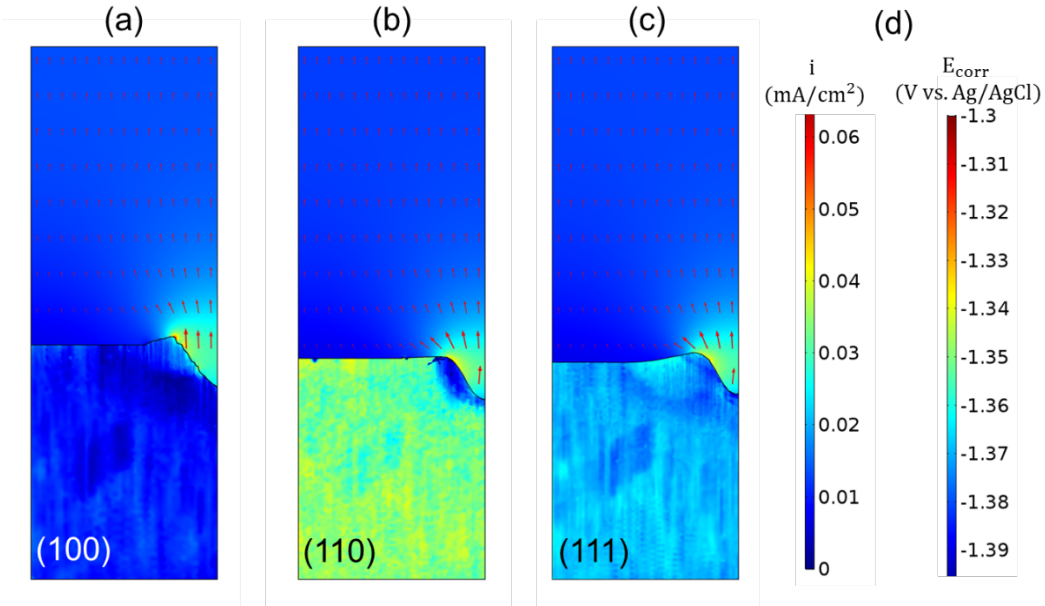

Figure 4.11 FE simulated current density within the electrolyte (i) and corrosion potential (Ecorr) distribution of (a) (100), (b) (110), and (c) (111) samples during tribocorrosion. The FE model considers both lattice reorientation and subsurface dislocation density effects per algorithms detailed in Section 3.1.

The simulated surface current distribution along the x-axis (TD) at time t_s corresponding to the state where the indenter has just depassivated the surface, is plotted in Fig. 12 to demonstrate the micro-galvanic coupling caused by the difference in crystal orientation and dislocation density. Three sets of current density are calculated with different effects included. **Fig. 4.12 (a)** is the result predicted by only including the crystallographic interpolated electrochemical parameters and the depassivation effect without considering the dislocation effect. Higher current density could be observed near the wear track. However, the current of (100) near the wear track is significantly lower than that of (110) and (111). This is because the lattice rotation caused by wear even raises the corrosion potential and lowers the corrosion current density near the wear track for (100) samples, which could be inferred from **Fig. 4.11**. Thus, even though the wear track is depassivated, the increase in local current density is small. While in the case of (110) and (111), both crystallographic effect and depassivation effect would increase the current density near the wear track. **Fig. 4.12 (b)** is the result is predicted by only including the dislocation effect without considering the crystallographic effect or the depassivation effect. (100) sample demonstrates more significant galvanic coupling caused by dislocation than the other two samples. **Fig. 4.12 (c)** considers all three effects. With all the effects considered, the three samples reach a similar overall current density level. The (100) sample shows more significant galvanic coupling inside the wear track, represented by the large fluctuation of the current density. For (100) and (110) samples, the highest current density is at the edge of the wear track.

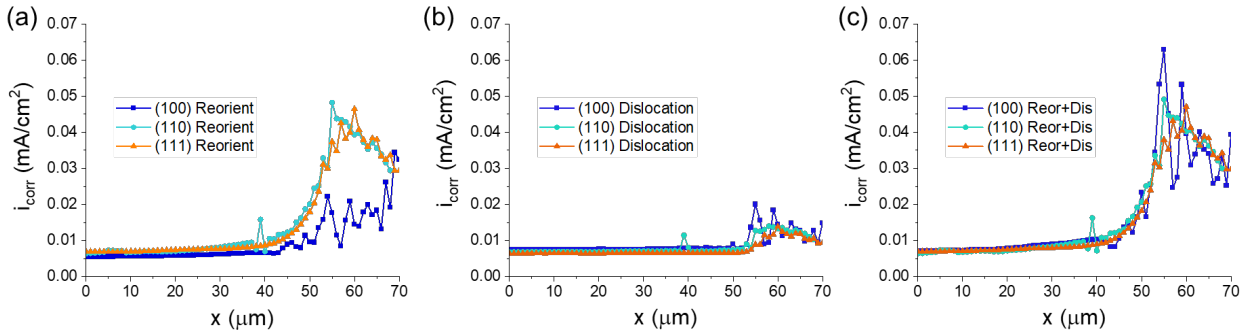

Figure 4.12 FE simulated current density distribution along the surface direction (defined in Fig. 2, where x=70 μm corresponds to the center of the wear track) during tribocorrosion considering (a) only lattice reorientation effect, (b) only dislocation effect, and (c) both lattice reorientation and subsurface dislocation effects.

To validate the effectiveness of the model with different assumptions, the total interface current during the tribocorrosion process was calculated using the integration method below. As shown in

Fig. 4.2, the total current of the wear track could be interpreted as the integration of the current at different place of the wear track. At time *t*, the indenter has been scratching for time $t - t_s$ and is thus at position $v(t - t_s)$ along the SD, where v is the velocity of the indenter. The wear track area right underneath the indenter is in a completely depassivated state while the starting point has been repassivated for time $t - t_s$. The area in between has a repassivation time which changes linearly from 0 to $t - t_s$. Thus, suppose the total interface current for the 2D simulation when repassvation has taken place for time *T* is *i*(*T*) (converted to the unit of nA/mm), the total current for the whole wear track when indenter has been moving for time T is

$$I(t) = \mathrm{v} \int_0^{t-\mathrm{t_s}} i(T)dT \tag{4.9}$$

After time *t* has passed t_f, the repassivation time along the wear track is a slow transition from $t - t_f$ at the end of the wear track to $t - t_s$ at the beginning of the wear track. Thus, the total current will be

$$I(t) = v \int_{t-t_f}^{t-t_s} i(T)dT \tag{4.10}$$

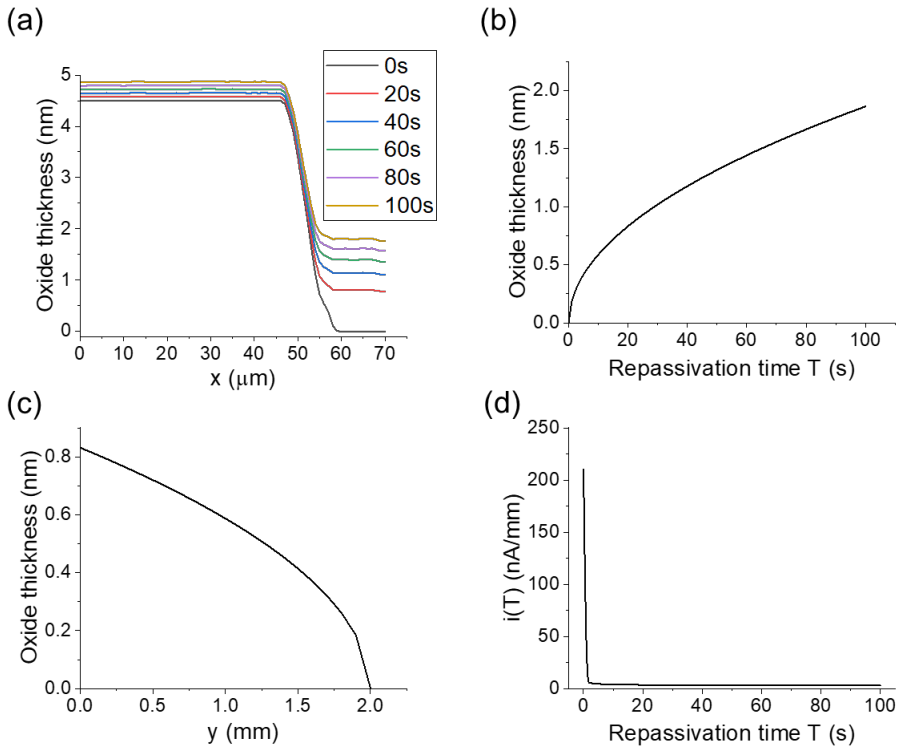

Figure 4.13 (a) Oxide thickness distribution along the x-axis (TD) of different time. (b) Oxide thickness at the bottom of the wear track with respect to repassivation time T. (c) Oxide thickness distribution along the y-axis (SD). (d) Current i(T) with respect to repassivation time T.

The result of the current density and oxide thickness of the (100) sample along the time domain is taken as an example to demonstrate how the total current is integrated in **Fig. 4.13**. As shown in **Fig 4.13 (a)**, the oxide thickness distribution along the x-axis (TD) will change as the surface repassivation. The repassivation rate inside the wear track is faster than that outside the wear track. The oxide thickness change at the bottom of the wear track with respect to repassivation time is plotted in **Fig 4.13 (b)**. Repassivation happens at a fast rate at the beginning and slows down as the oxide film growth thicker and the current density is reduced. At T=100s, the passive layer inside the wear track grows to a thickness of around 1.8 nm. This could be translated to an oxide thickness distribution along the y-axis (SD) as show in **Fig. 4.13 (c)**. At $t = t_f$, the end of the wear track is completely depassivated while the beginning of the wear track has an oxide thickness that has been repassivated for 20s. The 2D interface current $i(T)$ corresponding to repassivation time T is plotted in **Fig. 4.13 (d)** and the total current $I(t)$ is integrated using $i(T)$ based on eq (4.9) and (4.10).

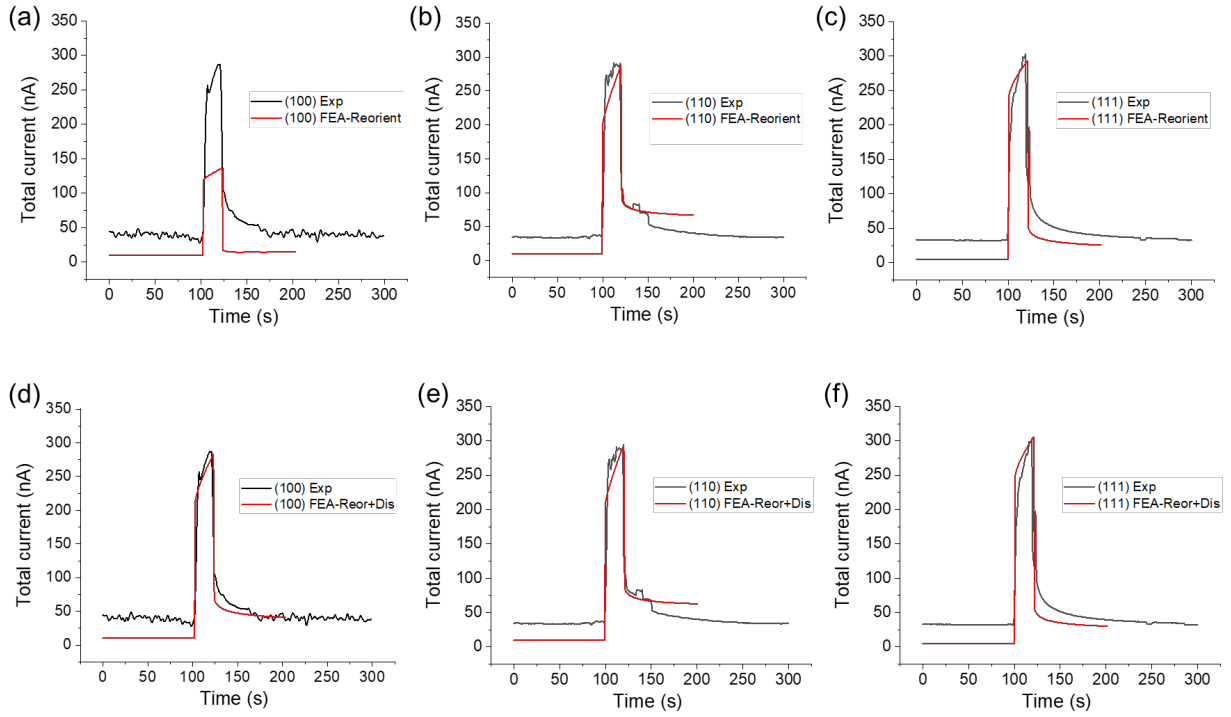

Figure 4.14 Comparison of experimental measured vs. FE simulated total tribocorrosion current for all samples by considering (a-c) only the lattice reorientation effect, and (d-f) both lattice reorientation and subsurface dislocation effects.

The total current predicted by only considering the crystallographic effect and depassivation effect is plotted in **Fig. 4.14 (a-c)**. The current predicted by simulation under this assumption is clear below the experimental current, especially for (100) sample. Even though the galvanic coupling between different orientations and depassivation cause the total current to increase during the tribocorrosion, the two effect is not enough to account for all the increase. Only after considering the dislocation effect, a good match between the simulation and experiment is achieved for the total tribocorrosion current, as shown in **Fig. 4.14 (d-f)**.

Just as discussed in experimental results, the tribocorrosion resistance of the three samples are similar, even though (100) has the lowest yield strength and the worst corrosion resistance. The simulation result could give a hint to this phenomenon. Comparing the current peak in **Fig. 4.14 (a)** and **Fig. 4.14 (d)**, the current considering only the crystallographic effect and the depassivation effect is much lower than that considering all the effects in the case of (100). This is much different from the cases of (110) and (111), in which crystal orientation and depassivation effect almost accounts for all the current increase. Just as discussed above, this is because as the crystal orientation inside the wear track changes from (100) to other orientations due to the lattice rotation caused by wear, the galvanic coupling between the wear track and unworn region in the case of (100) is reduced. While in the case of (110) and (111), the lattice rotation significantly makes the galvanic coupling more intense. This brings the tribocorrosion current of the (100) down to the same level as (110) and (111).

4.5 Conclusions

In this work, the crystallographic effect on tribocorrosion of pure Al was investigated using both experimental tests and FE simulations. The indentation test and potential-dynamic test confirmed the difference in mechanical and electrochemical properties for different crystal orientations. Based on the parameters interpolated from the results of (100), (110) and (111) surfaces obtained from these tests, a finite element model was developed using the crystallographic information obtained from EBSD test. The model included the depassivation-repassivation effect and the galvanic effect of difference in electrochemical properties caused by difference in crystal

orientation and the drop in equilibrium corrosion potential caused by dislocation density. The results from the experiments and simulation lead to the following conclusions:

(1) From experimental results, it could be indicated that the wear resistance and corrosion resistance of the (100) sample is the worst and (111) is the best. For hardness, (100) < (110) < (111). For open circuit potential, (100) < (110) < (111). For corrosion current density, (100) > (110) > (111).

(2) The simulation results match well with experimentally tested current curves, indicating that the depassivation-repassivation effect, crystallographic effect and dislocation effect all plays an important role in the localized, accelerated corrosion in the tribocorrosion process.

(3) However, both experiments and simulation results indicate that the three samples have similar current increase and peak current during the tribocorrosion test. This is because the crystallographic effect reduces the galvanic coupling between the worn region and unworn region for (100) sample, while increasing the galvanic coupling in the case of (110) and (111).

The success in this single crystal tribocorrosion model has great significance in helping to explain the underlying mechanism of tribocorrosion. It could be adapted to simulate other material systems or act as a first step to build models with more complex microstructures.

References

1. Vieira, A.C., et al., *Mechanical and electrochemical deterioration mechanisms in the tribocorrosion of Al alloys in NaCl and in NaNO3 solutions.* Corrosion Science, 2012. **54**: p. 26-35.
2. Mraied, H. and W.J. Cai, *The effects of Mn concentration on the tribocorrosion resistance of Al-Mn alloys.* Wear, 2017. **380-381**: p. 191-202.
3. Chen, J., et al., * Effects of alloying concentration on the aqueous corrosion and passivation of aluminum-manganese-molybdenum concentrated alloys .* Corrosion Science, 2022. **198**.
4. Wen, F., et al., *Effect of crystal orientations and precipitates on the corrosion behavior of the Al-Cu alloy using single crystals.* Journal of Alloys and Compounds, 2022. **890**.

5. Ralston, K.D., et al., *The effect of precipitate size on the yield strength-pitting corrosion correlation in Al-Cu-Mg alloys.* Acta Materialia, 2010. **58**(18): p. 5941-5948.
6. Zhu, Y.K., et al., *Localized corrosion at nm-scale hardening precipitates in Al-Cu-Li alloys.* Acta Materialia, 2020. **189**: p. 204-213.
7. Macdonald, D.D., *Passivity - the key to our metals-based civilization.* Pure and Applied Chemistry, 1999. **71**(6): p. 951-978.
8. Mraied, H., W.J. Cai, and A.A. Sagues, *Corrosion resistance of Al and Al-Mn thin films.* Thin Solid Films, 2016. **615**: p. 391-401.
9. Mischler, S., S. Debaud, and D. Landolt, *Wear-accelerated corrosion of passive metals in tribocorrosion systems.* Journal of the Electrochemical Society, 1998. **145**(3): p. 750-758.
10. Mischler, S., A. Spiegel, and D. Landolt, *The role of passive oxide films on the degradation of steel in tribocorrosion systems.* Wear, 1999. **225**: p. 1078-1087.
11. Landolt, D., S. Mischler, and M. Stemp, *Electrochemical methods in tribocorrosion: a critical appraisal.* Electrochimica Acta, 2001. **46**(24-25): p. 3913-3929.
12. Wang, W.B., et al., *Ultrahigh tribocorrosion resistance of metals enabled by nano-layering.* Acta Materialia, 2021. **206**.
13. Wang, K.W., et al., *Multiphysics modeling and uncertainty quantification of tribocorrosion in aluminum alloys.* Corrosion Science, 2021. **178**.
14. Papageorgiou, N. and S. Mischler, *Electrochemical Simulation of the Current and Potential Response in Sliding Tribocorrosion.* Tribology Letters, 2012. **48**(3): p. 271-283.
15. Cao, S.F., S.G. Maldonado, and S. Mischler, *Tribocorrosion of passive metals in the mixed lubrication regime: theoretical model and application to metal-on-metal artificial hip joints.* Wear, 2015. **324**: p. 55-63.
16. Chen, J., et al., *The origin of passivity in aluminum-manganese solid solutions.* Corrosion Science, 2020. **173**.
17. Li, Z.Y., H.Y. Yu, and D.B. Sun, *The tribocorrosion mechanism of aluminum alloy 7075-T6 in the deep ocean.* Corrosion Science, 2021. **183**.
18. Chen, X., et al., *Emergence of micro-galvanic corrosion in plastically deformed austenitic stainless steels.* Materials & Design, 2021. **203**.
19. Jemmely, P., S. Mischler, and D. Landolt, *Electrochemical modeling of passivation phenomena in tribocorrosion.* Wear, 2000. **237**(1): p. 63-76.

20. Olsson, C.O.A., et al., *Modeling Current Transients in a Reciprocal Motion Tribocorrosion Experiment.* Journal of the Electrochemical Society, 2021. **168**(3).
21. Cao, S.F. and S. Mischler, *Modeling tribocorrosion of passive metals - A review.* Current Opinion in Solid State & Materials Science, 2018. **22**(4): p. 127-141.
22. Cheng, Y.F., *Stress corrosion cracking of pipelines*. 2013: John Wiley & Sons.
23. Gutman, E.m.M., *Mechanochemistry of solid surfaces*. 1994, Singapore ; River Edge, NJ: World Scientific. ix, 322 p.
24. Xu, L.Y. and F. Cheng, *A finite element based model for prediction of corrosion defect growth on pipelines.* International Journal of Pressure Vessels and Piping, 2017. **153**: p. 70-79.
25. Zhu, Z., et al., *Numerical Simulation and Experimental Verification of Pitting Corrosion Propagation in Sweet Pipeline Service.* Journal of Pipeline Science and Engineering, 2022.
26. Shahryari, A., J.A. Szpunar, and S. Orrianovic, *The influence of crystallographic orientation distribution on 316LVM stainless steel pitting behavior.* Corrosion Science, 2009. **51**(3): p. 677-682.
27. Hagihara, K., et al., *Crystal-orientation-dependent corrosion behaviour of single crystals of a pure Mg and Mg-Al and Mg-Cu solid solutions.* Corrosion Science, 2016. **109**: p. 68-85.
28. Song, G.L. and Z.Q. Xu, *Crystal orientation and electrochemical corrosion of polycrystalline Mg.* Corrosion Science, 2012. **63**: p. 100-112.
29. Song, J.M., et al., *Orientation dependence of the electrochemical corrosion properties of electrodeposited Cu foils.* Corrosion Science, 2013. **74**: p. 223-231.
30. Komanduri, R., N. Chandrasekaran, and L.M. Raff, *MD simulation of indentation and scratching of single crystal aluminum.* Wear, 2000. **240**(1-2): p. 113-143.
31. Komanduri, R., N. Chandrasekaran, and L.M. Raff, *MD Simulation of nanometric cutting of single crystal aluminum-effect of crystal orientation and direction of cutting.* Wear, 2000. **242**(1-2): p. 60-88.
32. Liu, M., et al., *A combined experimental-numerical approach for determining mechanical properties of aluminum subjects to nanoindentation.* Scientific Reports, 2015. **5**.
33. Yasuda, M., F. Weinberg, and D. Tromans, *Pitting Corrosion of Al and Al-Cu Single-Crystals.* Journal of the Electrochemical Society, 1990. **137**(12): p. 3708-3715.

34. Treacy, G.M. and C.B. Breslin, *Electrochemical studies on single-crystal aluminium surfaces.* Electrochimica Acta, 1998. **43**(12-13): p. 1715-1720.
35. Davis, B.W., P.J. Moran, and P.M. Natishan, *Metastable pitting behavior of aluminum single crystals.* Corrosion Science, 2000. **42**(12): p. 2187-2192.
36. Bland, L.G., K. Gusieva, and J.R. Scully, *Effect of Crystallographic Orientation on the Corrosion of Magnesium: Comparison of Film Forming and Bare Crystal Facets using Electrochemical Impedance and Raman Spectroscopy.* Electrochimica Acta, 2017. **227**: p. 136-151.
37. Barrett, T.J., et al., *A generalized spherical harmonics-based procedure for the interpolation of partial datasets of orientation distributions to enable crystal mechanics-based simulations.* Materialia, 2019. **6**: p. 100328.
38. Hielscher, R. and H. Schaeben, *A novel pole figure inversion method: specification of the MTEX algorithm.* Journal of Applied Crystallography, 2008. **41**: p. 1024-1037.
39. Pantleon, W., *Resolving the geometrically necessary dislocation content by conventional electron backscattering diffraction.* Scripta Materialia, 2008. **58**(11): p. 994-997.
40. Nye, J.F., *Some Geometrical Relations in Dislocated Crystals.* Acta Metallurgica, 1953. **1**(2): p. 153-162.
41. Natishan, P.M. and W.E. O'Grady, *Chloride Ion Interactions with Oxide-Covered Aluminum Leading to Pitting Corrosion: A Review.* Journal of the Electrochemical Society, 2014. **161**(9): p. C421-C432.
42. Li, Z., et al., *Investigation of the stress corrosion cracking behavior in annealed 5083 aluminum alloy sheets with different texture types.* Journal of Alloys and Compounds, 2020. **817**.
43. Shi, Y.Q. and I. Szlufarska, *Wear-induced microstructural evolution of nanocrystalline aluminum and the role of zirconium dopants.* Acta Materialia, 2020. **200**: p. 432-441.

Chapter 5. Summary and Future Work

5.1 Summary of the thesis

In this thesis, finite element method was exploited to investigate the mechanism of tribocorrosion of Al, Al-Mn alloys and Al/Cu multilayers. Models that couple electrochemistry with material mechanics and microstructures were built to investigate the mechanism of tribocorrosion.

In study 1, the tribocorrosion of bulk Al alloy was simulated with the consideration of abrasive wear, depassivation/repassivation effect and the coupling of electrochemical kinetics with plastic strain. The model reflects how depassivation and mechanical deformation affect the electrochemical status of alloy, causing accelerated localized corrosion. The model was then used to investigate how Young's modulus, yield strength, exchange current density, and Tafel slopes affect the tribocorrosion resistance of bulk materials, which was summarized by a material loss map to guide the optimization of the tribocorrosion performance of alloys.

In study 2, the tribocorrosion of Al/Cu multilayers was simulated focusing on the micro-galvanic corrosion between the layers. The model demonstrated Cu being the nobler metal in the galvanic couple and the passivity of Al is the reason of the improved tribocorrosion resistance of this structural material. It also predicted that thinner layer thickness (within the range of 10~100 nm) leads to enhanced wear and tribocorrosion resistance, which is coherent with experimental results.

In study 3, EBSD were exploited in combination with FE simulation to investigate the effect of crystal orientation on wear, corrosion and tribocorrosion properties of pure Al. Experimental results demonstrate that in terms of pure wear and pure corrosion resistance, the ranking is (100) < (110) < (111). But samples with different crystal orientation was found to have little difference in tribocorrosion performance by both experiment and simulation. The simulation also demonstrated how crystallographic effect and dislocation density effect causes micro-galvanic corrosion in the vicinity of the wear track and leads to accelerated localized corrosion.

The FE models built in the three studies provide insights into the cause of the tribocorrosion of Al and its alloys and multilayers. Furthermore, the model facilitate optimization of the tribocorrosion performance of Al with numerical modeling method, providing guidance to future material design.

5.2 Proposed future work

Based on the current results in this dissertation, three future research works are proposed in order to build a more powerful model with more thorough fundamental understanding of the tribocorrosion, and to optimize the corrosion and tribocorrosion resistance of metals such as Al-Mn alloys.

(1) Molecular dynamics (MD) or density functional theory (DFT) could be used to predict the mechanical and corrosion properties of materials instead of nanoindentation test and potential-dynamic test. The combination of MD and the developed FE model could predict material's tribocorrosion performance prior to the synthesis of the material.

(2) Crystal Plasticity Finite Element Modeling (CPFEM) could assist the simulation of crystal orientation change during the tribocorrosion process. With proper experimental validation and calibration, CPFEM could predict lattice rotation and dislocation density, replacing the role of EBSD characterization in providing input of the tribocorrosion model.

(3) Experimental research could be carried out on Al-Mn alloys according to the prediction of Study 1. Emphasis should be put on finding out the optimal composition to synthesize alloys with low anodic and cathodic exchange current density, low anodic Tafel slope, high yield strength, and low Young's modulus in order to improve their corrosion and tribocorrosion resistance. Wear, electrochemical and tribocorrosion test could be carried out to verify the prediction of the model.

Appendix A: Experimentally Validated Finite Element Modeling of Electrochemical Polishing of Niobium in Hydrofluoric-Sulfuric Acid Electrolyte

This chapter is based on the following published paper in in Journal of The Electrochemical Society and reprinted with permission.

K. Wang, W. Cai, H. Tian and C. Reece "Finite Element Modeling of Electrochemical Polishing of Niobium in Hydrofluoric-Sulfuric Acid Electrolyte", Corrosion Science 178, 109095 (2021)

https://doi.org/10.1149/1945-7111/ac7354

A.1. Introduction

Superconducting radio-frequency (SRF) cavities are critical components for particle accelerators, which exploit high resonant electric fields to accelerate charged particles [1]. To achieve desired accelerating performance, niobium (Nb) SRF cavities require microscopically smooth internal surface at the grain level since the SRF current flows in the outmost ~ 40 nm of the surface [2]. Traditional chemical etching fails at producing grain-level smoothness due to the differences of etching rate at grain interior vs. grain boundaries, as well as grains with different crystallographic orientation. For example, buffered chemical polishing treatments of Nb result in a typical root mean square surface roughness of about 1.6 ± 0.42 μm [3]. Electrochemical polishing, on the other hand, overcomes such limitations by controlling metal dissolution rate at the limiting current range so that a uniform surface can be achieved [4]. When metals dissolves at the limiting current density, the dissolving metal (e.g. Nb) surface is typically covered by a thin compact solid film consisting of an oxide (e.g. Nb_2O_5), perhaps contaminated with significant amounts of anion from the electrolyte, as shown by previous surface characterizations [5, 6]. If the ionic conductivity of the film is sufficient to allow for the passage of the anodically formed cations at high rate, the dissolution/removal of atoms from the metal into the solid film would then occur with no dependence on local polarization potential, producing a smooth surface regardless of the microstructure (e.g. crystallographic orientation and grain boundaries) of the metal, since it is

governed by the availability of cation vacancies in the film and not by the lattice position of the metal atoms [4, 7-9].

Past experimental studies show that electrochemical polishing of Nb SRF cavity surface (**Fig. A1(a)**) using an electrolyte of concentrated sulfuric acid (98%) and hydrofluoric acid (49%) by a volume ratio of 10:1 result in smooth Nb surfaces [4, 9]. While many studies [9-11] utilize acidic fluoride electrolyte since HF is effective in dissolving the anodic films on Nb, those using fluoride-free electrolyte has also been reported [8, 12, 13]. Studies investigating the mechanisms and kinetics of the electrochemical reactions during the electrochemical polishing of the Nb has been conducted by several groups, such as Guan et al. [14] and Hryniewicz et al. [15]. X-ray photoelectron spectroscopy (XPS) confirmed the existence of the intermediate state of Nb_2O_5 and NbF_5. The mechanism involving the formation of Nb_2O_5 by anodic polarization and dissolution of the oxide layer under the influence of HF is also confirmed by electrochemical impedance spectroscopy (EIS) study [16]. Based on these results, the electrochemical polishing process of the Nb could be separated into two steps, as shown schematically in **Fig. A1(b)**. Firstly, the applied potential drives the Nb to anodize and form a thin oxide layer of niobium pentoxide (Nb_2O_5), which could be expressed by the reaction:

$$2Nb + 5H_2O \rightarrow Nb_2O_5 + 10H^+ + 10e^-, \quad (1)$$

while at the same time, the hydrogen evolution reaction happens at the Al surface of the counter electrode:

$$2H^+ + 2e^- \rightarrow H_2. \quad (2)$$

The second part of the process involves the dissolution of the niobium pentoxide at the electrode-electrolyte interface due to the synergistic effect of H^+ and F^-ions:

$$Nb_2O_5 + 10H^+ + 10F^- \rightarrow 2NbF_5 + 5H_2O. \quad (3)$$

The NbF_5 converts to a dissolvable state of $[NbF_7]^-$ in the presence of hydrofluoric acid (HF). The thickness of the Nb_2O_5 layer is determined by the formation of Nb_2O_5 which is affected by the applied potential and the dissolution of the Nb_2O_5. With higher applied potential, the oxidation rate will increase while the dissolution rate of the Nb_2O_5 has an upper limit due to the diffusion-limited mass transport control of fluorine ions. This results in thicker Nb_2O_5 layer, which reduces the electropolishing current and slows down the oxidation rate, which will eventually become the same as the dissolution rate. The thickness of the Nb_2O_5 layer and the current density is then stabled at a steady state. A voltage range exists within which, the increase in applied voltage does not

increase the current density so that the electrochemical polishing proceeds in a controlled rate, which is referred to as the plateau region [17, 18]. Once the overpotential on the cavity is maintained in the plateau region to allow the generation of stable and uniform current, the reaction rate can be tailored by the solution temperature to balance the Nb oxidization and Nb_2O_5 dissolution [11, 14].

Despite the understanding of the general mechanism, a quantitative and comprehensive understanding of the relationship between the processing parameters and the electrochemistry of the SRF cavity is still lacking. The challenge lies in the fact that there are several factors acting synergistically and impeding the uniform metal dissolution and oxidation over increasingly complicated geometries. Firstly, due to the difference in distance between the cathode and anode caused by the geometry of the cavity, the secondary current distribution is non-uniform and difficult to measure and control experimentally. Secondly, Joule heating induced during electrochemical polishing process will alter the temperature in the electrolyte, affect the kinetic parameters of the reactions, and ultimately lead to high ionic diffusion rate and local tertiary current density [11]. The variance in both secondary and tertiary current significantly complicates the problem. This will result in poor polishing result due to the formation of pits and porous oxide [11], as well as the generation of bubbles produced during reactions, all of which impede local ionic diffusion to cause non-uniform electrochemical polishing in microscale [19]. In addition, high dissolution rate caused by high temperature will cause the protecting oxide layer to completely dissolve, exposing the Nb surface directly to the acidic environment, leading to etching instead of uniform electrochemical polishing to the metal surface [9]. Lastly, the non-uniform temperature distribution will also affect the uniformness of the current distribution in macroscale, compromising the polishing results [20].

To address the above challenges and complexity during electrochemical polishing of Nb cavities, this work aims to develop a numerical modeling framework that couples the complex cavity geometry, and the multiphysics nature of the electrochemical polishing process, which includes the electrochemical reactions, thermal effects and fluid flow of the electrolyte and coolant, to systematically investigate the synergistic effects of electrochemical polishing conditions and cavity geometry on the metal dissolution kinetics. While several work has been done in the past using the finite element (FE) method to study the separate effects of fluid dynamics [21] or cavity geometry [22], little work has been done to evaluate their synergistical effects using experimental

results as validations. In this project, a multiphysics FE model was developed to quantitatively simulate the electropolishing kinetics using simple coupon geometry and was validated by the potentiodynamic curve collected by experiment using coupon samples. The electropolishing kinetics were further applied to a C100 1-cell cavity geometry (as shown in **Fig. A1(a)**). The current distribution, temperature and oxide thickness distribution along the cavity surface was simulated. Using this model, the effects of coolant flow and temperature on the surface current and oxide thickness was studied. The model paves the way for further investigation of electrochemical polishing of new cavity geometry (for example, the RFD crab cavity [23]) and the design for cooling systems that could greatly expedite future accelerator design and manufacture.

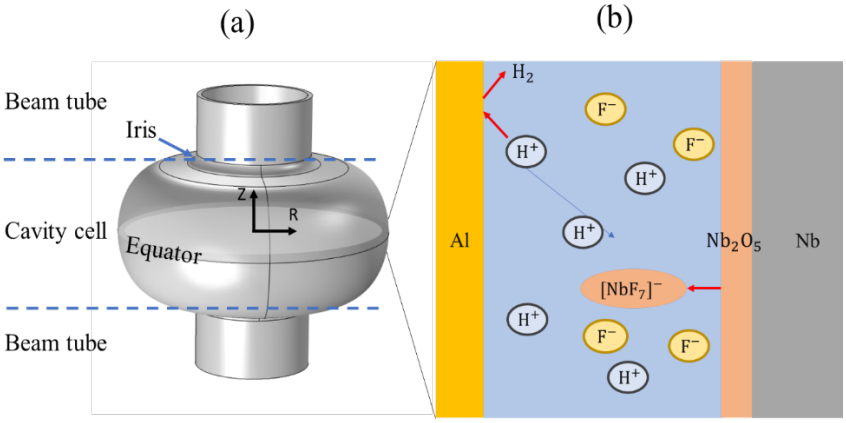

Figure A1 Schematic of the (a) 3D geometry of the C100 Nb cavity, and (b) electrochemical mechanisms during EP of Nb in hydrofluoric-sulfuric acid electrolyte.

A.2. Experimental and Modeling Methods

A.2.1. Experimental Methods

Electrochemical tests were conducted using standard 3-electrode setup, with the rectangular coupon of Nb with 0.6 cm^2 exposed area used as the working electrode (WE), Al plate as the counter electrode (CE), and mercury/mercury sulfate standard electrode as the reference electrode (RE). The electrolytes were a mixture of analytic grade 49% hydrofluoric acid and 96% sulfuric acid with volume ratio of 1:10, which is the same electrolyte used in electrochemical polishing. Potentiodynamic polarization curves of Nb were measured by a potentiostat (Gamry, PA, USA) with a potential ranging from -1 V to 1 V with respect to the RE from 10 – 45 °C. The electrochemical parameters reflecting the kinetics of the cell, including equilibrium potential,

corrosion current density and transfer coefficient was obtained from the potentiodynamic curve. The plateau current density is also measured as a function of the temperature. The test was run with static electrolyte with any stirring and the system was kept in a water bath to control the temperature.

A.2.2. Finite Element Models

COMSOL Multiphysics (version 5.3) was used for the FE models, with simulation and validation steps as shown in **Fig. A2**. The built-in fully coupled solver with automatic highly non-linear Newton iteration method was applied for the simulations. The minimum damping factor is set to be 10^{-6} and a relative tolerance of 0.001 is given for the solver. Triangular shaped meshes are applied throughout the model, as shown in **Fig. A3 (c, d)**. A coupon model with simple geometry were first simulated to investigate and validate the proposed electrochemical mechanism of the electrochemical polishing process. The potentiodynamic curve was simulated by the coupon model and compared to that obtained from experiment to validate the i-V relationship. Then the electrochemical setup was applied to a model using the C100 cavity geometry with added effects of temperature and coolant flow.

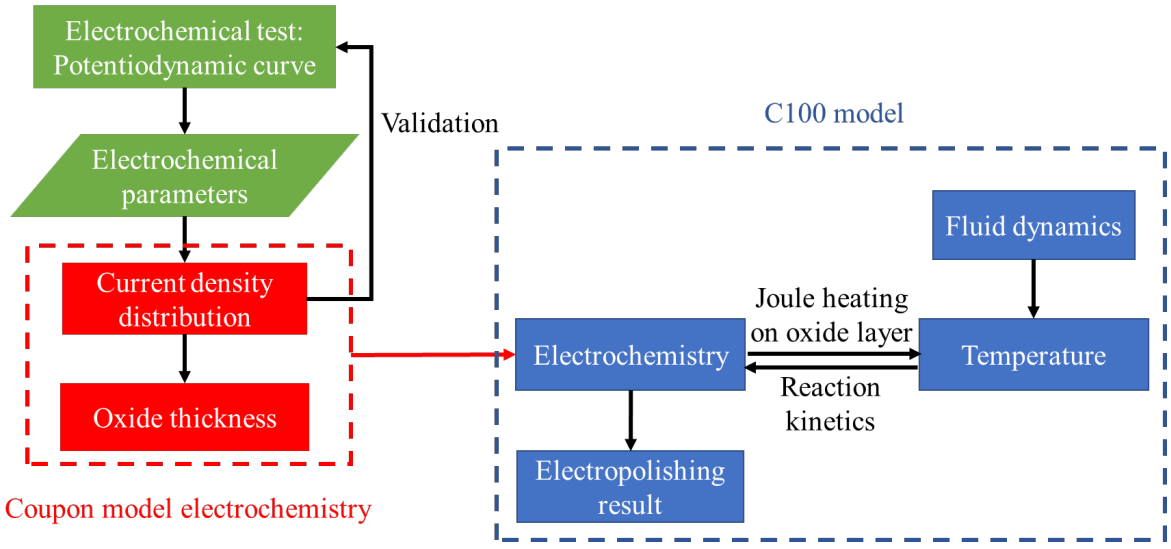

Figure A2 Flowchart of the developed FE modeling and experimental validation schemes.

(i) Coupon model geometry

The coupon sample model simulated the scenario where two flat rectangular electrodes of Nb (anode) and Al (cathode) were placed in parallel to each other in the electrolyte, as shown in **Fig. A3(a)**. To avoid the complexity of the convergence problem caused by the edge effect and focus only on the surface kinetics, the geometry was simplified as two parallel surfaces with the rectangular-shaped electrolyte of 5 × 10 cm^2 between them. The right boundary of the rectangle is the Nb sample surface, which is assigned with the Butler-Volmer kinetics, faradaic oxide growth and non-faradaic dissolution as described in the next section. The left boundary is the Al counter electrode surface with the Butler-Volmer kinetics to reflect the hydrogen evolution reaction. The meshing size of the coupon model is 5 mm.

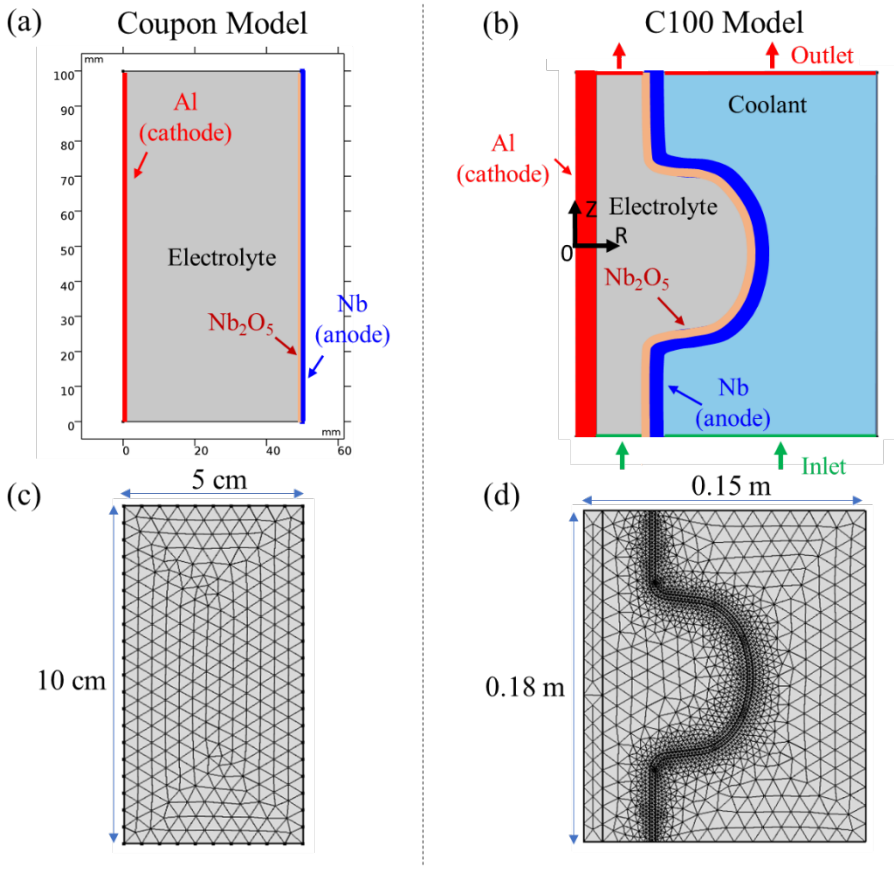

Figure A3 (a-b) FE model setup schematics and (c-d) meshing plot for the coupon and C100 models.

(ii) Coupon model governing equations

The reaction kinetics of the oxidization of Nb in the low voltage region is given by the Butler-Volmer equation:

$$i_{B-V} = i_0 \left(\exp\left(\frac{\alpha_a F \eta}{RT}\right) - \exp\left(\frac{\alpha_c F \eta}{RT}\right) \right), \quad (4)$$

where i_0 stands for the equilibrium corrosion current density, α_a and α_c stands for the anodic and cathodic transfer coefficient respectively, and η stands for the overpotential. The overpotential η is defined as

$$\eta = \varphi_{app} - \varphi_l - \varphi_{film} - \varphi_{eq}, \tag{5}$$

in which φ_{app} is the externally applied potential, φ_l is the electrolyte potential at the interface, φ_{film} is the potential drop from the metal (hydr)oxide layer, and φ_{eq} is the equilibrium corrosion potential. When the overpotential is much higher or lower than 0, the Butler-Volmer equation could be approximately simplified to Tafel equation. The transfer coefficient α could be correlated with the Tafel slope β by equation

$$\alpha = \frac{2.303RT}{F\beta}. \tag{6}$$

To simulate the circumstance when the applied potential drives the system to the plateau region, the equation is implemented to calculate the local corrosion current density:

$$i_{loc} = \frac{i_{B-V}}{1+\frac{i_{B-V}}{i_{lim}}}, \tag{7}$$

where i_{lim} is the limiting current density. This eq. (7) ensures the smooth transition of the potentiodynamic curve from Butler-Volmer region to plateau region. At the Butler-Volmer region where $i_{B-V} \ll i_{lim}$, it is assumed that $i_{loc} \approx i_{B-V}$. At the plateau region where $i_{B-V} \gg i_{lim}$, it is assumed that $i_{loc} \approx i_{lim}$. Here the i_{lim} is assumed to be the same as the temperature-dependent plateau current density as measured by experiment, which is listed in **Table A1**.

Table A1 Summary of limiting current density under different temperatures (T) measured by potentiodynamic polarization tests.

T (°C)	i_{lim} (mA/cm^2)
10	8.37
15	10.13
20	15.32
22	16.26
26	18.15
34	20.64
45	40.01

The growth rate of oxide per reaction (1) is implemented by the following equation

$$v_F = \frac{\nu i_{loc} M}{nF\rho}, \quad (8)$$

where v_F is the growth rate expressed in thickness/time, ν is the stoichiometric coefficient, which is 1, i_{loc} is the current density calculated using equation (7), M is the molar mass of the niobium pentoxide, which is 0.26581 kg/mol, n is the electron transferred during the reaction, which is 5, F is the Faraday's constant, and ρ is the density of the niobium pentoxide, which is 4550 kg/m^3.

Apart from the Faradaic oxide growth described above, the oxide dissolution reaction expressed by reaction (3) happens in a non-Faradaic manner. Such reaction does not induce electron transport between the Nb anode and Al cathode and thus does not contribute to the overall current density. The rate of this reaction is determined by the concentration of H^+ and F^- that could reach the surface of the Nb_2O_5. Compared to the F^- ions, H^+ ions has a much higher concentration in this acidic electrolyte composed of the mixture of HF and H_2SO_4, so the main rate limiting factor of this reaction is the diffusion of F^- ions [24]. The non-faradaic dissolution rate v_{NF} is given by

$$v_{NF} = (DMc_{F^-})/(\rho\delta), \quad (9)$$

where D is the temperature-dependent diffusion coefficient of F^- ions as listed in **Table A2** [17], c_{F^-} is the concentration of F^- ions and δ is the thickness of the diffusion layer. In our study, a concentration gradient of 25,701,254 mol/m^4 is used as a replacement of the c_{F^-}/δ term, obtained based on the result from [17].

Table A2 Summary of diffusion coefficient of F- ions under different temperatures (T) interpolated from the experimental data from Ref [17].

T (°C)	D ($\times 10^{-12}$ m^2/s)
1	2.69
9	4.86
19	8.77
30	12.9
41	28.3
50	29.0

Thus, the total growth rate (v_n) of the oxide is then given by

$$v_n = v_F - v_{NF} = \frac{\nu i_{loc} M}{nF\rho} - v_{NF}. \quad (10)$$

By integrating the growth rate with respect to time, the thickness of the Nb_2O_5, as well as the resistance of the oxide could be obtained as

$$r_{film} = \frac{\int v_n dt}{\sigma}, \tag{11}$$

where σ is the electrical conductivity of niobium pentoxide, which is 1.46×10^{-6} S/m [25, 26]. The φ_{film} defined in eq. (5) is then calculated from r_{film} along the cavity surface using Ohmic law

$$\varphi_{film} = i_{loc} r_{film} \tag{12}$$

(iii) C100 model geometry

A 2D axisymmetric model was built for the C100 cavity, as shown in **Fig.** A**3(b)**. The wall thickness of the Nb cavity is 3 mm. The counter electrode is an aluminum rod. The internal of the cavity is filled with electrolyte, while the outside by the coolant (i.e. water). The diameter of the chamber for outside water cooling is 0.15 m, giving an inlet area of 0.0661 m^2. The size of the inlet for inside electrolyte flow is 0.00353 m^2. The meshing of the C100 model is finer near the Nb surfaces than elsewhere so that the potential, current density and temperature distribution have larger gradient near the boundary of the Nb cavity. The meshing size near and inside the cavity wall is set to be 2 mm and slowly transitions to 10 mm in regions far from the wall, as plotted in **Fig. A3(d)**.

Table A3 Summary of the electrochemical kinetic parameters of Nb used in the FE simulations, where α, φ_{oc}, and i_0 represents the transfer coefficient, equilibrium corrosion potential, and equilibrium corrosion current density respectively, as defined in section 2.2.

	α	φ_{eq} (V vs. Hg/Hg_2SO_4)	i_0 (mA/cm^2)
Cathodic	-0.568	- 0.823	4.61×10^{-2}
Anodic	0.644		

(iv) C100 model governing equations

The electrochemical kinetics for C100 model was set up the same as the coupon model. The coupling of temperature with faradaic oxidization was implemented by the temperature-dependent

limiting current density $i_{lim}(T)$, interpolated from the experimental data as listed in **Table A1**, while the non-faradaic dissolution rate was calculated based on the temperature-dependent diffusion coefficient of F^- ions in the electrolyte, interpolated from the experimental data as listed in **Table A2** [17].

The inlet and the outlet of the coolant flow direction is shown in **Fig. A3(b)**. The electrolyte flows into the cavity while the outside is filled with cooling water flow. Both the inside and the outside flows are given laminar flow conditions and are set to be fully developed flow. The boundary condition of the fluid is set as no slip, meaning that fluid velocity at the wall is 0. The boundary condition of the inlet of the inside electrolyte flow is given by a total flow rate of 1 gallon/min. For outside water coolant, three coolant flow rates, 1, 10 and 100 gallon/min (GPM), were chosen to represent a mild, average, and aggressive coolant flow strategy.

The general heat transfer is governed by the equation

$$\rho C_p \frac{\partial T}{\partial t} + \rho C_p u \cdot \nabla T + \nabla \cdot (k \nabla T) = Q, \tag{6.13}$$

where ρ is the density of the material or liquid, C_p is the heat capacity at constant pressure, T is the temperature, t is the time, k is the thermal conductivity, and Q is the heat source power per unit area, given by Joule heating of the oxide layer as

$$Q = {i_{loc}}^2 r_{film}. \tag{6.14}$$

Because the conductivity of the Nb, Al metal and the electrolyte is much larger than that of the niobium pentoxide, thus, Joule heat generated by similar current flowing through them is negligible comparing to that of the niobium pentoxide and not considered in this model.

The outside boundary of the system is set to be an open boundary for heat transfer.

A.3. Results and discussions

A.3.1. Potentiodynamic polarization behavior of Nb

The experimentally measured potentiodynamic polarization curve of Nb in hydrofluoric-sulfuric acid electrolyte at 20°C is plotted in **Fig. A4(a)**. The curve could be separated into a Butler-Volmer region at low potentials (~ -1.25 V to -0.5 V vs. Hg/Hg_2SO_4) and a plateau region at high potentials (~ -0.5 V to 1.0 V vs. Hg/Hg_2SO_4). It can be seen that the equilibrium corrosion potential

is ~ -0.823 V vs. Hg/Hg_2SO_4. The transfer coefficient of the anodic and cathodic branches listed in **Table A3** were calculated from eq. (6) using the anodic and cathodic Tafel slopes obtained by linear fitting of the curves within ± 200 mV of the open circuit potential, as denoted by the blue and red solid lines respectively in **Fig. A4(a)**. The equilibrium corrosion potential and current density was determined at the intersection of the two Tafel lines. The obtained parameters are also listed in **Table A2** and used for the FE simulations. The limiting current density (i_{lim}) is obtained from the plateau region by the average value of the current density at 0 V, 0.5 V and 1 V. The limiting current density was measured for different temperatures and the result is listed in **Table A1**. The temperature deviation during the measurement of the potentiodynamic curve is kept below 1.5 °C for each data point. It can be seen from **Fig. A4(b)** that the limiting current density increased monotonically with temperature, from ~ 8.4 mA/cm^2 at 10 °C to ~ 40 mA/cm^2 at 45 °C, similar to the trend reported by Jin et al. [27].

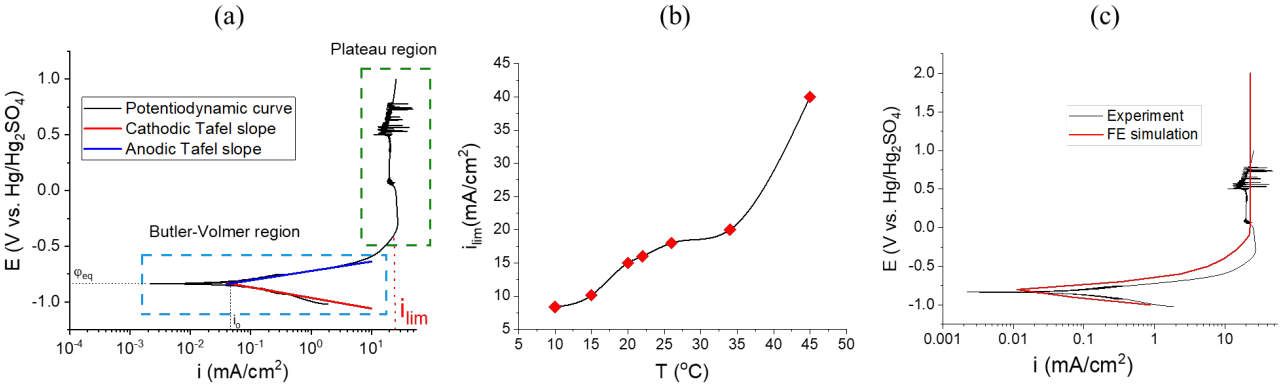

Figure A4 (a) Potentiodynamic polarization curve of Nb measured in hydrofluoric-sulfuric acid electrolyte at 20°C. (b) Summary of the experimentally measured limiting current density as a function of temperature. (c) Simulated and experimentally measured potentiodynamic polarization curves of Nb in hydrofluoric-sulfuric acid electrolyte at 20°C.

A.3.2. Coupon model validation

The experimentally measured electrochemical kinetic parameters listed in **Table A2** were used as inputs for the FE coupon model. A potentiodynamic polarization curve was then simulated by the coupon model using the governing equations described in section 2.2, as shown in **Fig. A4(c)**. For the simulation, after applying different potentials, the average current density flow through the surface were calculated using the model. **Fig. A4(c)** shows that the simulated curve successfully

captured the shape of the potentiodynamic curve at the Bulter-Volmer region and the plateau region, demonstrating the validity of the electrochemical kinetics setup. The same electrochemical kinetics is then applied to the C100 model.

A.3.3. Electrochemcial behavior of C100 Nb cavity

A.3.3.1. Surface electrochemistry and Joule heating

During the simulation of C100 cavity (without and with coolant), the Nb surface was grounded (0 V vs. RE) while the Al electrode was applied a fixed potential of – 14 V vs. RE. The simulated electrochemical polishing results of C100 cavity without coolant flow are summarized in **Figs. A5-7**. The inside of the cavity is filled with static (i.e. non-flowing) electrolyte and the outside of the cavity is static air. The outside boundaries of the air domain are set as open boundaries, which allows the outgoing heat flux if the temperature exceeds ambient temperature. It's worth noting that the coupling between electrochemistry and temperature is a positive feedback loop, which means that the electrochemical polishing current and the temperature in the vicinity areas will constantly go higher, at least in the range when the measured electrochemical kinetics data is valid. Without proper cooling, the system does not reach an equilibrium state. Thus, results from a few representative transient times are shown here. It should also be pointed out that, even though the results are presented in the order of temperature distribution followed by electrochemical status, these two processes affect each other back and forth in the electrochemical polishing process.

Fig. A5(a)-(c) demonstrates the temperature distribution of the system at 1 min, 5 min and 30 min after the electrochemical polishing starts. The temperature at the inner surface of the cavity at these time steps is plotted in **Fig. A5(d)**. It can be seen that without the coolant flow, the system heats up quickly, from ~ 25.3-26.1 ºC at 1 min, to ~ 32.4 ºC after 30 min. It is also noted that due to the different heat capacity of the electrolyte and air, after 30 min of electrochemical polishing, the temperature is much higher in the air side (~ 32.4 ºC) than that of the electrolyte (~ 24 ºC), especially near the Al surface. Nonetheless, except for the initial 1 min, the temperature distribution along the Nb surfaces were found to be rather uniform.

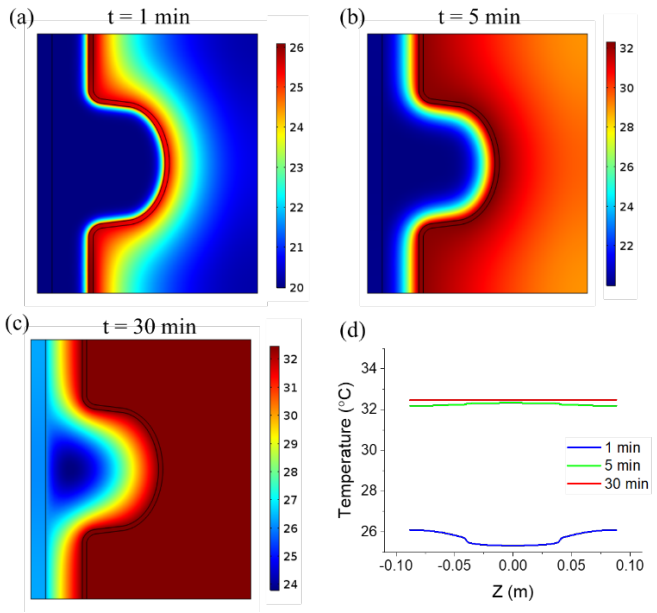

Figure A5 Simulated system temperature distribution without coolant flow at (a) 1 min, (b) 5 min and (c) 30 min, and (d) temperature profile along the inner surface along the z-direction as defined in Fig. 2(b).

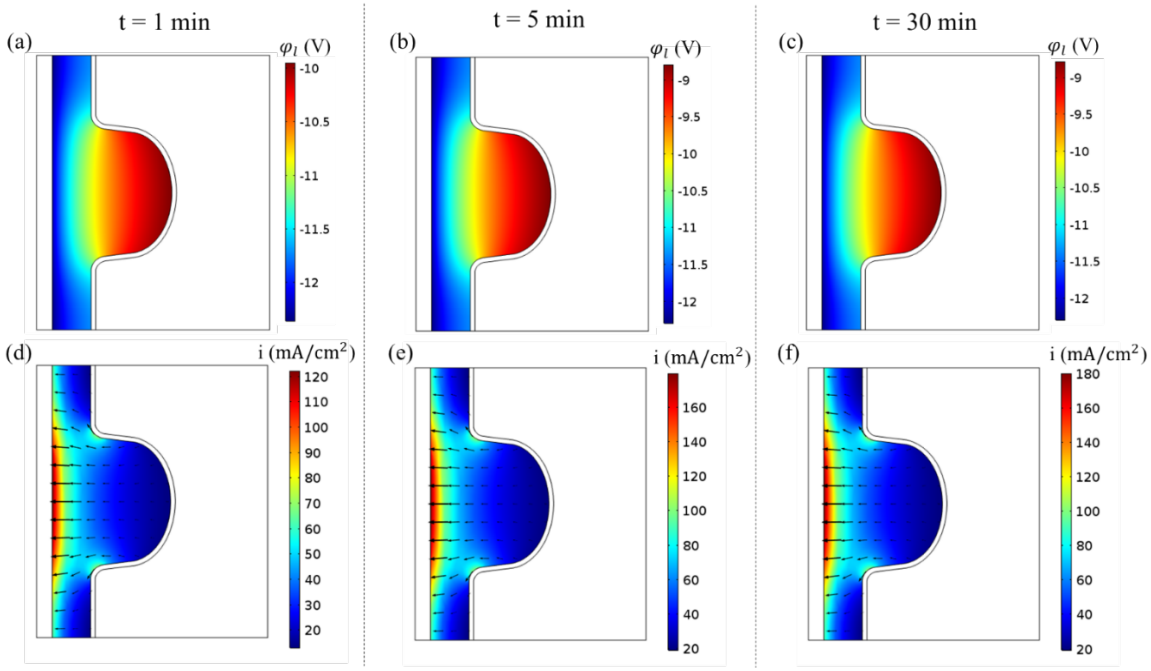

Figure A6 Simulated electrolyte (a-c) potential and (d-f) current density distribution without coolant flow after (a, d) 1 min, (b, e) 5 min, and (c,f) 30 min of EP.

The electrolyte potential and current density distribution within the electrolyte of the C100 cavity are shown in **Fig. A6**, where the different anode-cathode distance along the Nb surface results in rather localized electrochemical activities. Near the equator of the cell, the electrolyte

potential was found to be much higher than that from regions far away, as shown in **Fig. A6 (a)-(c)**, indicating a different driving force for reaction. **Fig. A6 (d)-(f)** shows the current distribution inside the electrolyte, where the current flow vectors (magnitude and direction) are represented by the arrows. It can be seen that along the Nb surface, a local high current density of ~ 50 mA/cm^2 is observed near the iris regions of the cavity at 1 min, which increased to ~ 80 mA/cm^2 at 30 min.

The accumulated oxide thickness and the surface current density through the Nb-electrolyte interface along the z direction are shown in **Fig. A7**. The current density as shown in **Fig. A7 (b)** is the current density normal to the surface, which indicates the electropolishing rate. Note that this is different from the electrolyte current density magnitude from **Fig. A6 (d)-(f)** in the vicinity of the surface, which considers the current caused by potential gradient parallel to the surface. From these results, it could be seen that higher temperature will lead to higher reaction rate for both oxidization reaction and oxide dissolution reaction. The oxide thickness at 5 min is smaller than that at 1 min and keeps on decreasing. This indicates that the dissolution rate increases with temperature faster than the oxidation rate. These simulated results thus show that without sufficient cooling, the high temperature generated from electrochemical polishing of just 5 min will quickly dissolve the majority of the anodized oxide, which is likely to cause subsequent etching of the metal surface, resulting in undesirable rough metal surface. In addition, such high temperature could also lead to the formation of porous oxide layer (instead of dense and compact oxide layer) and large amounts of hydrogen bubbles to further deteriorate the polishing results. These simulated results thus highlight the necessity of thermal management during the electrochemical polishing process to achieve an optimized surface finish.

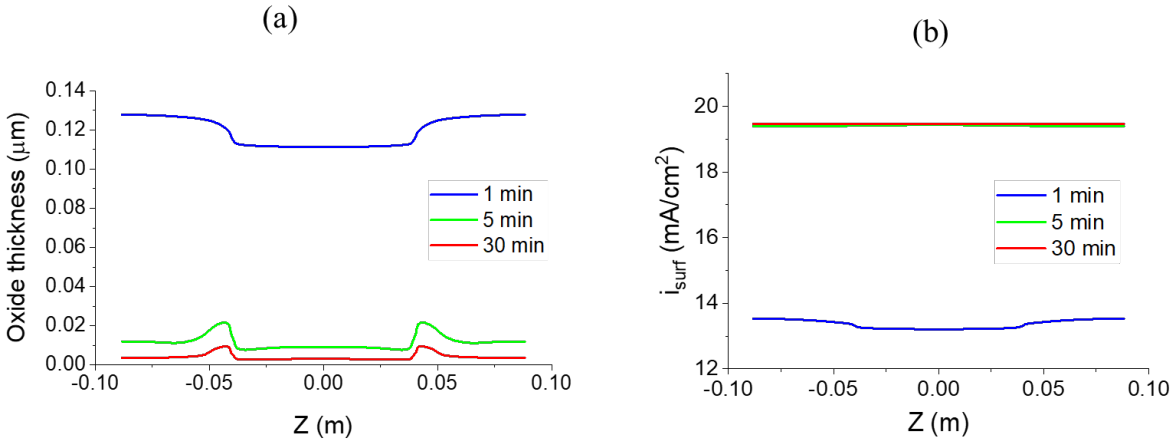

Figure A7 Simulated (a) oxide thickness and (b) current density distribution along the surface of the Nb cavity.

A.3.3.2. Effects of coolant on surface electrochemistry

Fig. A8-A10 demonstrates the results of the C100 model with coolant. We started with no oxide at first. At first few minutes, the current density is high and the oxide grows thicker. During this time, Joule heating is high and will raise the temperature of the system. However, as the oxide grows thicker, the current density drops and Joule heating power begins to decrease. With sufficient coolant flow, the cooling and the heating of the system was found to reach an equilibrium. The oxidization of Nb and dissolution of its oxide also reached an equilibrium and resulted in a steady electrochemical polishing state. Three outside coolant flow rates, 1, 10 and 100 gallon/min (GPM), were chosen to represent a mild, average, and aggressive coolant flow strategy. The inside electrolyte flow was set to be 1 GPM for all the circumstances. **Fig. A8** shows the fluid dynamics of the three different flow rates under the influence of the cavity geometry. It could be seen that the electrolyte flow is faster at the beam tube area while slower at the cavity cell region, thus providing a more significant cooling effect on the beam tube area. The coolant flow (outside of the tube), on the other hand, is rather stagnant at the beam tube region, so it cools down the cavity cell region more effectively. Thus, both inside electrolyte and outside coolant flow are essential for achieving a uniformly low temperature of the system to maintain a steady and uniform electrochemical polishing rate along the Nb cavity surface.

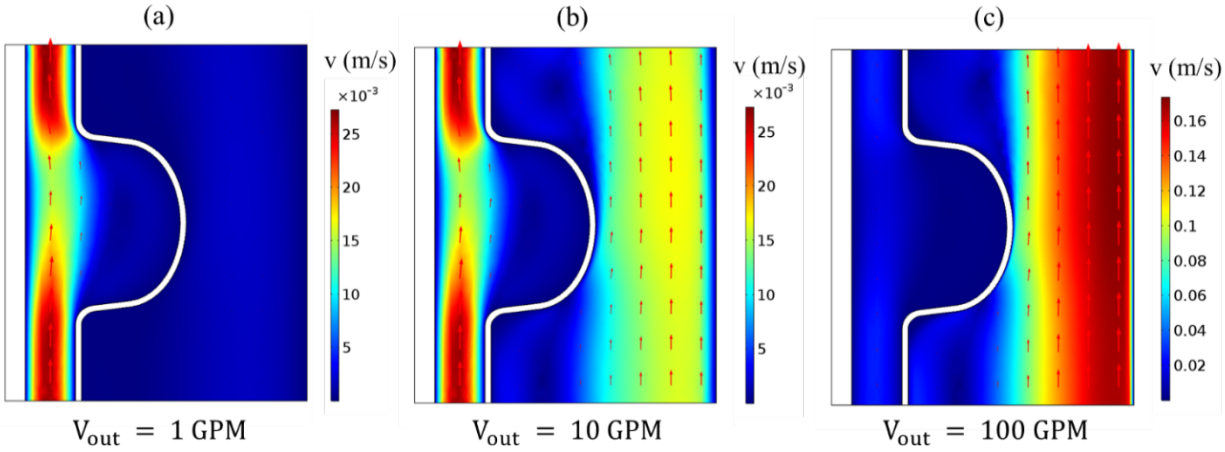

Figure A8 Simulated flow velocity distribution of the electrolyte and coolant water flow with a coolant flow rate of (a) 1, (b) 10, and (c) 100 GPM.

Based on the actual cooling capability of Jefferson Lab [28], two inflow fluid temperatures, 7 and 20 °C, were chosen for both the inside electrolyte flow and outside water flow. As shown in

Fig. A9, with the coolant flow, the system temperature is lowered for all coolant setups studied, with more significant cooling at higher GPM. An asymmetrical temperature distribution could be observed because of the direction of the flow. Because the low velocity of the inside electrolyte flow, a high temperature area could be observed in the cavity cell region. Another high temperature region could be seen at the upper half of the cell region, due to the stagnant flow of the outside coolant. It is also noticed that at 10 and 100 GPM, the upstream cavity wall (i.e. regions closer to the incoming flow) gets more effective cooling than other regions. **Fig. A10(a)** shows the temperature profiles at the inner surface of the cavity. It could be seen that, for both 7°C and 20°C coolant, the flow rate of 1 GPM is not enough to provide efficient cooling at the cavity cell region and the downstream beam tube region. A coolant flow rate of 100 GPM, on the other hand, would cause over-cooling at the cell region, which lead to even higher temperature variance of Nb than that from 10 GPM (**Fig. 6.10 (a)**). In addition, the simulated current distribution in **Fig. 6.10(b)**

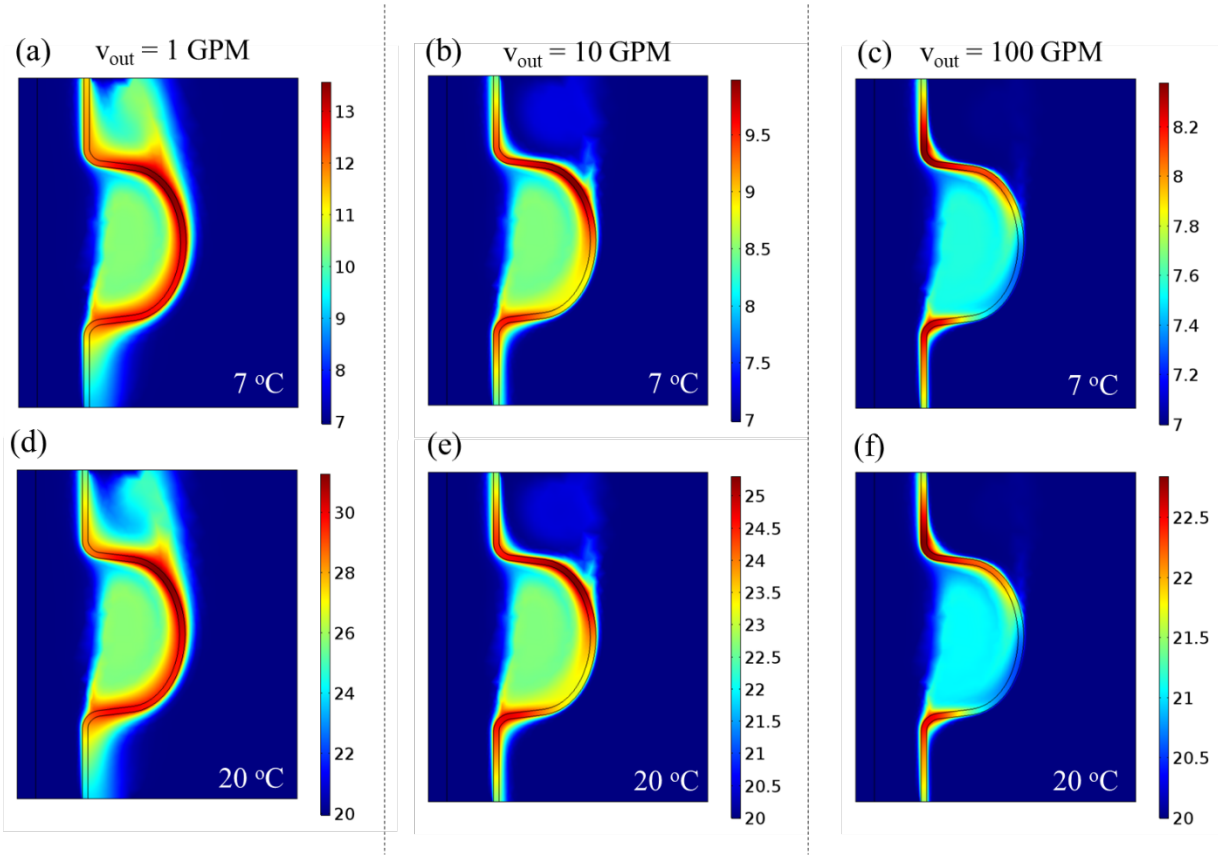

Figure A9 Simulated temperature distribution with different coolant flow of 1- 100 GPM at (a-c) 7 oC and (d-f) 20 oC coolant temperature.

also confirms that 10 GPM flow is the optimal choice for the electrochemical polishing process, that results in the least current variation along the surface. As for the coolant temperature, the 7°C

coolant was found to maintain the system at an even lower temperature, keeping the electrochemical polishing current at a lower value with smaller variance than those at 20 °C. This is expected to allow the formation and dissolution of the oxide layer to proceed at a low rate, leading to smoother surface finish. The simulated results for oxide thickness are plotted in **Fig. A10(c)**. Even though the oxide thickness variation is not the smallest for the optimal coolant setup, which is 7°C and 10 GPM, it is not the key parameter to determine polishing result as long as it is thick enough to prevent etching. Thus, based on these simulation results, it is concluded that among all conditions studied, 7°C coolant inflow temperature with 10 GPM flow rate is the optimal electrochemical polishing condition, providing sufficient cooling with an achievable flow rate to allow the generation of rather uniform surface current and oxide thickness.

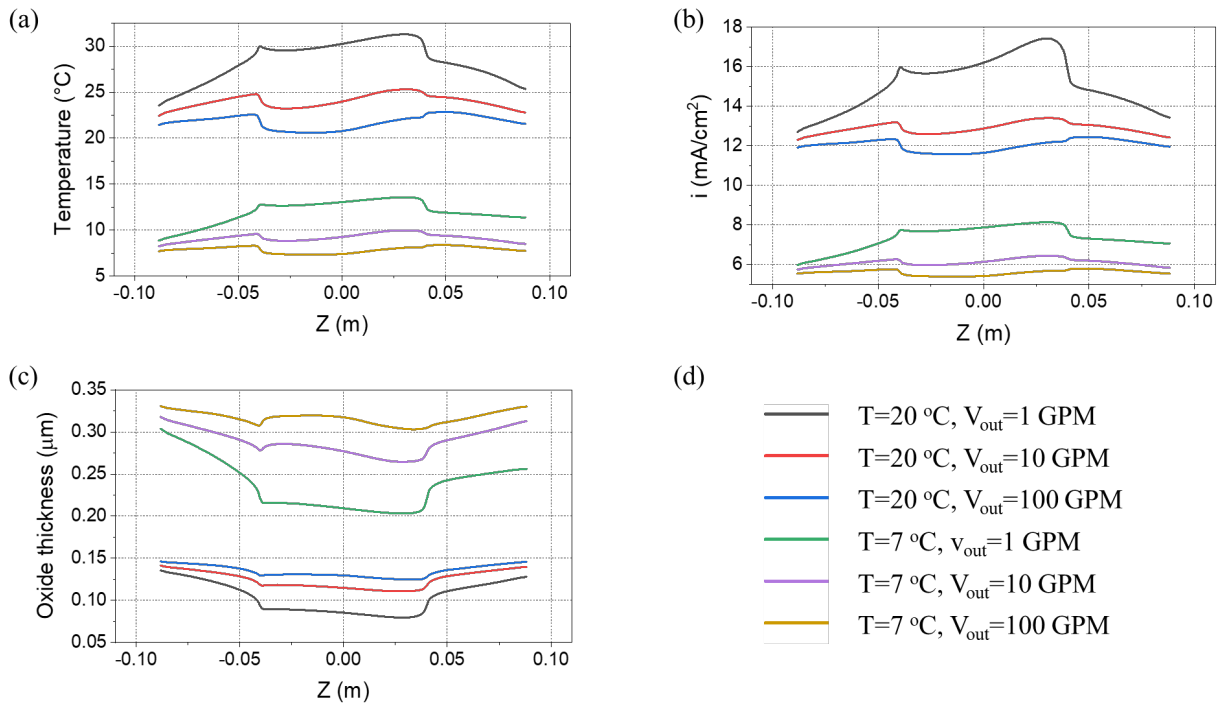

Figure A10 Simulated (a) surface temperature, (b) surface corrosion current density, and (c) oxide thickness under different cooling conditions as listed in the color legend in (d).

A.3.4. Discussion

Despite the success in simulating the current and potential distribution, oxide growth kinetics of Nb electropolishing in a complex cavity geometry under different cooling setups, the model still

has several limitations.

Firstly, the model doesn't consider the effect of electrolyte flow velocity on ion concentration, which will affect the diffusion limited current density. This is limited by the discrepancy in length scale between the diffusion layer, which is a few μm, and the general geometry of the cavity, which is in tens of cm. However, fresh electrolyte flowing in the cavity will only benefit the electropolishing quality and does not affect the significance of the results predicted by our model. Another limitation is that the model hasn't taken convection flow into account due to the instability it will induce into the coupling between the temperature and fluid dynamics. The temperature gradient in this circumstance is small and the convection flow it generates could be neglected compared to the active coolant flow. However, a model with the ion transport under the effect of flow and the fluid dynamics considering the convection flow is under construction to accommodate the model to more scenarios and improve the model's precision.

Another flaw of the model is that there is little experimental validation on the oxide thickness. Previous publication indicates an oxide thickness of 50 ~ 100 nm under similar applied potential but with different electrolyte at room temperature, which is smaller than our simulation results. This could be because the conductivity of Nb_2O_5 used in the simulation was taken from other literatures and might be a bit larger than the conductivity of the dense Nb_2O_5 film that is actually formed in the electropolishing process. A more detailed experimental test and characterization of the oxide film could be conducted to calibrate the oxide growth kinetics.

A.4. Conclusions

In this work, a FE multiphysics model was built and assisted by experimental methods to investigate the electrochemical polishing kinetics of Nb for applications in SRF cavities. Experimentally, it was found that the polarization behavior of Nb in hydrofluoric-sulfuric acid electrolyte shows a Butler-Volmer region at low potentials (~ -1.25 V to -0.5 V vs. Hg/Hg_2SO_4) and a plateau region at high potentials, with the limiting current density in the plateau region increasing monotonically with temperature from 10- 45 ^oC. Using the experimentally validated FE model, the effects of Joule heating, temperature, coolant flow rate on the uniformity of surface current density and oxide thickness along the curved Nb walls of a C100 cavity was studied. It was found that without coolant, the Joule heating quickly accelerate oxidation dissolution, leading to

an ultra-thin oxide layer and unfavorable high surface current density on Nb surface. On the other hand, when coolant was applied, its temperature and flow rate were found to significantly affect the surface current distribution and oxide uniformity. Among all conditions studied, an optimum coolant setup of 7°C and 10 GPM was identified. This developed modeling framework could be used to provide fast and high-fidelity simulations of Nb surface electrochemistry as a function of processing conditions for future cavity design and manufacture, which would be otherwise expensive and time-consuming to perform experimentally.

References

1. Reece, C.E., *Continuous wave superconducting radio frequency electron linac for nuclear physics research.* Physical Review Accelerators and Beams, 2016. **19**(12).
2. Ciovati, G., *Review of high field Q slope, cavity measurements*. 2008, Thomas Jefferson National Accelerator Facility (TJNAF), Newport News, VA ….
3. Lilje, L., *Experimental investigations on superconducting niobium cavities at highest radiofrequency fields*. 2001, University of Hamburg: Hamburg, Germany. p. 127.
4. Ciovati, G., H. Tian, and S.G. Corcoran, *Buffered electrochemical polishing of niobium.* Journal of Applied Electrochemistry, 2011. **41**(6): p. 721-730.
5. Hryniewicz, T., K. Rokosz, and H.R.Z. Sandim, *SEM/EDX and XPS studies of niobium after electropolishing.* Applied Surface Science, 2012. **263**: p. 357-361.
6. Sowa, M., et al., *Influence of electropolishing and anodic oxidation on morphology, chemical composition and corrosion resistance of niobium.* Materials Science & Engineering C-Materials for Biological Applications, 2014. **42**: p. 529-537.
7. Hassel, A.W. and D. Diesing, *Breakdown of ultrathin anodic valve metal oxide films in metal-insulator-metal-contacts compared with metal-insulator-electrolyte contacts.* Thin Solid Films, 2002. **414**(2): p. 296-303.
8. Neelakantan, L., A. Pareek, and A.W. Hassel, *Electro-dissolution of 30Nb-Ti alloys in methanolic sulfuric acid-Optimal conditions for electropolishing.* Electrochimica Acta, 2011. **56**(19): p. 6678-6682.

9. Tian, H., et al., *The mechanism of electropolishing of niobium in hydrofluoric-sulfuric acid electrolyte.* Journal of the Electrochemical Society, 2008. **155**(9): p. D563-D568.
10. Mandula, T.R. and R. Srinivasan, *Electrochemical impedance spectroscopic studies on niobium anodic dissolution in HF.* Journal of Solid State Electrochemistry, 2017. **21**(11): p. 3155-3167.
11. Chandra, A., M. Sumption, and G.S. Frankel, *On the Mechanism of Niobium Electropolishing.* Journal of the Electrochemical Society, 2012. **159**(11): p. C485-C491.
12. Inman, M., E.J. Taylor, and T.D. Hall, *Electropolishing of Passive Materials in HF-Free Low Viscosity Aqueous Electrolytes.* Journal of the Electrochemical Society, 2013. **160**(9): p. E94-E98.
13. Inman, M., E.J. Taylor, and T.D. Hall, *Electropolishing of Passive Materials in HF-Free Low Viscosity Aqueous Electrolytes (vol 160, pg E94, 2013).* Journal of the Electrochemical Society, 2016. **163**(8): p. X5-X5.
14. Guan, L., et al., *pH dependent passivation behavior of niobium in acid fluoride-containing solutions.* Electrochimica Acta, 2018. **285**: p. 172-184.
15. Hryniewicz, T., K. Rokosz, and H.Z. Sandim, *SEM/EDX and XPS studies of niobium after electropolishing.* Applied Surface Science, 2012. **263**: p. 357-361.
16. Tian, H., et al., *Novel characterization of the electropolishing of niobium with sulfuric and hydrofluoric acid mixtures*. 2008, Thomas Jefferson National Accelerator Facility (TJNAF), Newport News, VA ….
17. Tian, H. and C.E. Reece, *Evaluation of the diffusion coefficient of fluorine during the electropolishing of niobium.* Physical Review Special Topics-Accelerators and Beams, 2010. **13**(8).
18. Crawford, A.C., *Extreme diffusion limited electropolishing of niobium radiofrequency cavities.* Nuclear Instruments & Methods in Physics Research Section a-Accelerators Spectrometers Detectors and Associated Equipment, 2017. **849**: p. 5-10.
19. Lee, S.J., Y.H. Chen, and J.C. Hung, *The Investigation of Surface Morphology Forming Mechanisms in Electropolishing Process.* International Journal of Electrochemical Science, 2012. **7**(12): p. 12495-12506.

20. Landolt, D., P.F. Chauvy, and O. Zinger, *Electrochemical micromachining, polishing and surface structuring of metals: fundamental aspects and new developments.* Electrochimica Acta, 2003. **48**(20-22): p. 3185-3201.
21. Reece, C., J. Mammosser, and J. Ortega, *Hydrodynamic thermal modeling of 9-cell ILC cavity electropolishing and implications for improving the EP process*. 2008, Thomas Jefferson National Accelerator Facility (TJNAF), Newport News, VA ….
22. Rodríguez, A.P. and L.M.A. Ferreira, *Copper Electrochemical Polishing Optimisation.*
23. Xiao, B., et al., *HOM DAMPER DESIGN FOR BNL EIC 197MHZ CRAB CAVITY*. 2021, Brookhaven National Lab.(BNL), Upton, NY (United States).
24. Eozenou, F., et al., *Aging of the HF-H2SO4 electrolyte used for the electropolishing of niobium superconducting radio frequency cavities: Origins and cure.* Physical Review Special Topics-Accelerators and Beams, 2010. **13**(8).
25. Rani, R.A., et al., *Thin films and nanostructures of niobium pentoxide: fundamental properties, synthesis methods and applications.* Journal of Materials Chemistry A, 2014. **2**(38): p. 15683-15703.
26. Ravikiran, Y.T., et al., *Synthesis, characterization and low frequency AC conduction of polyaniline/niobium pentoxide composites.* Synthetic Metals, 2006. **156**(16-17): p. 1139-1147.
27. Jin, S., et al., *Buffered electropolishing parameters on niobium sheet.* Physical Review Special Topics-Accelerators and Beams, 2010. **13**(6).
28. Reece, C.E., *Operational Commissioning of the SPEC Horizontal Electropolish System.* JLAB-TN-20-028, 2020.